

57036

217 9122

7a disc 1725

SINTERING OF A MODEL
NICKEL/ALUMINA
CATALYST

SINTERING OF A MODEL NICKEL/ALUMINA CATALYST

PROEFSCHRIFT



TER VERKRIJGING VAN DE GRAAD VAN DOCTOR
AAN DE TECHNISCHE UNIVERSITEIT DELFT, OP
GEZAG VAN DE RECTOR MAGNIFICUS, PROF.DRS.
P.A. SCHENCK, IN HET OPENBAAR TE VERDEDIGEN
TEN OVERSTAAN VAN EEN COMMISSIE AANGEWEEZEN
DOOR HET COLLEGE VAN DEKANEN, OP DINSDAG
23 MEI 1989 TE 16.00 UUR

DOOR

LUCRETIA AGNES CORREIA

SCHEIKUNDIG INGENIEUR
GEBOREN TE PARAMARIBO,
SURINAME

**TR diss
1725**

Dit proefschrift is goedgekeurd door de promotor
Prof.Dr.Ir. L.L. van Reijen

This investigation was supported by the Netherlands Foundation for
Chemical Research (SON) with the financial aid from the Netherlands
Organization for Advancement of Pure Research (Z.W.O.).

VOORWOORD

Op deze plaats wil ik mijn dank betuigen aan allen die een bijdrage hebben geleverd aan de totstandkoming van dit proefschrift. Enkele van hen wil ik gaarne apart vermelden.

- Mevr. W.H. Batenburg - Van der Vegte van de vakgroep Biotechnologie, voor de assistentie verleend bij het Microscopisch onderzoek.
- Dhr. Th.L.J. de Haan van de tussenafdeling der Materiaalkunde, voor de electronendiffractie en EDX-analyse.
- Dhr. C.G. Borsboom van de tussenafdeling der Materiaalkunde, voor de verleende ondersteuning bij het ESCA-onderzoek.
- Dhr. Ir. J. Luijterink van de afdeling der Civiele Techniek, voor de verleende faciliteiten op het gebied van beeldanalyse.
- Dhr. J.H.F. Grondel voor zijn technische adviezen en ondersteuning bij het opzetten van de faciliteiten t.b.v. het dunnelaagonderzoek.
- De medewerkers van de instrumentmakerij van de afdeling, voor, met name, de opdampklok.
- Mijn werkgever, het ECN, ben ik zeer erkentelijk voor de faciliteiten, mij geboden om dit proefschrift te voltooien.
In het bijzonder gaat mijn dank uit naar de dames van de typekamer, o.a. mej. E. Warmerdam en mej. A. Bruin.

CONTENTS

1. INTRODUCTION	1
1.1. General survey	1
1.2. Lay out of thesis	6
1.3. References	7
2. ELECTRON MICROSCOPIC STUDY OF THE SINTERING OF THE METAL PARTICLES IN A Ni/Al ₂ O ₃ MODEL CATALYST	9
2.1. Introduction	9
2.2. Preparation of the model catalyst	9
2.2.1. Preparation of thin alumina supports	9
2.2.2. Deposition of metals	11
2.3. Sintering of the model catalyst in hydrogen	14
2.3.1. Equipment	14
2.3.2. Procedure	16
2.3.3. Analysis by TED and EDX	18
2.4. Results of the analysis by TED and EDX	19
2.4.1. Composition of the model catalyst	19
2.4.2. Discussion	21
2.5. Electron microscope results about particle growth and particle size distribution	22
2.5.1. Sintering at 873 K	22
2.5.2. Sintering at 973 K	27
2.6. Discussion and conclusions	35
2.7. References	37
3. ANALYSIS OF THE CHEMICAL COMPOSITION AND STRUCTURE AT NICKEL- ALUMINA INTERFACES	39
3.1. Introduction	39
3.2. Preparation of specimens	39
3.2.1. Alumina substrates	39
3.2.2. Metal deposits	41
3.2.3. Standard samples	41
3.3. The XPS-method	42
3.3.1. Principles	42
3.3.2. Evaluation of XPS data	45
3.4. Results and discussion	49

3.4.1. Standard samples	49
3.4.2. Thin film composites (TFC)	52
3.4.3. Discussion	58
3.5. Conclusions	61
3.6. References	62
4. KINETICS OF THE GROWTH OF INDIVIDUAL PARTICLES	
4.1. Introduction	63
4.2. Approximations for the rates and the equilibria of elementary reaction steps	63
4.2.1. Transfer between bulk nickel (flat surface) and nickel vapour	65
4.2.2. Transfer between nickel bulk and adsorbed nickel	68
4.2.3. Adsorption and desorption of nickel vapour on and from a flat nickel surface	68
4.2.4. Adsorption and desorption of nickel vapour on and from a flat alumina surface	69
4.2.5. Diffusion to and from a small sphere (embedded in vapour), a small circular disk (in interaction with adsorbed layer) and a flat surface (embedded in vapour)	69
4.2.6. Diffusion of nickel atoms over the surface towards the edge of a half sphere of nickel, supported by a flat alumina surface, and the transition at the edge from the nickel particle to the alumina surface	70
4.2.7. The diffusion coefficients	71
4.3. General formulae for growth rates	72
4.3.1. General remarks	72
4.3.2. Formulae for maximum growth rates	73
4.4. Quantitative evaluation of the maximum rates of the individual growth steps	78
4.4.1. Heats of adsorption, activation energies for diffusion and surface free energies	78
4.4.2. Final results	80
4.5. The role of supersaturation in determining growth rates	85
4.6. Nucleation inhibited growth as a possible rate determining step	86

1. INTRODUCTION

1.1. General survey

In many catalysts for hydrogenation or carbon monoxide conversion processes, the active material is a transition metal dispersed on an oxidic support to prevent contact between the small particles and thus the sintering of the metal phase. It will be clear that the stability of the large active surface area under operating conditions is a requirement of every industrial catalyst. Many chemical causes may be responsible for catalyst deterioration, such as poisoning or carbon formation. One physical effect, however, will always be present, namely sintering of the small metal particles and/or the porous support due to transport of material.

Sintering or coarsening of small supported metal particles is defined as the process by which the mean particle size of the dispersion increases, accompanied by a decrease of the accessible surface area. There are different physical principles involved during this process:

- a. When the particles are small, they can migrate on the substrate during which they can approach each other and coalesce.
- b. When the support sinters, that is the specific surface area decreases, the distance between the particles decreases and in the extreme case particles collide and coalesce.
- c. If the particles are immobile, coarsening can proceed by interparticle transport of atomic (molecular) species either by surface diffusion along the substrate or by transport through the vapour phase.

It is the sintering of small metal particles that will be the subject of this thesis.

The incentive to this work came from parallel work in our laboratory, where the preparation was studied of a nickel alumina catalyst for the conversion of synthesis gas ($\text{CO} + \text{H}_2$) to methane under operation conditions required for its potential application in the exothermal step of an intermediate distance energy transport cycle (N.F.E. project of K.F.A. Jülich) [1]. A special feature of the developed catalyst is the high metal to support volume ratio (1:1) combined with a high thermostability. Apparently at a certain particle size ($\sim 20\text{nm}$

stabilization of particle size, which is observed experimentally. But, combinations of normal growth processes and nucleation inhibition are very flexible and theoretical predictions can be easily adjusted to experimental data.

The present thesis is concerned essentially with the sintering of nickel particles on an alumina support.

Two main lines of investigation have been followed:

- The sintering has been followed experimentally by studying a model catalyst system consisting of a dispersion of small nickel particles on a very thin non-porous alumina foil. Particle sizes and size distributions have been determined by means of electron microscopy. Sintering is performed by heating in a hydrogen atmosphere at 873 K and 973 K.
- An attempt is made to put the theoretical considerations of B.K. Chakraverty and others on a more quantitative basis by making estimates for the frequency factors of the rates of all reaction steps by using Eyring's theory for reaction rates and by relating all possible energy terms in the Arrhenius factors to the experimentally known value of the heat of evaporation of nickel atoms from bulk nickel. In this way it is hoped to come to a better discrimination between the various possible rate determining steps in the growth process and to a more significant comparison of theoretical predictions and experimental observations.

As a side line also in the experimental work some attention is devoted to the possible effects of dopes on the sintering of the nickel particles. Of course the effect of so-called promoters on activity and stability of supported metal catalysts is a well known topic in the field of catalysis. It has been mentioned already, that promoters may stabilize porous supports at high temperatures and thus enhance stability against sintering. A much more difficult question is, whether promoters also will influence the sintering properties of small metal particles due to Ostwald ripening processes, in the way they have been discussed thus far.

A term often used in describing the favourable effect of a support in preventing the sintering of metal particles is metal-support interaction. It is then thought, that at the interface of metal and

diameter) a quite satisfactory stability is achieved, with a catalytic activity still proportional to the metal surface exposed [2].

Relatively few systematic investigations of sintering have been reported for Ni/Al₂O₃ catalysts. C.H. Bartholomew et al. [3] have reported on the sintering behaviour of impregnated catalysts loaded with 15% wt of nickel; E.B.M. Doesburg et al. [2] on the sintering behaviour of coprecipitated catalysts loaded with up to 75% wt of nickel. Despite the difference in preparation conditions all catalysts showed a fast increase of the mean particle size during the first 60 hours of sintering in hydrogen, at for instance 973 K, after which the particle size stabilizes. The specific surface areas of support and metal show a similar behaviour, viz. a fast initial decrease followed by a stabilization. Thus it is concluded, that sintering of the metal is induced by sintering of the support. This idea is reinforced by results of H. Schaper [4], where stabilization of the carrier against sintering by using 1-5 mol % La₂O₃ as dopant led to a better stability of the activity of the catalyst.

Despite the information so gathered, it is very difficult to come to a quantitative understanding of sintering, as it is hard to distinguish between effects caused by the carrier and the metal phase. The only way to do so is by using a thermostable support. Such a system was first reported by E. Ruckenstein [5] by using electron microscopy to study dispersions of very small nickel particles on transparent films of crystalline alumina. Recently various investigations of the sintering of such model catalysts, using electron microscopy, have been published.

P. Wynblatt et al. [6] thoroughly studied the behaviour of a Pt/ γ -Al₂O₃ system in an oxygen environment. Using model catalysts with a mean particle diameter of 6 up to 15 nm, growth of the particles was mainly observed within the very first few hours, after which, as discussed above, the mean particle size stabilizes.

J.J. Chen et al. [7], using a Pd/Al₂O₃ system with a mean particle size of 3.5 nm, also observed a fast increase of the mean particle size within the first hours of sintering in hydrogen.

So, even without the effect of a sintering support, sintering of the

metal phase is substantial and of the same order of magnitude as for metal particles in supported catalysts.

In the last decade also a number of fundamental studies have appeared, emphasizing various theoretical aspects of the sintering of ensembles of small supported metal particles [6, 8 - 10].

Starting with B.K. Chakraverty [9], the notion arose, that the sintering of small metal particles on an inert support can be treated along the same lines as the growing of colloidal particles in a solution. Here the so-called Ostwald ripening process occurs, where the driving force consists of the difference in surface energy of small and large particles and where the mass transport consists of the diffusion of atoms and molecules, dissolving at the surface of the small particles and condensing at the surface of the large particles. The theoretical treatment of these phenomena is due to C. Wagner [10], with improvements due to I.M. Lifshitz and V.V. Slyozov [11]. Altogether this description is well known as the L.S.W.-theory. B.K. Chakraverty has been the first author to apply the L.S.W.-theory to describe the sintering of ensembles of small metal particles. Two rate determining steps for the transport of metal atoms from one particle to another were considered: atom diffusion over the substrate and atom transfer at the interface between particle and substrate. It was shown, that the particle size distribution, if related to the average particle size, tends to a unique asymptotic function for each of the processes, while the rate of increase of the average particle size is proportional to r^{-3} and r^{-1} , respectively, for the two processes considered. T.M. Ahn and J.K. Tien [6] improved B.K. Chakraverty's treatment, by also considering the retardation in the growth process that occurs if the growing particle has well developed crystal faces. Incorporation of atoms in such a face requires the formation of two dimensional nuclei, which can be a very slow process. Finally H.H. Lee [12] has pointed out an unjustified approximation in B.K. Chakraverty's treatment, invalidating the simple power law growth rates obtained earlier.

The confrontation of the predictions of these theories with the experimental results for Pt and Pd dispersions on alumina supports does not lead to conclusive results. There is no single mechanism that explains the combination of fast initial growth and ultimate

support new compounds are formed that bind well to metal and to support leading to an improved cohesion between metal and support. An ancient example is the formation of hydrosilicates in nickel-silica catalysts, discovered by J.J. de Lange and G.H. Visser [13] and extensively discussed by J.W.E. Coenen [14, 15, 16]. During prolonged boiling of a mother suspension or also during slightly hydrothermal conditions at the beginning of reduction, nickel oxide or hydroxide on one hand and silica on the other hand can react to form hydrosilicate layers at the interface between nickel oxide and silica, which persist after reduction, acting as a kind of glue between metal and support. When nickel-alumina catalysts are made by coprecipitation, already in the hydroxide stage a catalyst precursor is formed consisting of a mutual solid solution of nickel- and aluminum-ions in one single hydroxide lattice. Here the unknown factor is to what extent such an intermediate compound persists during the phase separation between nickel and alumina which occurs in the further steps of catalyst preparation. Here too it is possible, that a spinel type NiAl_2O_4 glue still subsists at the interface between nickel and alumina.

Strictly speaking such a glue would not interfere with sintering through an Ostwald ripening process, as not the metal particles have to move, but only the metal atoms evaporating from small particles and condensing on the larger ones. But it is obvious, that traces of compounds, that lead to improved cohesion between metal particles and support, also may strongly influence the mobility of individual atoms, diffusing over the support.

Guided by the experimental technique used for the preparation of the model catalysts for sinter studies and the availability of X-ray Photoelectron Spectroscopy (XPS), several experimental studies have been made in this context:

- The possible formation of intermediate compounds at the interface between nickel and alumina has been studied by XPS. To this end a 300 nm thick layer of non-porous alumina is made by reactive evaporation of aluminum in an oxygen atmosphere onto a quartz substrate. On top of this layer a 100 nm thick layer of nickel is deposited by evaporation in vacuum. Depth profiles of composition and structure at the interface have been obtained with the XPS-facility by intermittantly etching by means of accelerated Ar^+ -ions and measuring XPS-spectra.

- In order to study possible effects of promoters on the formation of compounds at the metal-alumina interface thin layers of chromium and manganese have been introduced between the alumina and the nickel layer by preceding the evaporation of nickel with the evaporation of chromium or manganese. Depth profiles of composition and structure by means of XPS have been made in the same way as described before.
- The effect of chromium and manganese on the sintering of dispersions of nickel particles is studied by introducing thin layers of chromium and manganese between the transparent alumina support of the model catalysts and the nickel film. Again chromium and manganese have been introduced by evaporation onto the support preceding evaporation of nickel.

1.2. Lay out of thesis

The thesis is divided into three parts, viz an experimental section consisting of chapter 2 and 3, a theoretical section consisting of chapters 4 and 5 and an appendix, and general introductions and conclusions in chapter 1 and 6 respectively.

In chapter 2 the electron microscope measurements are presented of average particle sizes and size distributions of nickel model catalysts, supported on transparent alumina films, in the various stages of a sintering treatment.

In chapter 3 analyses by X-ray photoelectron spectroscopy are presented of the composition and structure of the interfaces of thin film composites of nickel and alumina, in some cases separated by thin layers of chromium or manganese.

In chapter 4 rate equations have been presented for the reaction steps, that may lead to the growth of individual nickel particles. After making estimates for the kinetic and energetic parameters involved, quantitative rates have been estimated and decisions have been made as to which steps have to be considered as rate determining.

Chapter 5 is devoted to the final theoretical analysis of the development of particle sizes and size distributions during sintering

of ensembles of nickel particles according to three selected rate determining steps. A discussion is given of the sensitivity of the calculated growth curves to the choice of numerical values of the various parameters involved.

In chapter 6 the experimental results of chapter 2 are compared with the theoretical predictions of chapter 4 and 5. Also, a comparison is made with literature data about the Pt/Al₂O₃ system. Conclusions are drawn as to the effect of additives on the rate of sintering. Also, some general conclusions are presented as to the applicability of the results of this thesis to real catalysts.

The appendix contains an analysis and further justification of a number of assumptions, made in the kinetic and thermodynamic basis of chapter 4 and 5.

1.3. References

- [1] H.W. Nürnberg; G. Wolff: *Naturwiss.* 63 (1976) 190.
- [2] E.B.M. Doesburg; P.H.M. de Korte; H. Schaper; L.L. van Reyen: *Appl. Cat.* 11 (1984) 155.
- [3] C.H. Bartholomew; W.L. Sorensen: *J. Cat.* 81 (1983) 131.
C.H. Bartholomew; R.B. Pannell; R.W. Fowler: *J. Cat.* 79 (1983) 34.
D.G. Mustard; C.H. Bartholomew: *J. Cat.* 67 (1981) 186.
C.H. Bartholomew; R.B. Pannell; J.L. Butler: *J. Cat.* 65 (1980) 335.
- [4] H. Schaper: Thesis (Delft) 1984.
- [5] E. Ruckenstein; M.L. Malhotra: *J. Cat.* 41 (1976) 303.
- [6] P. Wynblatt in *Growth and Properties of Metal Clusters*, ed. J. Beurdon 1980, pg. 15.
T.M. Ahn; P. Wynblatt; J.K. Tien: *Acta Metall.* 29 (1981) 921.
T.M. Ahn; J.K. Tien: *J. Cat.* 66 (1980) 335.

- T.M. Ahn; J.K. Tien: J. Phys. Chem. Solids 37 (1976) 771, 777.
P. Wynblatt; N.A. Gjostein: Acta Metall. 24 (1976), 1165, 1175.
- [7] J.J. Chen; E. Ruckenstein: J. Cat. 69 (1981) 254.
- [8] E. Ruckenstein; D.B. Dadyburjor: Rev. Chem. Eng. 1 (1983) 251.
E. Ruckenstein; B. Pulvermacher: J. Cat. 29 (1973) 224, A. I. Ch.
E. 19 (1973) 356.
- [9] B.K. Chakraverty: J. Phys. Chem. Solids 28 (1967) 2401.
- [10] C. Wagner: Z. Electrochemie 65 (1961) 581.
- [11] I.M. Lifshitz & V.V. Slyosov: J. Phys. Chem. Solids 19 (1961) 35.
- [12] H.H. Lee: J. Cat. 63 (1980) 129.
- [13] J.J. de Lange & G.H. Visser: Ingenieur 58 (1946) 24.
- [14] J.W.E. Coenen: thesis (Delft) 1958.
- [15] G.C.A. Schuit; L.L. van Reyen: Adv. Cat. 10 (1958) 242.
- [16] J.W.E. Coenen; in Preparation of Catalysts II, eds. B. Delmon, P. Grauge, P. Jacobs and G. Poncelet, pg. 83.

2. ELECTRON MICROSCOPIC STUDY OF THE SINTERING OF THE METAL PARTICLES IN Ni/Al₂O₃ MODEL CATALYSTS

2.1. Introduction

The support of the model catalysts consists of very thin non-porous alumina films (< 50 nm), transparent to the electron beam of the electron microscope, obtained by anodic oxidation of an aluminum sheet, removal from the substrate, and subsequent thermal stabilization. The dispersion of nickel particles is obtained by first depositing a very thin layer of nickel (~ 1 nm) on the substrate by evaporation in vacuum from a heating source. During deposition the target is at room temperature. The surface tensions are such, that spreading of the nickel in a thin layer is unfavourable. Thus, after heating in hydrogen, the nickel film breaks apart into a fine dispersion of nickel particles. Interlayers of chromium or manganese, if required, have been obtained by depositing these metals prior to nickel and in the same way as nickel.

In order to study the sintering of the nickel particle dispersion of a particular sample, such a sample was heated for a number of successive periods in hydrogen at 873 K or 973 K. Electron microscope photographs were made from these samples. As the nickel particles are so small that they would oxidize spontaneously in air at room temperature and as they have to be transferred from the sinter apparatus to the electron microscope and vice versa, a careful procedure had to be followed in order to avoid such oxidation.

The structure and chemical composition of the model catalysts before and after sintering have been checked by electron diffraction (T.E.D.) and energy dispersive analysis of X-rays (E.D.X.).

2.2. Preparation of the model catalyst

2.2.1. Preparation of thin alumina supports

Non-porous alumina films can be prepared by different techniques such as oxidation or anodization of aluminum foils [1], reactive evaporation deposition of aluminum [2], sputtering or chemical vapor deposition

[3]. Because very thin films (<50nm) are needed for TEM study, anodization was the most proper way.

Alumina was formed using an aluminum foil, thickness 1.5 mm and purity 99,9995%. The foil was first polished electrochemically, using the recipe of Schwartz [4] as given in table 2.1.

Table 2.1. Electrochemical polishing of aluminum

<u>Polishing solution</u>	<u>Condition</u>
5% chromic acid	10V
52% phosphoric acid	Pb cathodes
5% sulfuric acid	65 C, 2 min

After etching, the foil was rinsed in running water for one hour and washed with distilled water. The clean aluminum was thereafter anodized at 20V in a 3% wt tartaric acid solution, adjusted to a pH 5.5 [1]. After 20 seconds at room temperature the current drops and the process stops. The thus formed amorphous non-porous layer is known to grow with 1.5 nm pro Volt, hence the alumina layer was about 30nm thick. The foil was washed in distilled water and cut to pieces (3*3 mm) suitable for use in the TEM.

The oxide film was detached from the foil by immersing the specimen in a concentrated mercuric chloride solution. When amalgamation started, the specimen was transferred into distilled water where the amalgamation could continue until the oxide film separated from the aluminum. The thin films were again transferred into fresh distilled water and picked up on electron microscope grids, type oyster, as shown in fig. 2.1.



Fig. 2.1. Gold electron microscope grid, type oyster.

Crystallization and stabilization of the amorphous alumina was achieved by heating the specimen in air at 925 or 1025K for 100 hours. These thermally stabilized films were used as support.

2.2.2. Deposition of metals

2.2.2.1. Equipment

The equipment used for vapour deposition, an apparatus built under own supervision (see fig. 2.2a and b) contains:

- A vacuum bell glass with pumping system and vacuum gauges.
- Measuring and control equipment.
- A resistance heated source, from which the metal is evaporated. For deposition of very thin layers a tungsten boat is used, while for thicker layers crucibles with a molybdenum wire-coil heater were used (a). Al_2O_3 and BN crucibles were used to evaporate Ni and Al, respectively.
- A specimen holder with a variable distance to the source of up to 20 cm (b).
- A shutter (c).
- A cold finger (d).

2.2.2.2. Procedure

During physical vapour deposition (p.v.d.) of metals evaporation has to be carried out in high vacuum to ensure as little as possible oxidation to occur. The vacuum system, as shown before, is equipped with an oil diffusion pump able to achieve a vacuum of 10^{-5} Pa in a clean system. However, as the system contains a glass container and rubber seals it is impossible to clean the system by heating. Therefore, a cold finger was constructed on which residual gas can condense and a shutter was installed between the heating source and the substrate to prevent deposition of the metal in the initial stage of evaporation during which the gettering power of the metal vapour is used to clean up the system. Chemical cleaning up is realized by the ability of electronegative metals to bind residual gasses such as water and oxygen. In this way the adsorbed species are immobilized on the inner surfaces of the system ceasing out gassing.

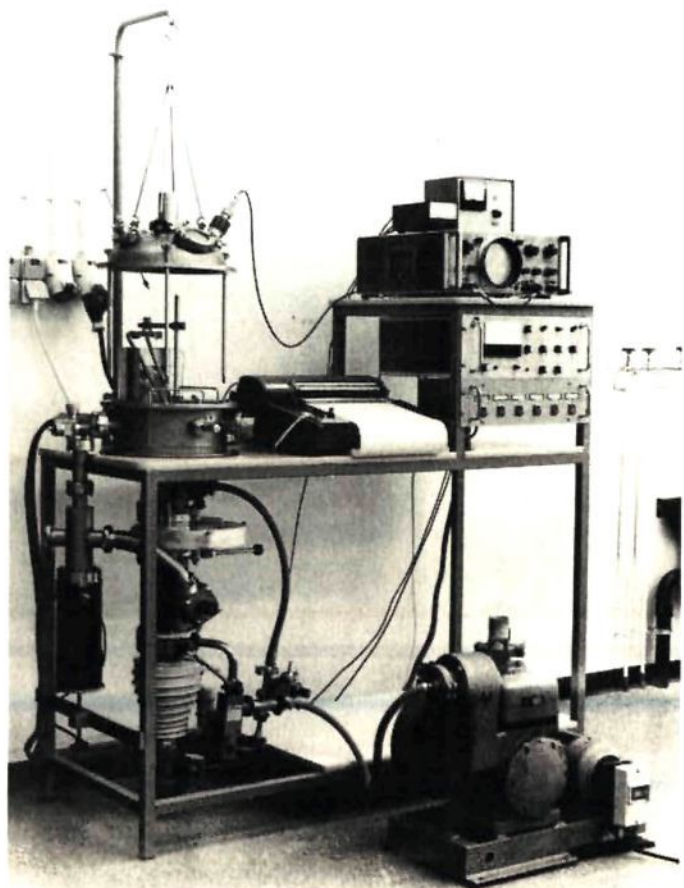


Fig. 2.2a. Vacuum evaporating apparatus

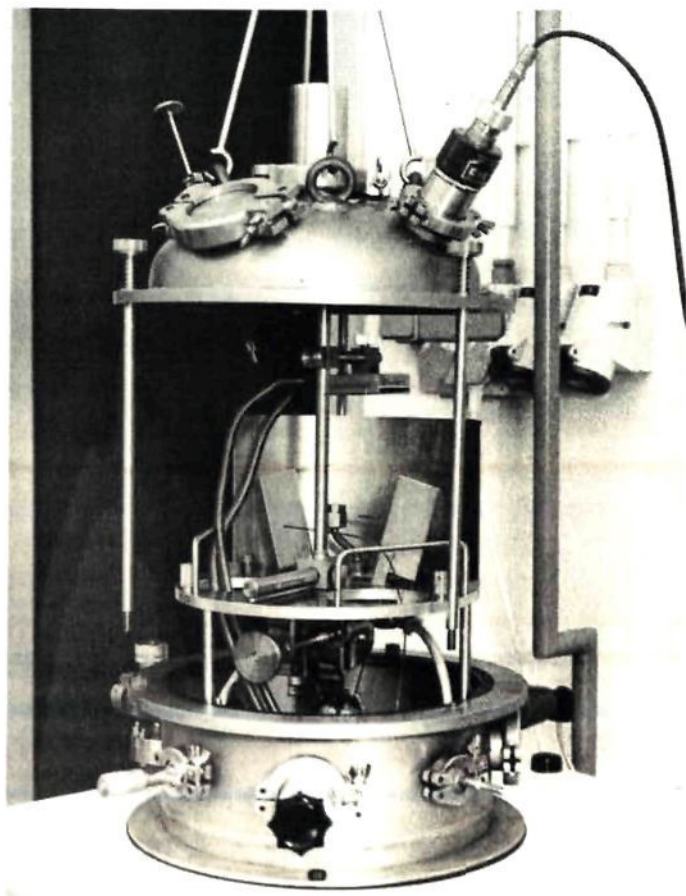


Fig. 2.2b. The inner system of the deposition chamber

So, after achieving high vacuum (1.7×10^{-3} Pa) with the oil diffusion pump, liquid nitrogen is poured into the cold finger during which vacuum immediately improved up to 5×10^{-4} Pa. Then, with the shutter closed, heating up of the metal starts which is accompanied by a fast decrease of the pressure and subsequent increase of the pressure up to the equilibrium vapour pressure of the metal at that particular temperature. After equilibrium is reached the shutter is opened and deposition starts.

The thickness of the deposited thin films is estimated by an indirect technique, namely measuring the light transmission of a film simultaneously deposited on a quartz slide using a spectrophotometer Zeiss PMQ-2. This appears to be a suitable technique for measuring the thickness of very thin films. However, because of the high transparency of these films the accuracy is felt to be of the order of 0.5 nm.

For the preparation of extreme thin films a very low growth rate is desired; hence deposition of the metals was studied in a preliminary study. A deposition rate of approximately 0.5 nm min^{-1} could be achieved at an steady state vapour pressure of 2.6×10^{-4} Pa. The corresponding temperatures of the heating source for the different metals used during this investigation are given in table 2.2.

Table 2.2. Deposition conditions and parameters for thickness measurement.

Metal	T(source) K	R nm/min	n	κ
Ni	1625	0.6	1.70	2.40
Cr	1825	0.5	1.87	2.69
Mn	1475	0.6	1.89	2.59

n = film refractive index and κ the absorption coefficient, from ref. [5].

Model catalysts were prepared under the before mentioned conditions, depositing the metal onto the stabilized alumina support, captured in a grid with the specimen holder at room temperature. However, as there was only one heating source in the vacuum chamber, the composite films had to be prepared in several stages. After a film was deposited the vacuum chamber was opened, the heating source changed, and the next layer was subsequently deposited onto the film grown before. The sequence of metal films deposited was first chromium followed by manganese and subsequently nickel. Dependent on the desired model catalyst one or more steps were skipped. However, one has to bear in mind that in the case of multilayers each thin film is exposed to air before the next film is deposited.

All films, up to 10 nm, were shown to be amorphous. The particle ensemble was obtained by heating up the model catalyst, both the nickel-alumina as well as the multmetal layer-alumina systems, in hydrogen. During contraction of the film nickel recrystallizes and small particles are formed. Preliminary experiments have shown that particles of less than 10 nm could be obtained from nickel films of about 3 nm thickness.

2.3. Sintering of the model catalyst in hydrogen

2.3.1. Equipment

2.3.1.1. The gas purification section

Sintering is carried out in hydrogen and because finely dispersed nickel metal oxidizes readily, the model-catalyst has to be passivated in a wet nitrogen flow before exposure to air. The gases used are purified using several agents as is given in table 2.3.

Table 2.3. Adsorbentia used for purification of the gases.

H ₂ gas	N ₂ gas
Pd/Al ₂ O ₃ catalyst	BTS catalyst (Cu/diatomaceous earth)
Molecular Sieves 4A	Molecular Sieves 4A

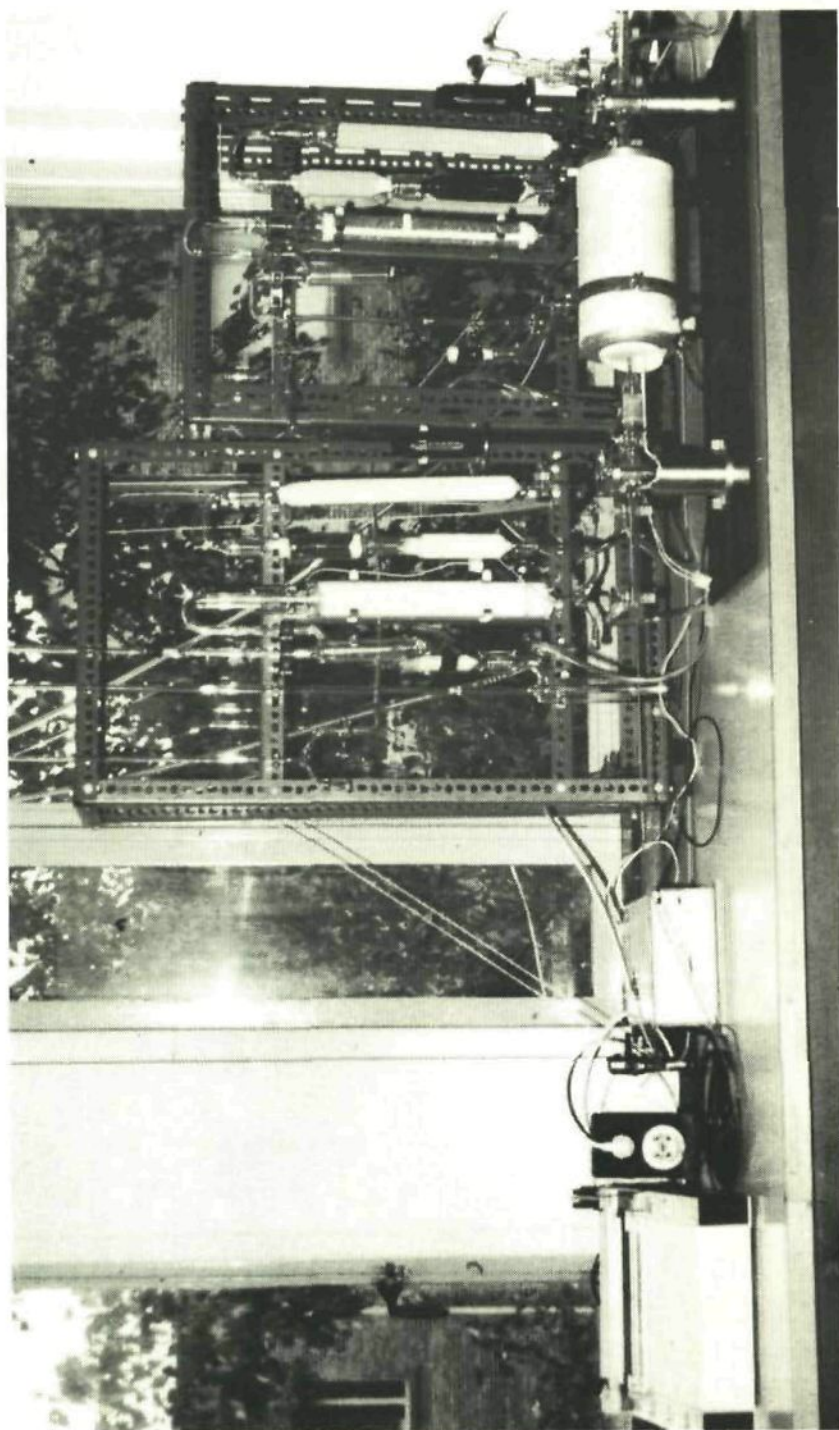


Fig. 2.3. Sinter equipment

2.3.1.2. The sintering device

This device consists of an oven and a quartz tube with a diameter of 12 mm. The tube is divided in three different chambers connected by taps, as can be seen in fig. 2.4.

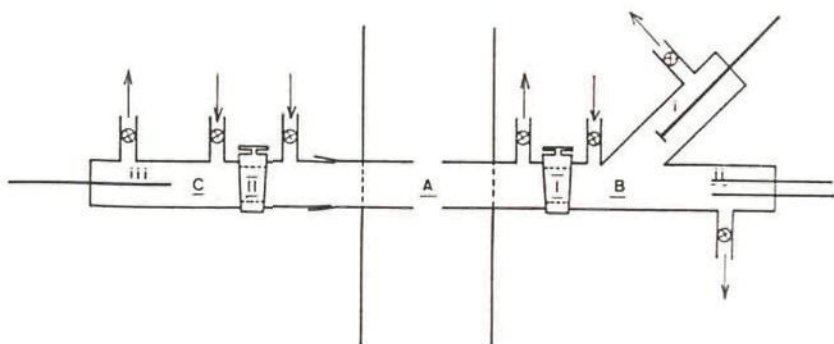


Fig. 2.4. Schematical drawing of the sintering device

- The quartz tube oven (A), diameter 12 mm,
- The quenching and passivation chamber (B).
Here the sample to be analyzed can be selected and quenched. With a hook (i) the boat containing the sample is directed into the side tube, while the remaining boats are pushed back into the oven using a quartz bar (ii) and tap nr. I is closed. After quenching, the sample is passivated by leading a $N_2/3\% H_2O$ gas mixture through the chamber. The sample is then ready for exposure to air and analysis by TEM. After removing the specimen, the chamber is flushed with hydrogen and tap nr. I is opened.
- Sample inlet chamber (C).
After analyzing, the sample is returned into the oven through the inlet chamber. Tap nr. II is closed, disconnecting the chamber from the oven. After flushing with hydrogen, the tap is opened and the specimen can be moved into the oven with the thermocouple (iii).

2.3.2. Procedure

The precursor of the model catalyst, prepared as described before, consists of a thin amorphous nickel film with or without additives and a stabilized γ -alumina layer. Heating this composite results in

crystallization and the formation of a nickel crystallite dispersion. Experimental results on the desintegration of the metal film showed that this is a rather slow process. At 873K contraction of the particles still goes on after one hour ageing. So for convenience the first observation was carried out after three hours heating at the sinter temperature. Sintering is then followed ex-situ in the TEM (Philips EM 201, 401). After each annealing period the sample is photographed and analyzed with a Quantimed 720, Imanco. Analysis of the particle dispersion with the Quantimed is based on image analysis. Therefore, the photograph is projected onto a screen connected to a computer and by means of a sensor the screen is automatically scanned on differences in contrast. By applying a certain threshold in darkness for the background, the coordinates of every point on the screen with a darkness higher than the threshold value are fed into the computer. By scanning the screen a two dimensional array of spots is created with every closed ensemble of points being a particle. Then, using this digital picture, a number of procedures can be executed such as calculation of the particle area and counting of the number of particles, analyzed resulting in a particle size distribution.

Table 2.4. The composition of the model catalysts used for sintering in hydrogen, as determined by light transmission measurement.

Sample Catalyst	Film thickness (nm)			T(sinter) (K)	Number of samples analyzed
	Ni	Cr	Mn		
A	3	-	-	873	1
B	2	-	-		3
C	1	-	-		5
D	5	-	-	973	2
E	1	-	-		4
F	1	1	-		1
G	1	-	<1		1
H	1	1	1		1

As it was impossible to label a certain area of the catalyst, which could serve as a standard particle ensemble to be followed during sintering, different spots were photographed to ensure good overall particle size analysis. For each analysis at least 400 particles have been examined, using up to three pictures. This ensures a deviation in the mean particle size of less than 5%.

Table 2.4 gives a survey of the model catalysts analysed.

2.3.3. Analysis by T.E.D. and E.D.X.

Because of the small dimensions of the model catalysts, foils of approximately 30 nm thickness and 3 mm diameter, the usual techniques such as X.R.D. (X-ray Diffraction) and X.P.S. (X-ray Photoelectron Spectroscopy) can not be used. An excellent tool was found in T.E.D. (Transmission Electron Diffraction) and E.D.X. (Energy Dispersive analysis of X-rays), both available in the electron microscope Philips EM 401.

T.E.D. offers the opportunity for structural analysis of small samples because of the high scattering power of atoms/ions for electrons and the short electron wavelength compared with X-rays. The technique is based on the same phenomenon as X.R.D., namely interference of scattered radiation according to the Bragg's condition: $n\lambda = 2d \sin \theta$. For a typical small angle reflection with $\sin \theta/\lambda = 0.2 \text{ \AA}^{-1}$, numerical evaluation [6] shows that the intensity of scattered electrons is 10^8 times larger than the intensity of scattered X-rays. Hence samples of e.g. 5 nm thickness diffract an electron beam sufficiently strong to give a diffraction pattern, whereas the same sample usually does not contain enough scattering power for X-rays.

Moreover, the line (angular) broadening, $\beta(2\theta)$, of the diffraction lines of powder patterns is related to the crystallite size and the wavelength as:

$$\beta(2\theta) = \frac{\lambda}{D \cdot \cos \theta}$$

As the wavelength (λ) of 100 keV electrons is 0.037 Å while the wavelengths of monochromatic X-rays are of the order of 1 Å (e.g. 1.54 Å for CuK_α), the detection limit, as restricted by particle size is about 40 times better.

The electron beam can also be used for elemental analysis with E.D.X. During exposure of the sample to the beam, an inner shell vacancy is formed (ionization). Subsequently, this vacancy is filled by an electron from a higher energy level, thereby emitting a photon (X-ray) with a characteristic energy for the elements which are analyzed. In contrast with X.P.S. (see chapter 3), however, because of the weak environmental dependency of this process, only elemental analysis can be performed.

2.4. Results of the analysis by T.E.D. and E.D.X.

2.4.1. Composition of the model catalysts

For the catalysts sintered at 873K, the alumina support used was thermally stabilized at 923K in air. Even after prolonged heating (200h) the support was still amorphous, contrary to the results of E. Ruckenstein [7].

After sintering the model catalysts ($\text{Ni}/\text{amorphous-Al}_2\text{O}_3$) for 150 hours in hydrogen, some crystallization of the support appeared to have occurred. No change in the nickel pattern was observed.

The supports for the catalysts sintered at 973K were stabilized at 1025K in air before metal deposition. At the first measurement, the high nickel loaded catalyst D showed to have an amorphous support, while the supports of the low nickel loaded catalysts E-H were crystalline.

Also in this case further heating in hydrogen of model catalyst D leads to some crystallization of the amorphous support. The electron diffraction pattern shows a few additional spots, fig. 2.7, and the TEM pictures some crystal boundaries within the amorphous phase. This can be seen from fig. 2.5, where the dark areas bordered with straight lines are the $\gamma\text{-Al}_2\text{O}_3$ crystallites. Also in this catalyst no change in the nickel pattern was observed.

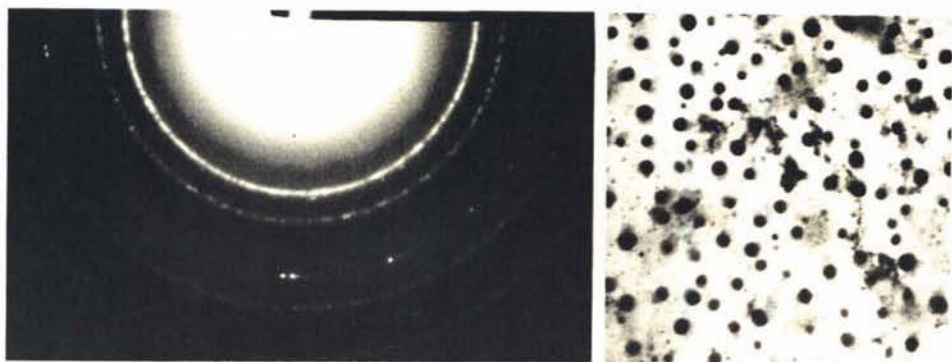


Fig. 2.5. Electron Diffraction pattern and the electron micrograph of model system D.

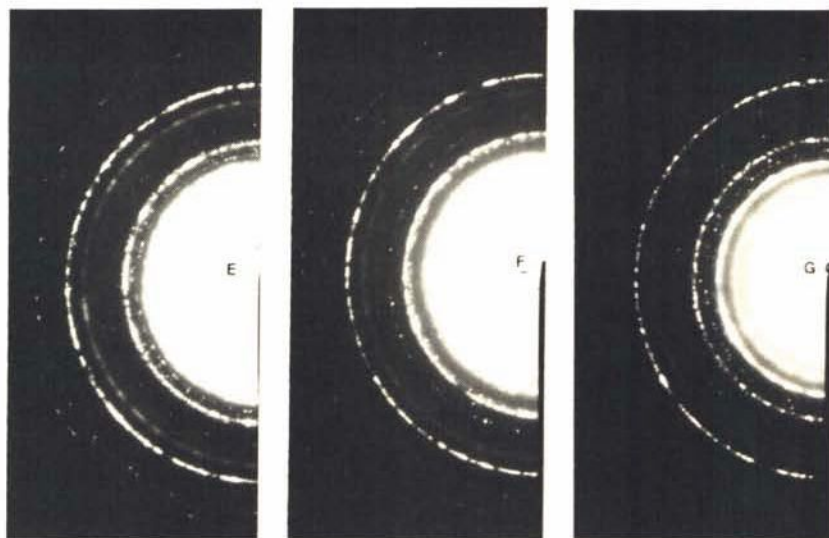


Fig. 2.6. Electron Diffraction pattern of model systems E, F and H

The sintered catalysts E-H, starting with a crystallized support, do show different features. At the first measurement in all systems, except for catalyst F, nickel aluminate is detected. In the Ni-Cr-Al₂O₃ system of catalyst F no nickel aluminate is found, while nickel chromate cannot be detected as a separate compound because its electron diffraction pattern coincides with those of nickel and alumina. Addition of manganese to the model catalyst results in the formation of both nickel and manganese aluminate as can be seen in table 2.5.

At the time sinter experiments at 973K started, it became possible to perform quantitative E.D.X. analyses. Therefore only catalysts E-H have been be characterized in this way. The result of the structural (TED) and elemental (EDX) analyses are gathered in table 2.5.

Table 2.5. Chemical and physical composition of the model catalysts.

Catalyst	EDX results after 3h. sintering			TED results after 300h. sintering		
	Mol.% with respect to Al ₂ O ₃			Ni	Al ₂ O ₃	Intermediate
	Ni	Cr	Mn			
D	25			c	a	
E	4.6	0.2	0.1	c	γ	NiAl ₂ O ₄
F	3.6	3.6		c	γ	
G	4.9	0.2	2.9	c	γ	MnAl ₂ O ₄ , NiAl ₂ O ₄
H	4.2	5.1	3.4	c	γ	MnAl ₂ O ₄ , NiAl ₂ O ₄

c = crystalline; a = amorphous

2.4.2. Discussion

The alumina supports prepared by cleaning the aluminum foil in a fresh polishing solution were shown to be amorphous after heat treatment, while those cleaned in a repeatedly used bath could be crystallized. In contrast with the recipe of E. Ruckenstein the aluminum foil used for the preparation of the alumina supports was polished in a chromic acid containing bath. H. Konno [8] showed that chromate ions strongly adsorb on alumina films and as it is expected that the polished aluminum will be covered immediately with a thin oxide film, adsorption of chromate ions can be expected to occur. Subsequently during anodization the ions probably penetrate into the oxide film after having been reduced to Cr(III). The so formed chromium oxide then stabilizes the alumina layer.

After using the bath for several times the colour of the bath changes

from red to green, indicating the reduction of chromate ions, Cr(VI), to chromium cations, Cr(III). Depletion of chromate ions in the solution must have lead to decreasing crystallization inhibition of the supports of catalysts E-H.

So, although only a trace of chromiumoxide could be detected in all the supports, we ascribe a certain crystallization inhibition to the presence of chromium ions in alumina.

2.5. Electron microscope results about particle growth and particle size distribution

2.5.1. Sintering at 873K

At this temperature samples with different nickel metal loading were used (see table 2.4). The mean particle sizes of the nickel dispersions of catalysts A, B and C are given in table 2.6. For this experiment one sample of catalyst A, three samples of catalyst B and five samples of catalyst C were sintered with specimens of the same composition placed separately in different alumina boats in the oven.

Table 2.6. The mean particle size of the catalysts before and after sintering, with r in nm.

Catalyst	$\bar{r}(0)$	$\bar{r}(\text{end})$	number of samples
A	6.5	8.4	1
B	3.5	5.4	3
C	2.0	3.3	5

In fig. 2.7, the change of the mean particle size, for all samples, during sintering is shown. It can be seen that, although there is some scattering in the measured particle sizes of different samples of the same catalyst, this amounts to 8% only, hence sintering of the metal dispersion is reproducible.

From the same figure it can be seen that, despite the difference in the initial mean particle sizes of the three catalysts, they all show an initially fast increase in the particle size of less than 75%. After 10 hours sintering the growth rate decreases after which at approximately 50 hours, the mean particle sizes tend to stabilize at a level of 8.4, 5.4 and 3.3 nm as specified in table 2.6. However, some samples of model catalyst C, denoted as C[0, x, +] in fig. 2.7, exhibit an

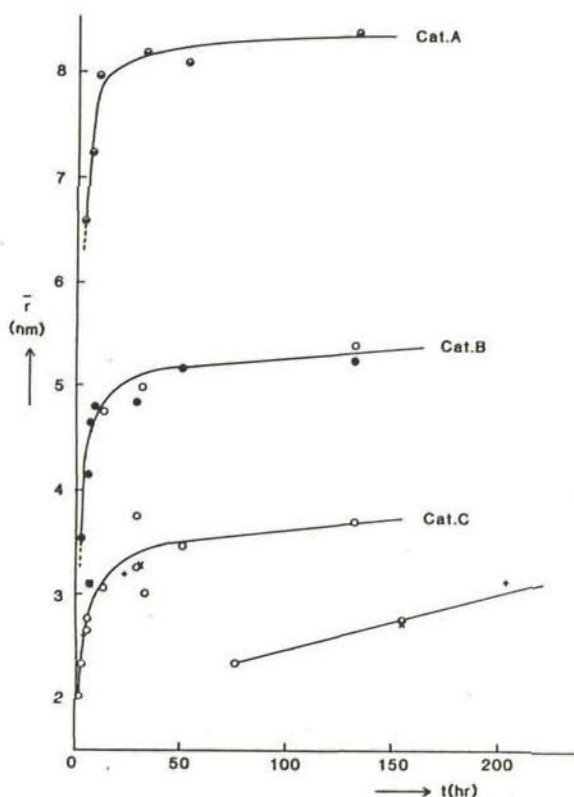


Fig. 2.7. The change of the mean particle sizes of three different model systems during heat treatment at 873K in hydrogen.

anomalous behaviour after 72 hours sintering. In contrast with the other samples showing a stabilization level at 3.3 nm, the mean particle size of these samples drops after which growth proceeds again, steadily but slowly.

The development of the particle size distributions for the catalysts A, B and C are given in fig. 2.9, 11 and 13. Fig. 2.9 represents the P.S.D. for model catalyst C after heat treatment for 6, 28 and 133 hours, with the micrographs given in fig. 2.8. This system, having the smallest mean particle diameter (4 nm), shows the most narrow distribution. After 133 hours the P.S.D. is only slightly broadend.

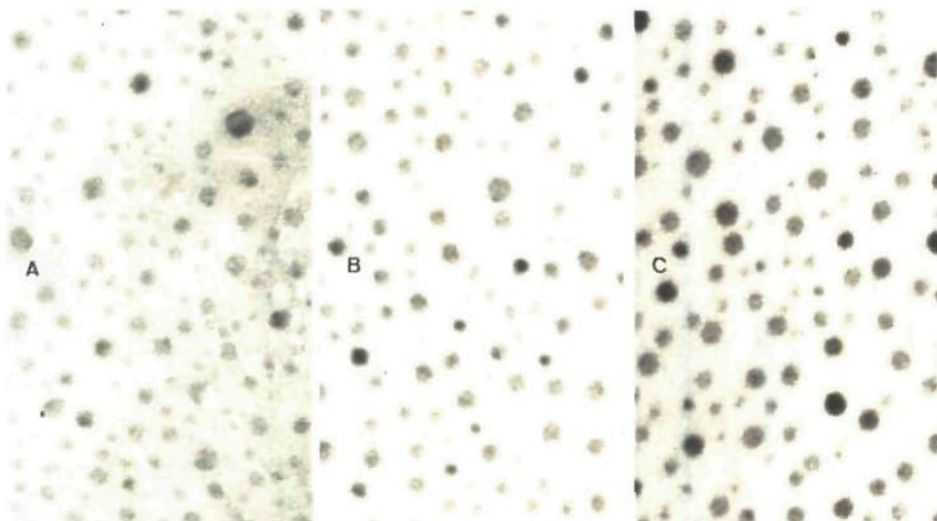


Fig. 2.8. Electron micrographs of model catalyst C after 3h (a), 28h (b) and 133h (c) sintering at 873K in hydrogen. Scale 1 cm = 30 nm.

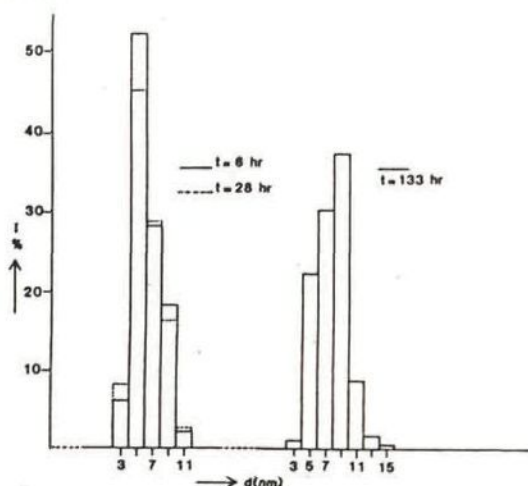


Fig. 2.9. Particle size distribution evaluated for catalyst C at different stages during sintering at 873K in hydrogen.

For the somewhat coarser modelcatalyst B, the electron micrographs are given in fig. 2.10 and the PSD's in fig. 2.11. The PSD of modelcatalyst B, fig. 2.11, for the 'fresh' catalyst resembles that of catalyst C. In this case a significant broadening of the distribution is observed.

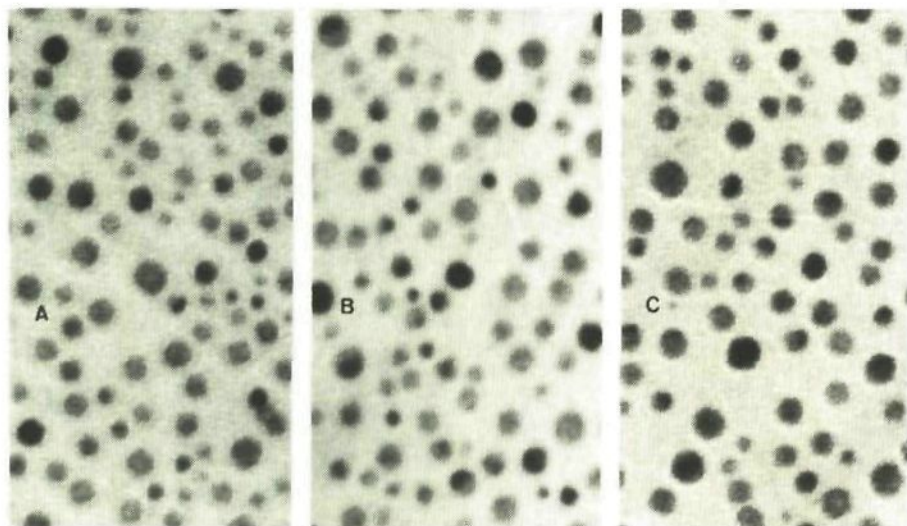


Fig. 2.10. Electron micrographs of model catalyst B after 5 hr(a), 30 hr(b) and 153 h (c) sintering at 873 K in hydrogen. Scale 1 cm = 30 nm.

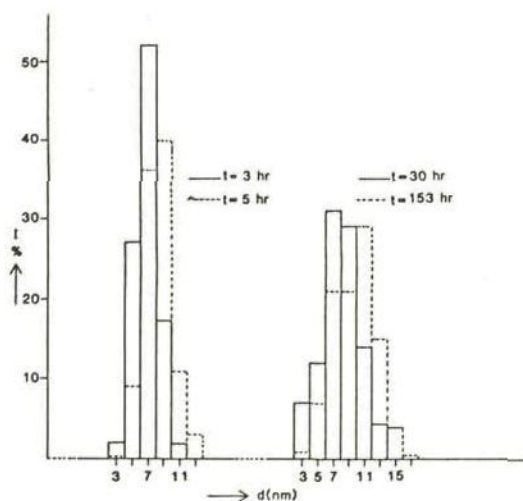


Fig. 2.11. Particle size distribution evaluated for catalyst B at different stages during sintering at 873K in hydrogen.

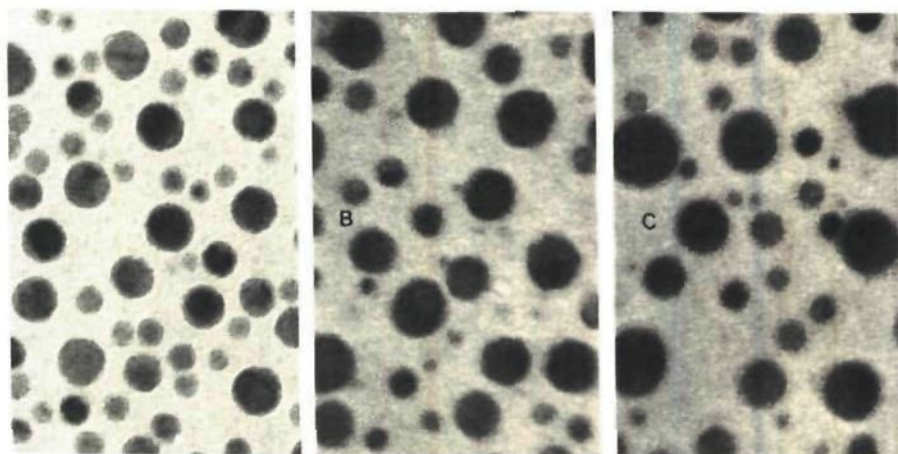


Fig. 2.12. Electron micrographs of model catalyst A after 5 hr (a), 30 hr (b) and 132 h (c) sintering at 873 K in hydrogen. Scale 1 cm = 30 nm.

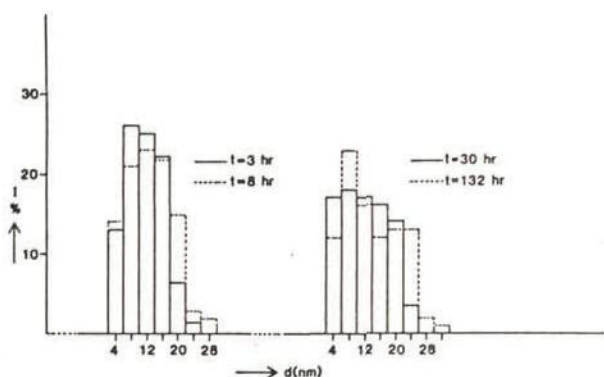


Fig. 2.13. Particle size distribution evaluated for catalyst A at different stages during sintering at 873 K in hydrogen.

From fig. 2.12 and 2.13 it can be seen that the PSD of the catalyst A is extremely broad, while during sintering the features of the PSD only change slightly.

Now, as shown before in fig. 2.7 samples C 0, x and + behave differently. Therefore the development of the PSD of catalyst C 0 during sintering is also given in fig. 2.14. This nickel particle ensemble contains a higher amount of particles smaller than 5 nm than the one characterized by fig. 2.9.

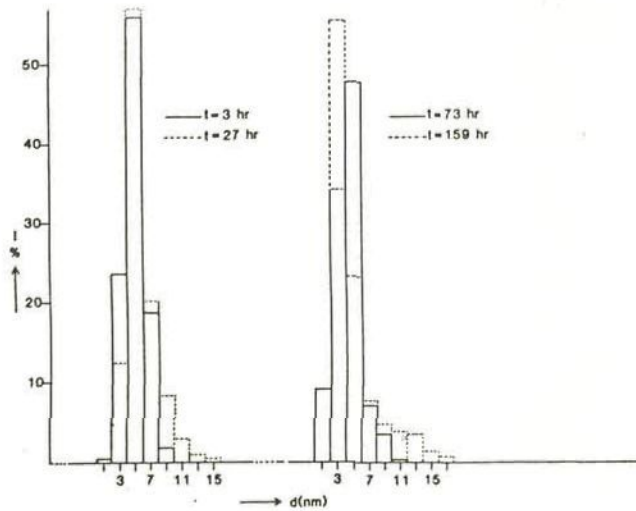


Fig. 2.14. Particle size distribution evaluated for catalyst C,0 at different stages during heat treatment at 873 K in hydrogen

Furthermore, this sample shows a remarkable increase of the relative number of particles of 3 nm, accompanied with a significant broadening of the distribution, and an increased tendency for facet formation.

2.5.2. Sintering at 973 K

Four model catalysts of different chemical composition, as given in table 2.7, were used for the experiments at this temperature.

Table 2.7. Characteristics of the model catalysts used at 973 K, with \bar{r} in nm.

Catalyst	Chemical composition	$\bar{r}(0)$	$\bar{r}(\text{end})$	number of samples
D	Ni - Al ₂ O ₃	11.5	12	2
E	Ni - Al ₂ O ₃	2.6	4.1	3
F	Ni-Cr - Al ₂ O ₃	2.0	3.1	1
G	Ni-Mn - Al ₂ O ₃	4.3	6.4	1
H	Ni-Mn-Cr- Al ₂ O ₃	2.6	5.0	2

For all the samples the changes of the mean particle size and the PSD during sintering have been plotted in fig. 2.15 and 2.22. The electron micrographs exhibit changing of the morphology of growing particles while for the large particles facet formation is obvious.

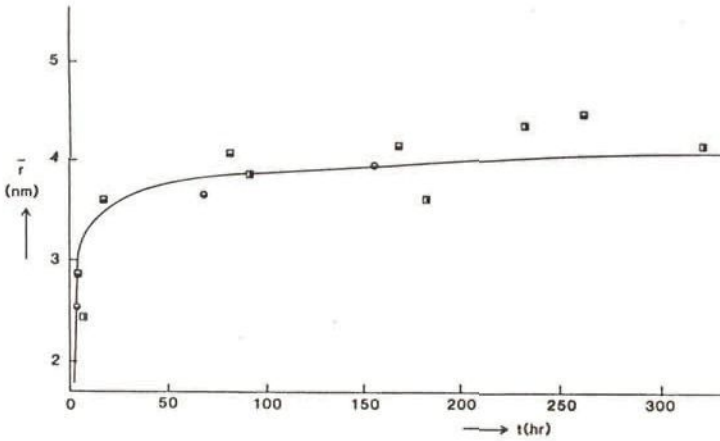


Fig. 2.15a. The change of the mean particle size of the model system, Cat. E: Ni/Al₂O₃, aged at 973 K in hydrogen.

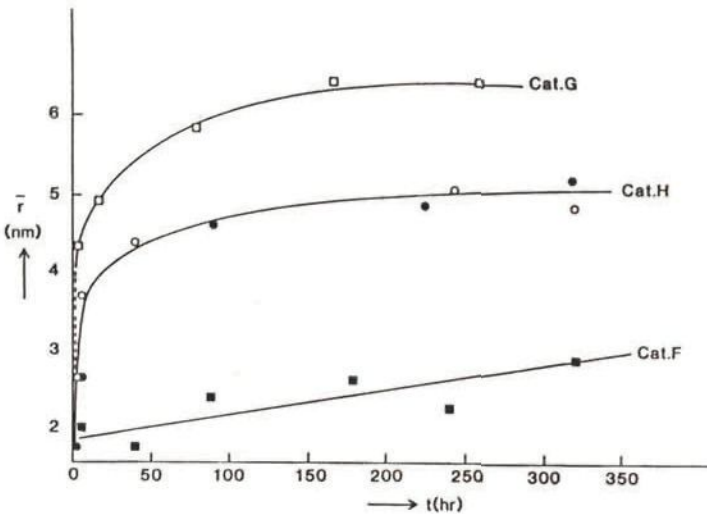


Fig. 2.15b. The change of the mean particle sizes of the model systems, Cat. F: Ni/Cr/Al₂O₃, Cat. H: Ni/Mn/Cr/Al₂O₃, and Cat. G: Ni/Mn/Al₂O₃, aged at 973K in hydrogen.

2.5.2.1. Ni/Al₂O₃, catalyst E, 4.6 mol% Ni

Three samples were sintered in two successive charges. The mean particle radius amounts to 2.6 nm and increases very fast to 3.5 nm after 16 hours, after which there is only a very slow coarsening, as can be seen from the electron micrographs in fig. 2.16. Starting with a narrow particle size distribution (fig. 2.17) resembling catalyst C, the distribution gradually and steadily broadens.

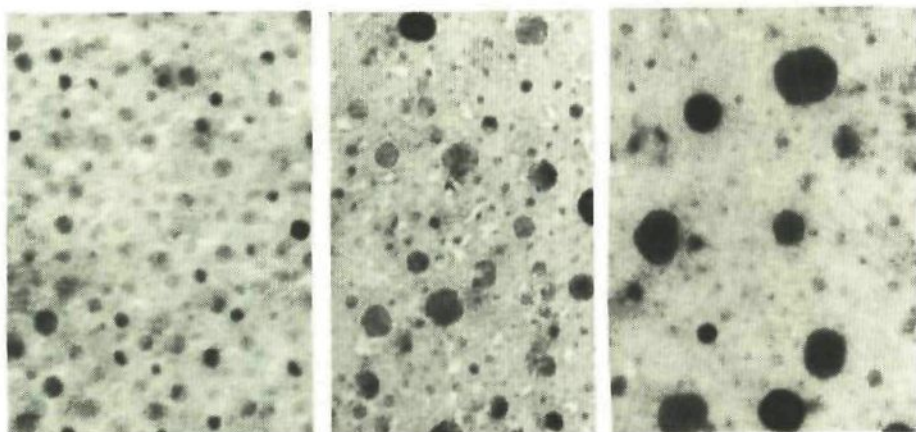


Fig. 2.16. Electron micrographs of model catalyst E after 3 hr (a), 17 hr (b) and 350 hr (c) sintering at 973 K in hydrogen. Scale 1 cm = 30 nm.

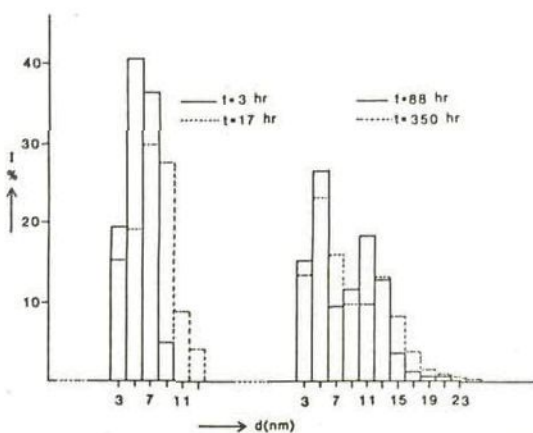


Fig. 2.17. Particle size distribution determined for catalyst E (Ni) at different stages of sintering at 973 K in hydrogen

2.5.2.2. Ni/Cr/ γ -Al₂O₃, catalyst F, 3.6 mol% Ni, 3.6 mol% Cr

This catalyst, containing an equivalent amount of chromium and nickel, exhibits a deviant behaviour during heat treatment (fig. 2.15). With a mean particle radius of 2.0 nm for the nickel dispersion, a linear growth rate is observed in contrast with growth so far observed. From the particle size distribution (fig. 2.19) and the electron micrographs (fig. 2.18), it can be seen that this particular nickel

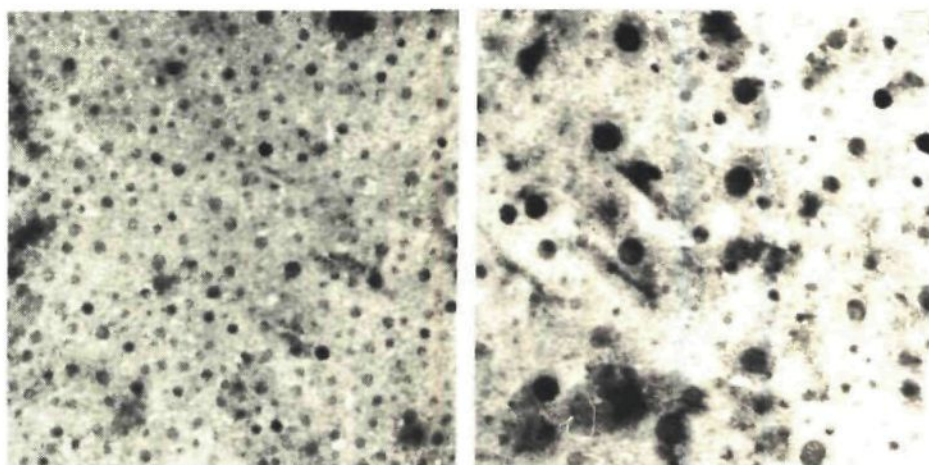


Fig. 2.18. Electron micrographs of model catalyst F after heat treatment in hydrogen at 973 K for 6 hr (a) and 320 hr (b). Scale 1 cm = 30 nm.

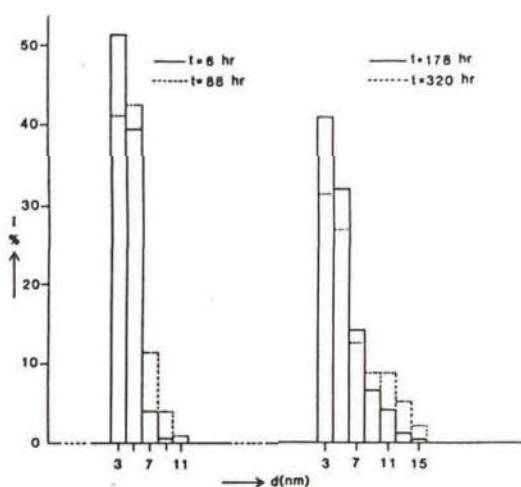


Fig. 2.19. Evolution of the particle size distribution of the catalyst F (Ni/Cr) during ageing in hydrogen at 973 K

dispersion has an extremely narrow distribution. During ageing some broadening up to 15 nm occurs with hardly any change in the features of the distribution.

2.5.2.3. Ni/Mn/ γ - Al_2O_3 , catalyst G, 4.9 mol% Ni, 2.9 mol% Mn

Sintering of this model catalyst results in a gradual increase of the mean particle radius of 4.3 nm up to 6.4 nm, showing a stabilization level at 6.4 nm after 170 hours.

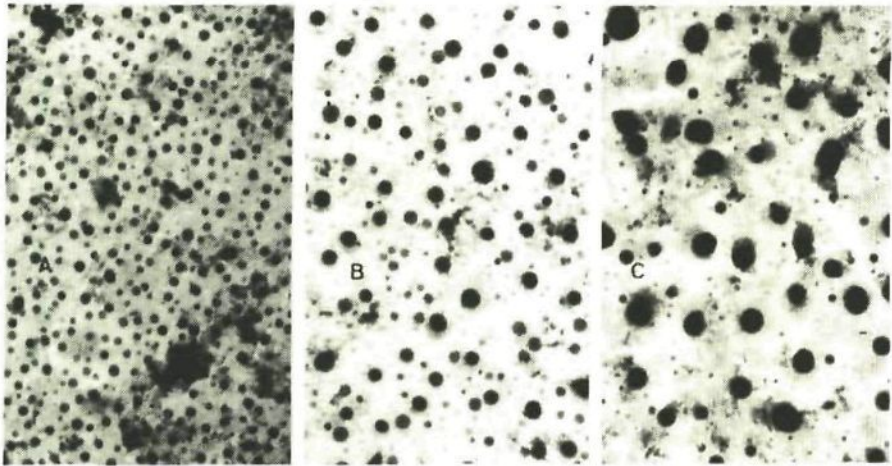


Fig. 2.20. Electron micrographs of model catalyst G after heat treatment in hydrogen at 973 K for 3 hr (a), 80 hr (b) and 259 hr (c). Scale 1 cm = 100 nm.

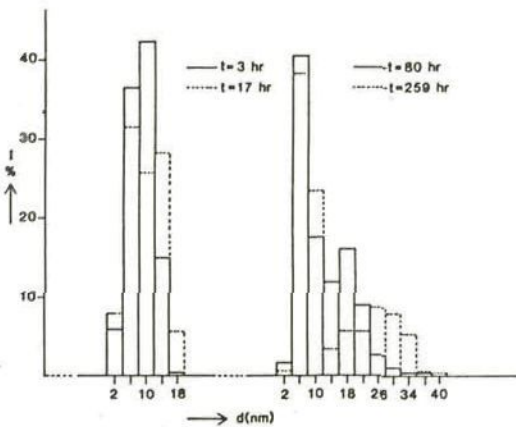


Fig. 2.21. Particle size distribution determined for catalyst G (Ni/Mn) during sintering at 973 K in hydrogen

Compared with the nickel model catalyst E, the particle size distribution (fig. 2.21) is somewhat broader. During sintering extreme large crystallites grow with a particle diameter up to 42 nm. Remarkable is the high fraction of particles with diameter of 6 nm, during the whole period of heat treatment.

2.5.2.4. Ni/Cr/Mn/ γ -Al₂O₃, catalyst H, 4.2 mol% Ni, 5.1 mol% Cr, 3.4 mol% Mn

The growth curve for this nickel dispersion resembles that of model catalyst E, exhibiting a fast sintering up to 4.4 nm after 40 hours then stabilizing at a level of 5.0 nm. The development of the particle size distribution of this nickel dispersion is the same as for catalyst E.

2.5.2.5. Ni/Al₂O₃, 25 mol% Ni

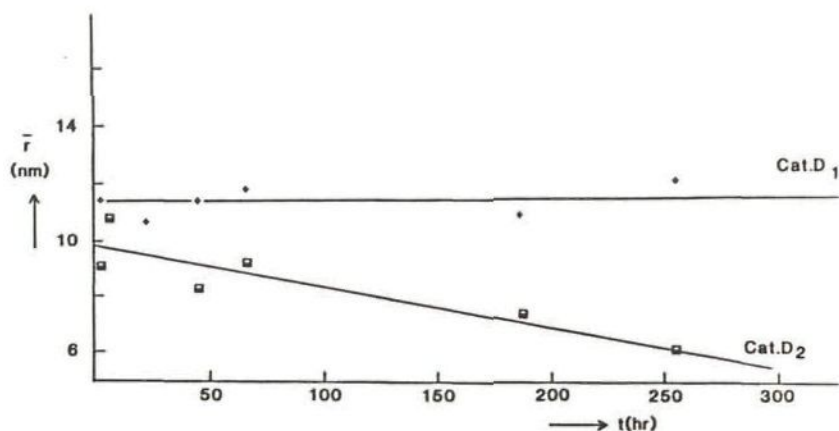


Fig. 2.22. Evolution of the mean particle size in catalyst D during sintering at 973 K in hydrogen

The behaviour of the high nickel loaded model catalyst D is illustrated in fig. 2.22. Also in this case the peculiar behaviour as observed for some samples of catalyst C (fig. 2.14) is found. For catalyst D₁ no change in the mean particle size is observed, while the particle size distribution changes only slightly, as can be seen in fig. 2.24.

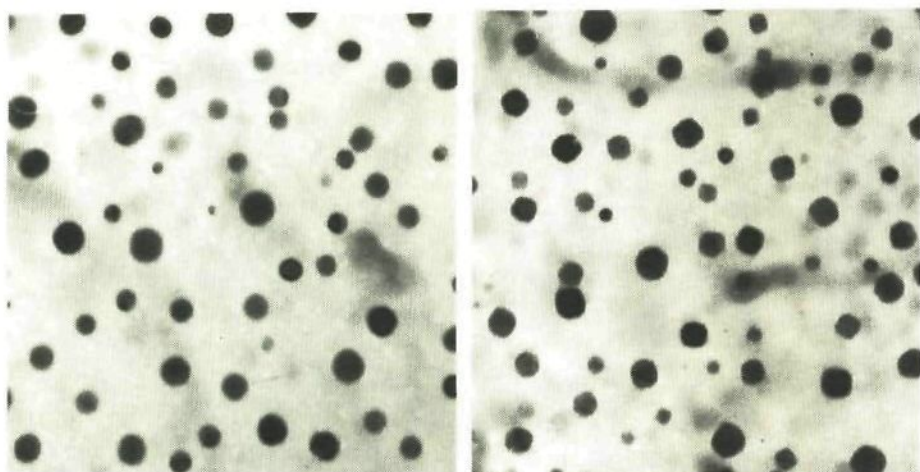


Fig. 2.23. Electron micrographs of catalyst D_1 after sintering for 3 hr (a) and 350 hr (b) at 973 K in hydrogen. Scale 1 cm = 100 nm.

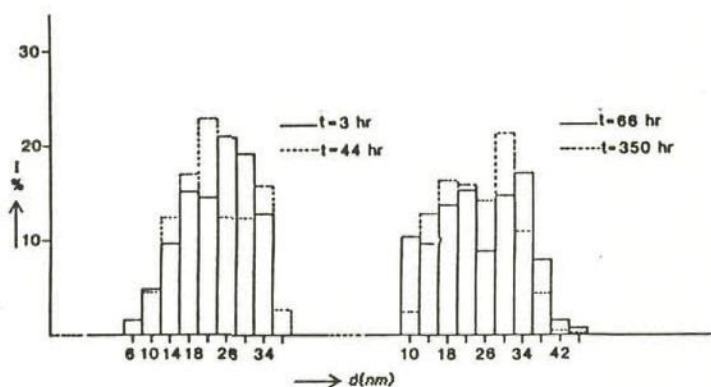


Fig. 2.24. Particle size distribution determined for catalyst D_1 during sintering at 973 K in hydrogen

For catalyst D_2 a decrease in the mean particle size is measured, while the particle size distribution (fig. 2.25) changes dramatically. During heat treatment the fraction of particles with a diameter of 10 nm, increases from 10% up to 81%. This was accompanied with a change in the transparency of the support observed in the microscope. The effect of the structural change of the support is demonstrated in fig. 2.26 and 2.27, with the PSD's evaluated for a crystalline and an amorphous part of the support.

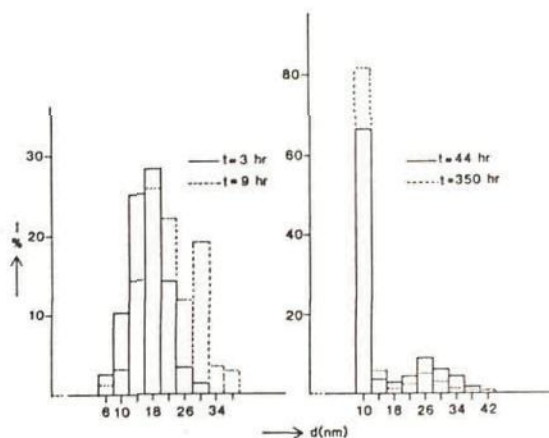


Fig. 2.25. Particle size distribution evaluated for catalyst D₂ during sintering at 973 K in hydrogen.

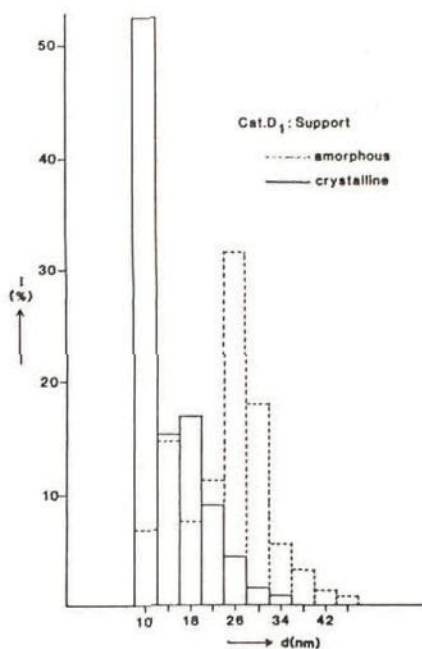


Fig. 2.26. The particle size distribution determined for the nickel dispersion of catalyst D₂ on the amorphous and the crystalline part of the support.

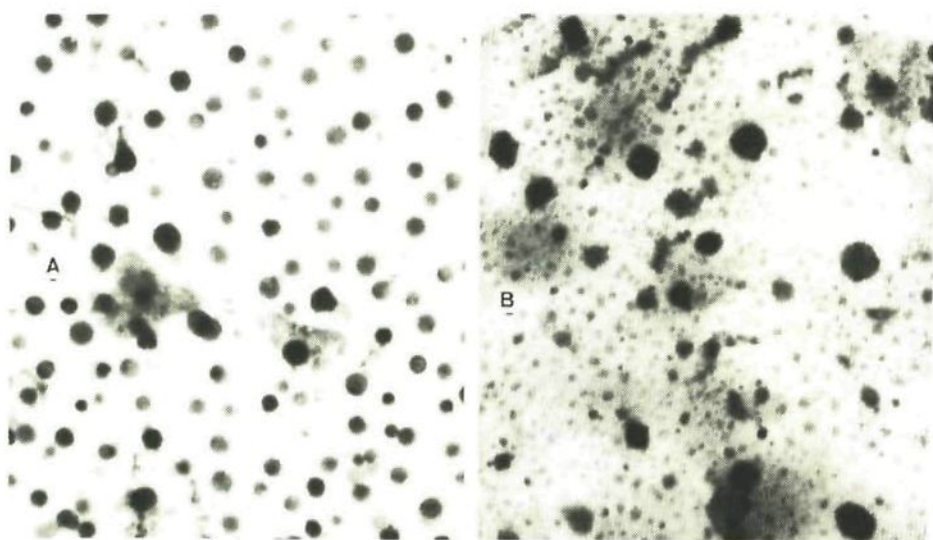


Fig. 2.27. Electron micrographs of model catalyst D_2 after crystallization of the support, a: amorphous and b: crystalline part of the support. Scale 1 cm = 100 nm.

Although the boundary used was rather arbitrary, the difference is remarkable. The particle size distribution on the crystalline part is asymmetric with a high fraction of small particles ($d = 10$ nm). On the amorphous part of the support a broad distribution is evaluated similar to the distribution of the stable catalyst D_1 (fig. 2.24).

2.6. Discussion and conclusions

Particle size distributions as presented in section 2.5.2. show that during sintering the fraction of particles larger than a certain size increases at the expense of the smaller ones. Such a phenomenon corresponds to the expectation for an Ostwald ripening process. Except for the chromium containing catalyst, growth curves of all model systems aged at 873 K as well as at 973 K show an initial stage of fast sintering, followed by a stage of very slow sintering. This is in agreement with the observations on Pt/alumina [9] and Pd/alumina [10] model systems investigated by other authors, but not with the power law growth curves, predicted from theoretical considerations for Ostwald ripening in literature.

At 873 K, increasing initial mean particle sizes lead to growth curves levelling off at increasing particles sizes. In other words: the growth rate apparently does not only depend on average particle size, as is to be expected for Ostwald ripening, but also on other factors.

At 973, no obvious indications for such an effect have been found, and for instance a sample with an initial mean particle radius of 11 nm does not show any growth at all. A possible explanation for the discrepancies at 873 K must be sought in the alumina carrier. After high temperature stabilization of the carrier and before deposition of nickel all carriers studied at 873 K and some studied at 973 K appeared to be amorphous, in contrast for instance to the carrier used by E. Ruckenstein [7]. After deposition of nickel and the subsequent decomposition of the film into separate particles, in several of the catalysts recrystallization of the carrier has been observed. Apparently, notwithstanding the high temperature pretreatment, the carriers have not been as stable as expected. Nickel particle growth connected to recrystallization of the carrier must be held responsible for the anomalous growth at 873 K of nickel dispersions with great initial mean particle dimensions.

In the sinter study at 973 K, using chromium and manganese as additives, chromium decreases the growth rate during the initial stage of sintering while manganese increases growth. Combination of the two metals cancels out both effects.

Comparing the particle size distributions of model catalysts E, F and H (fig. 2.17, 19, 21), addition of chromium (F) shows to increase the dispersion of the nickel phase while on addition of manganese the opposite is achieved. Obviously desintegration of the amorphous nickel film, governed by the nickel-alumina interface, is strongly influenced by the presence of the additives. But also the subsequent sintering of the nickel dispersion is strongly influenced by the additives.

A further discussion of growth kinetics, in particular at 973 K, will be postponed to chapter 6, where experimental results can be compared with theoretical predictions.

2.7. References

- [1] L. Holland; N. Sutherland: *Vacuum* 11 (1952) 155.
- [2] P. v.d. Engel: *Graduation Report* (1983) Delft.
- [3] H. Demiryont: *Thin Solid Films* 101 (1983) 345.
- [4] W. Schwartz: *Plating and Surf Finishing*, June (1982) 42.
- [5] P.B. Johnson; R.W. Christy: *Phys. Rev. B*, 9 (1974) 5056.
- [6] L.I. Maissel; R. Glang: *Handbook of Thin Film Technology*, Mc Graw-Hill, Inc., (1970).
- [7] E. Ruckenstein; M.L. Malhotra; *J. Cat.* 41 (1976) 303.
- [8] H. Konno; S. Kubayashi; H. Takahashi; M. Nagayama: *Corr. Sci.* 22 (1982) 913.
- [9] P. Wynblatt; N.A; Gjostein: *Acta Metall.* 24 (1976) 1165, 1175.
- [10] J.J. Chen; E. Ruckenstein: *J. Cat.* 69 (1981) 254.

3. ANALYSIS OF THE CHEMICAL COMPOSITION AND STRUCTURE AT NICKEL ALUMINA INTERFACES

3.1. Introduction

As compared to the model catalysts, the study of which has been described in chapter 2, the samples to be dealt with in this chapter must be considered as thick non-porous alumina supports covered with thick continuous nickel films (thin film composites, T.F.C.). The substrate is made by evaporation of aluminum from a high temperature source in an oxygen atmosphere and deposition of the oxide molecules formed onto a quartz support. After stabilization of the support at a sufficiently high temperature, the nickel film is deposited in high vacuum, again by evaporation from a high temperature source. In some cases the deposition of nickel is preceded by the deposition of a very thin film of chromium or manganese.

The object of study is the possible presence of nickel aluminate at the interface of nickel and alumina and the influence of chromium or manganese on its formation.

The appropriate technique is X-ray Photoelectron Spectroscopy (XPS). This is a surface technique. But depth profiles of composition and structure can be obtained, as the XPS-apparatus is equipped with an in situ etching facility operating with accelerated Ar^+ -ions.

In order to come to quantitative data a number of standard samples are required with well defined composition and structure. As such we have used Ni-foil and powders of NiO , Al_2O_3 and NiAl_2O_4 . Due to technical reasons chromium and manganese cannot be analyzed separately, so the analysis is confined to nickel and aluminum.

3.2. Preparation of specimens

3.2.1. Alumina substrate

Amorphous alumina films of about 300 nm thick were prepared by reactive evaporation of aluminum from a BN crucible, a technique developed in

our laboratory by P. v.d. Engel [1]. The basic principle is the high affinity of residual oxygen for the film material, aluminum. By increasing the partial oxygen pressure during evaporation of aluminum, both species react and the so formed alumina condenses on a quartz substrate located above the heating stage. The stoichiometry of the condensed alumina depends on several deposition parameters, such as the source-substrate distance, the oxygen pressure and the rate of evaporation. The most sensitive parameter during reactive evaporation is the oxygen vapour pressure. Oxygen is introduced into the reaction chamber through a needle valve connected with the system at the spare gate in the lid of the reaction chamber as can be seen in fig. 2.2.b. The oxygen vapour pressure can be adjusted by leaking the gas into the chamber after high vacuum is achieved. However, at a pressure of 0.1 Pa it is almost impossible to maintain constant pressure; so at 0.133 Pa the evaporation rate was optimized by varying the temperature of the heating source. Stoichiometric alumina films could then be deposited at a temperature of 1473 K, resulting in a deposition rate of 5 nm $\text{Al}_2\text{O}_3/\text{min}$.

Table 3.1. Conditions and results of reactive evaporation of aluminum

oxygen pressure (Pa)	T(K), heating source	Chem. composition
0.0133	1573	Al
0.0665	1573	Al/ Al_2O_3
0.133	1473	Al_2O_3

These results agree well with the conditions reported by Demiryont [2].

After deposition, the alumina layer was subsequently subjected to the same heat treatment as the model catalyst, namely annealing at 1025 K during 100 hrs.

3.2.2. Metal deposits

Chromium or manganese thin films (~ 2 nm) were introduced onto the stabilized γ -alumina film before the nickel film was deposited, just as described in section 2.2.3.2. However, as the nickel films used for these experiments were relatively thick (~ 100 nm), tungsten boats could not be used as heating source for the evaporation of nickel because of alloying between nickel and tungsten. Hence, in order to deposit these films, alumina crucibles were used, heated with a Mo coil. The evaporation conditions were the same as for thin film deposition, that is a temperature of 1623 K and a vapour pressure of 2.6×10^{-4} Pa.

The following thin film composites (T.F.C.) have been prepared and sintered at 973K in hydrogen during 150 hours:

- (1) Ni/ γ -Al₂O₃/SiO₂
- (2) Ni/Cr/ γ -Al₂O₃/SiO₂
- (3) Ni/Mn/ γ -Al₂O₃/SiO₂.

3.2.3. Standard samples

For chromium and manganese the most intense photoelectron peaks coincide with the ill-formed Auger peaks of nickel. Hence chemical analysis is confined to nickel and aluminum compounds.

For the interfacial analysis, first several standards were examined in order to determine parameters such as the binding energy and the sensitivity factor for nickel and aluminum in different chemical states. All the standards were subjected to a severe sputter-etching procedure, to account for preferential sputter effects [3].

The following samples were investigated:

- Ni metal foil;
- NiO powder, Fisher Sci Comp. C.R.;
- Al₂O₃ powder, Ketjen, Alu Grade B;
- NiAl₂O₄ powder [4], prepared by coprecipitation of an aqueous solution of nickel nitrate (0.6 M) and aluminum nitrate (0.3 M) with sodium carbonate at pH = 7, calcined at 1473K in air for 100 hr and characterized with X-ray Diffraction.
- NiAl₂O₄ TFC, prepared by calcining a Ni/ γ -Al₂O₃/SiO₂ composite at 1473 K in air for 150 hr.

3.3. The X.P.S.-method

3.3.1. Principles

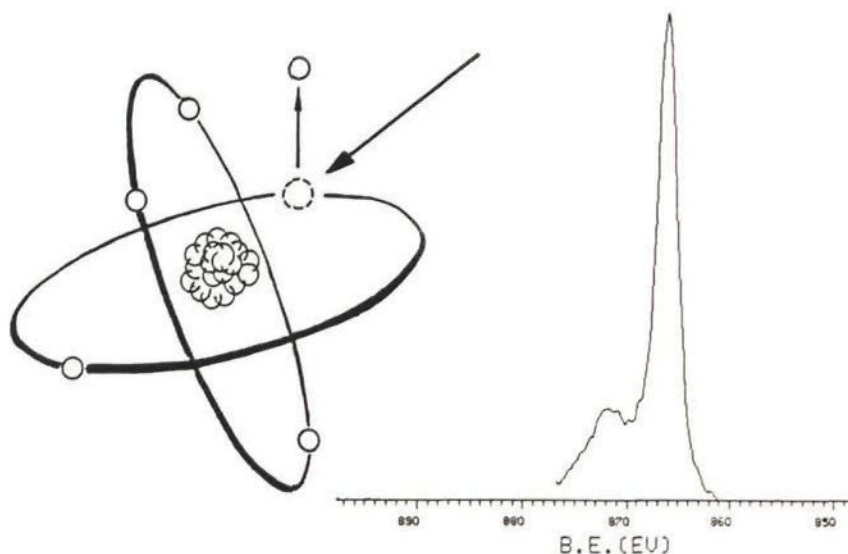


Fig. 3.1. Schematic representation of the ionization process.

X-ray Photoelectron Spectroscopy is based on the photoelectron effect as illustrated in fig. 1. During exposure of a sample to an X-ray beam, MgK α radiation (1253.6 eV), electrons are ejected from the material with a kinetic energy characteristic for the atoms or ions within the sample

$$E_k = h\nu - E_f + E_i = h\nu + E_b \quad (1)$$

where $h\nu$ is the photon energy, E_i and E_f the initial and final energy of the atom/ion and E_b the binding energy of the electron. The released electrons are analyzed with a "double cylindrical mirror analyzer" (Perkin Elmer (ϕ)15-255G), while the data are taken and collected on line with a VG Datasystem resulting in a spectrum as shown in fig. 3.2.

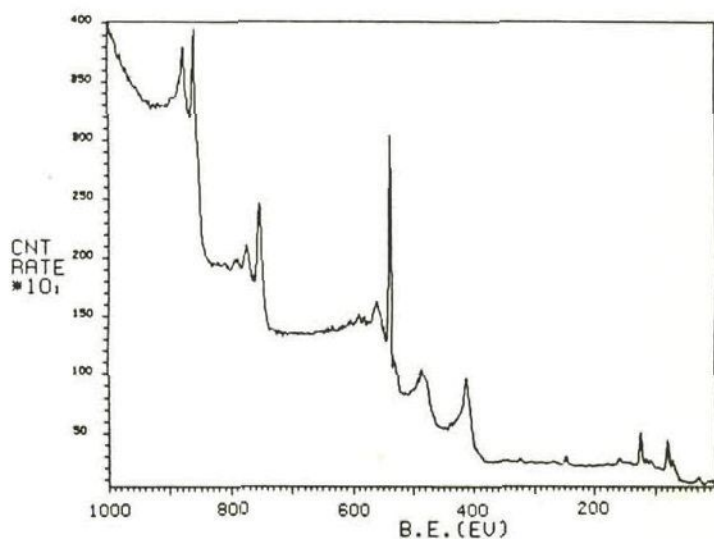


Fig. 3.2. Example of an overall spectrum.

The spectra have some special features common for XPS-spectra, which are important for the quantitative as well as the qualitative analysis:

- The photoelectron peak, the intensity of which is proportional to the cross section for photoionization of the electron concerned. As the cross section is greater for electrons with a higher binding energy than for electrons of lower binding energy, the peaks in the higher binding energy region are more pronounced than in the lower region.
- The basis of the spectrum increases discontinuously from low to high energy after each photoelectron peak. This is caused by loss of kinetic energy, suffered by the electrons during their path through the sample. Background determination is one of the most important operations in quantitative analysis.
- Several peaks are broadened or have a fine structure, arising from coupling of the spin and the orbital angular momentum. For a shell of $l > 0$, two subshells arise with quantum numbers $j = l \pm 1/2$, while the occupancy and thus the relative intensities of the photoelectron lines are $2l$ and $2l + 2$, respectively. For the quantitative analysis all peaks have to be taken into account.

- In the spectrum satellites can appear at the high binding energy side of the photoelectron peak. As can be seen from eq. (1), the final state determines the binding energy of the photoelectron. There are occasions where the vacancy formed by excitation of the electron interacts with the valence electrons, leading to a multitude of final states with higher binding energies.
- Apart from photoelectrons also Auger electrons are measured. After photoionization, the vacancy formed in one of the sub shells of the atom/ion may be filled by a non-radiative Auger process. This readjustment takes place by an electron from a less tightly bound orbital filling the hole, while a second electron - the Auger electron - is ejected.

Chemical information can be gained with XPS, because the binding energy of a photoelectron is determined by the total electrostatic environment. This includes not only the valence shell but all the other atoms/ions in the molecule or solid. The binding energy difference between the photoelectron of an atom/ion A in a molecule or solid and the free atom, the so called chemical shift, can be given as:

$$E_A = k\Delta g_A + \sum_{B \neq A} \frac{g_B}{r_{AB}} \quad (2)$$

where k is the electrostatic integral, g_A and g_B the charges on atom/ion A respectively B and r_{AB} the distance between A and its neighbours B. This relation clearly illustrates the effect of the net charge on ions and the chemical environment on the chemical shift.

Besides this shift, photoelectron peaks can also shift to higher binding energy because of charging up of the sample, especially when dealing with insulators such as alumina. This shift can be measured by calibrating the spectrum with the binding energy of a well known contaminant peak, for instance the carbon peak.

Because of the small mean free path of the ejected electrons in the solid, this technique is very surface sensitive. Only the topmost layers, some few atomic layers thick, are analyzed.

To obtain in depth chemical information, the sample is etched by sputtering with Ar^+ ions using a Perkin Elmer ion gun model 04-161 at an Ar^+ pressure of 6.67×10^{-3} Pa and operating conditions lkeV, 30 mA. This process, however, is rather severe and can introduce artefacts such as preferential and selective sputtering, while grain boundaries will be etched more easily than the grains. During sputter etching high energetic Ar^+ -ions remove material from the surface by ejecting atoms or ions from the crystal as shown in fig. 3.3.

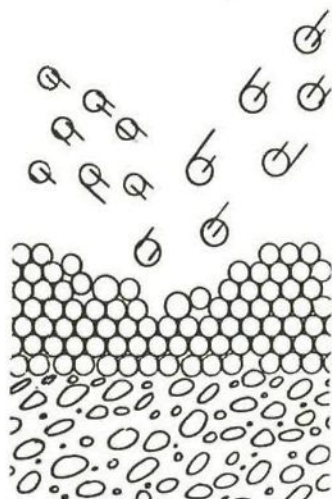


Fig. 3.3 Schematic representation of ion sputter etching.

The rate at which this process will occur depends on the binding energy. Therefore, a material with a low binding energy will sputter faster than those with high binding energies. When both such compounds are present in a sample, selective sputtering will lead to enrichment of the sample with the high binding energy compound. On the other hand, in a one component sample preferential sputtering of one of the consisting elements can lead to a change in the chemical composition of the compound. For instance, preferential sputtering of oxygen in nickel oxide may lead to reduction of the material. All these processes have to be taken into account when using ion sputter etching during analysis.

3.3.2. Evaluation of X.P.S. data

Determination of the quantitative composition by measuring the relative intensities, was carried out as described by C.D. Wagner [5]. The counting rate detected in a photoelectron peak from an element in a thick homogeneous sample, is given by:

$$I = n.A.f.\phi.T.\lambda.C.\sigma.y \quad (3)$$

where n is the number of atoms per unit volume.

The parameters can be divided in three groups:

- Instrumental parameters, for which it is assumed that they are constant, although usually not known.

A: surface area from which photoelectrons are detected.

f: photon flux, which can vary with time.

ϕ : angular correction factor.

- Factors, sensitive to kinetic energy.

T: inherent efficiency of detection by the spectrometer

λ : mean free path for the photoelectron in the sample medium.

C: fractional efficiency of emergence through a contaminating adsorbed layer.

- Factors determined by the photoelectric process.

σ : cross section per atom for photoionization of the particular level.

y: photoelectron yield, the fraction of photoelectric transitions that results in an ion in the ground state and a photoelectron of the appropriate kinetic energy.

Because the instrumental parameters are usually not known, relative intensities are used for the analysis:

$$\frac{n_1}{n_2} = \frac{I_1}{I_2} \cdot \frac{T_2 \lambda_2 C_2 \sigma_2 y_2}{T_1 \lambda_1 C_1 \sigma_1 y_1} = \frac{I_1}{I_2} \cdot S \quad (4)$$

where S is a sensitivity factor which can be calculated. Wagner has shown that the effect of the kinetic energy sensitive factors can be given as:

$$\frac{T_1 \lambda_1 C_1}{T_2 \lambda_2 C_2} = \left[\frac{E_1}{E_2} \right]^{-0.25} \cdot \exp [35.6(E_2^{-0.75} - E_1^{-0.75})] \quad (5)$$

Using cross sections calculated by J.H. Scofield [6], while the photoelectron yield is assumed to be unity, S can be calculated.

However, C.D. Wagner has demonstrated that the above mentioned assumptions do not apply to e.g. transition metals and zeolites. He ascribed this deviation to the probability of shake up and shake off phenomena (satellites) in the photoelectron process, leading to a lower photoelectron yield. This problem can be overcome by including the intensity of all peaks originating from secondary photoelectron processes.

The sensitivity factor "S" can also be determined experimentally by using standards of the starting materials and the compounds to be expected.

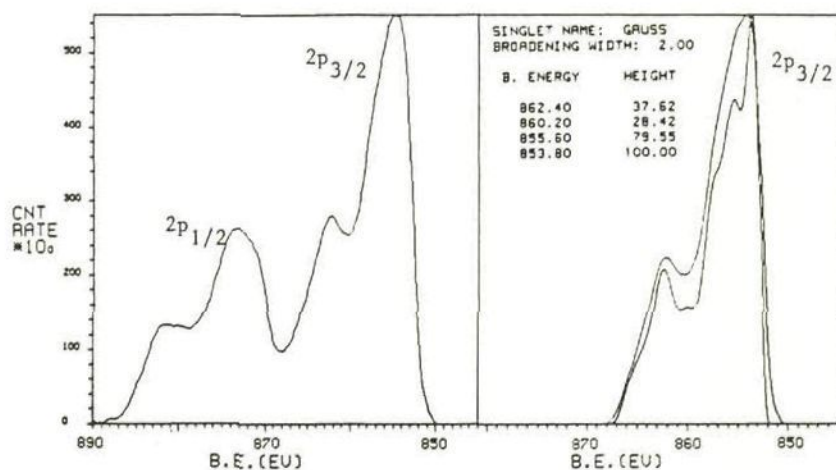


Fig. 3.4. Detail of the combined Ni⁰ and NiO XPS-spectrum.

But also in this case, secondary peaks must be included in the peak area measurements because of the varying intensity of these peaks with the chemical state. This feature is often used for the chemical identification of nickel compounds as will be discussed later.

When several nickel compounds are present, the photoelectron peaks as well as the secondary peaks of the different species may overlap and a deconvolution program [7] is used for separation as can be seen in fig. 3.4.

This technique is very convenient for the large photoelectron peaks. For the smaller and usually less well defined secondary peaks it is hard to determine the contribution of the different species present. To overcome this problem, for all nickel standards the ratio of the area of the total $2p_{3/2}$ -spectrum to the photoelectron peak is determined as:

$$X_c = \frac{I(2p_{3/2})}{I(p.e)} \quad (6)$$

Using this factor and the measured intensities of the deconvoluted photoelectron peaks ($I_{p.e}$), the total peak area, $I(2p_{3/2})$, for the different species present in the sample can be calculated.

A specific problem is met in the spectrum of aluminum by the presence of nickel. The low energy nickel peak overlaps the low binding energy side of the Al peak. This overlap is smaller in the case of the Al(2s) level as compared with the Al (2p) peak. So the use of Al(2s) prevails over the somewhat more intensive Al(2p) peak. At low aluminum concentration even for Al(2s) separation is still impossible, see fig. 3.5. In this case an indirect route is used to determine the peak area of the Al-peak.

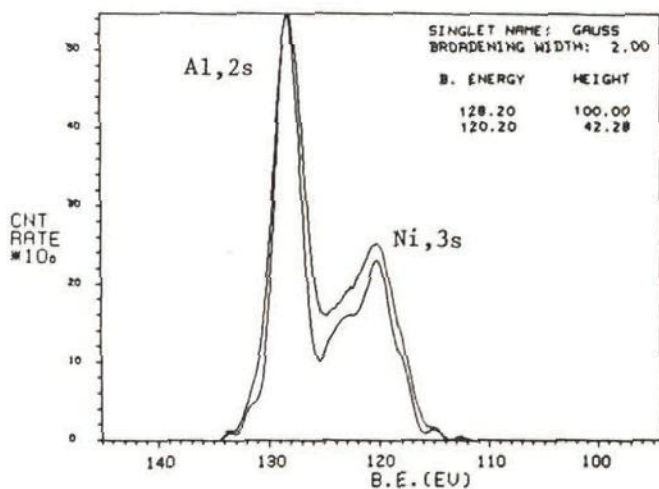


Fig. 3.5. The overlap of the low binding energy Al and Ni peaks.

Using the nickel standards, also the intensity ratio of the Ni(2p_{3/2}) to the measured Ni(3s) peak is calculated as:

$$X_{Ni} = \frac{I(2p_{3/2})}{I(3s)} \quad (7)$$

Subsequently this ratio is used to determine the intensities of the Ni(3s) peak from the calculated Ni(2p_{3/2}) peaks of the composites. Substraction of this area from the combined peak results in the Al intensity.

$$\begin{aligned} I(Al, 2s) &= I(Ni, Al) - X_{Ni} I(2p_{3/2}) \\ &= I(Ni, Al) - X_{Ni} X_c I(p.e.) \end{aligned}$$

Analysis is then carried on as follows:

- the chemical composition is determined with the binding energy of the measured photoelectron peaks.
- for all elements(ions) present the relative amount with respect to oxygen is calculated, using the measured or evaluated peak intensities with their appropriate sensitivity factors, as discussed before, as:

$$\frac{n_e}{n_0} = S_e \cdot \frac{I_e}{I_0} \quad (8)$$

where e is the element considered and 0 is oxygen.

- Combining both results then leads to a semi-quantitative composition of the sample.

3.4. Results and discussion

3.4.1. Standard samples

3.4.1.1. Binding energies

The results for the standards are shown in table 3.2 and fig. 3.6. All peaks separated from the Ni (2p_{3/2}) spectra by deconvolution, are gathered under the heading satellites, the intensities are given in brackets. The uncertainty of the binding energy measured is felt to be of the order of ± 0.2 eV. As there can exist a discrepancy in the measured values at different laboratories of 1 eV, the binding energies

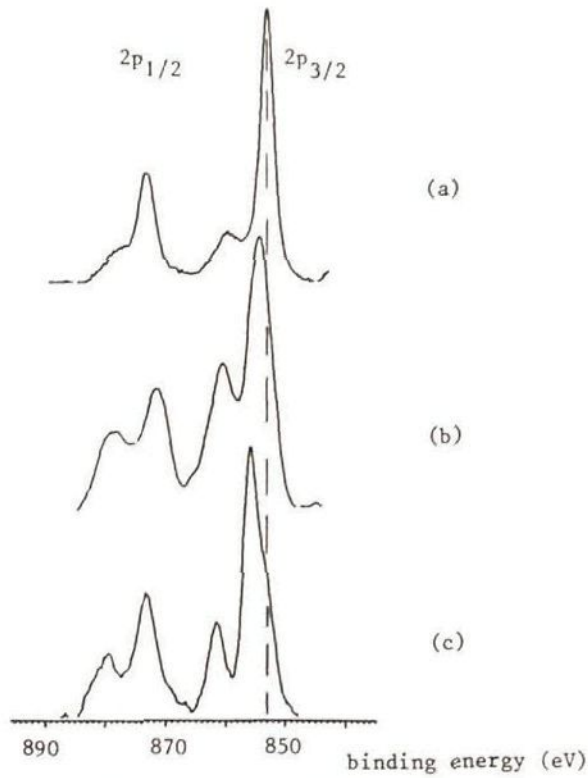


Fig. 3.6: Ni-2p spectra for different nickel compounds.

a = Ni-metal, b = NiO powder, c = NiAl₂O₄ (TFC)

Table 3.2. Binding energies as measured for the different standard samples.

Sample	Ni(2p _{3/2})	Satellites		O(1s)	Al(2s)
Ni-metal	853.0 (100)	855.8 (13)	859.0 (13)		
NiO powder	854.6 (100)	861.6 (61)	866.8 (22)	529.8	
NiAl ₂ O ₄ - powder	856.2 (100)	862.0 (42)	864.8 (21)	531.0	118.8
NiAl ₂ O ₄ - T.F.C.	855.8 (100)	862.0 (44)	864.4 (20)	531.4	118.8
Al ₂ O ₃ powder				531.8	119.6

are in reasonable agreement with those found in literature [8-10]. However, the aluminum and oxygen binding energies in nickel aluminate are felt to be low.

The spectra, given in fig. 3.6, illustrate the characteristic features of the satellites for the different nickel compounds, viz. a small satellite for nickel metal and a relatively large satellite for nickel oxide with that of nickel aluminate in between. The relation between the binding energies and the peak intensities measured is used for identification of the species present in the aged samples.

3.4.1.2. Sensitivity factor

The sensitivity factors were evaluated in both ways, as discussed in section 3.3.2, and have been listed in table 3.3. For aluminum there was a slight difference (~7%) between the calculated and experimental factor while no dependency on the chemical state was found. This was somewhat different for nickel. In contrast with nickel oxide, which shows a good agreement between the calculated and experimental factor, nickel aluminate displays a relative high measured sensitivity factor, low photon yield, especially for the powder samples.

Table 3.3. Calculated and experimental sensitivity factors with regard to oxygen, for the different standard samples.

Sample	S Nickel		S Aluminium	
	Calculated	Measured	Calculated	Measured
NiO powder	0.2	0.2		
NiAl ₂ O ₄ powder	0.2	0.58	4.4	4.1
NiAl ₂ O ₄ , T.F.C.	0.2	0.28	4.4	4.1
Al ₂ O ₃ powder			4.4	4.1

3.4.1.3. Preferential sputtering

The aluminates analyzed not only show low photon yields, but also reduce readily by sputter-etching. They even reduce to a greater extent than the nickel oxide powder, as can be seen in table 3.4.

Table 3.4. Percentages of non-reduced standard material after several treatments by sputter etching, using Ar⁺ ions (1keV, 30 mA)

Duration of total sputtering (min)	NiO powder	NiAl ₂ O ₄ powder	NiAl ₂ O ₄ film
1	79	59	
2		40	30
3		23	
5	63		25
10			20
15	59	21	16
40	59	21	16

3.4.2. Thin film composites (T.F.C.)

In depth analysis of the composites was carried out by Ar⁺-ion sputter-etching. The first data given in table 3.5 to 3.7 and in fig. 3.7 to 3.10 represent the last measurements of the series, where only nickel metal could be detected. So the series of data start at the point where only a nickel overlayer, slightly thicker than the mean free path of the ejected electrons in the solid, is present.

As soon as the topmost layer becomes thinner than the mean free path of the ejected electrons in the solid, the underlying layer becomes accessible for analysis. From this point on the artefacts as discussed in section 3.3.1 become troublesome. This means that the intermediate layer, if present, and the support start to be etched before the nickel overlayer is removed completely. However, as nickel metal is etched more easily than aluminate or alumina, selective sputtering will ensure a further decrease of the nickel content. Simultaneously, preferential

sputtering of an intermediate species, if present, can change the composition during analysis.

The interface is now defined as the point at which the concentration of the nickel metal and the alumina match.

3.4.2.1. T.F.C.1, Ni/Al₂O₃

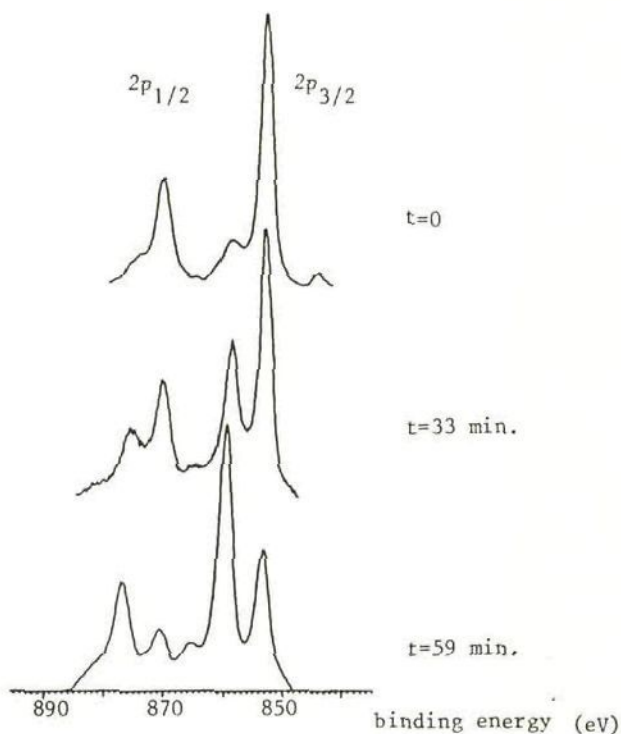


Fig. 3.7. XPS spectra of the Ni- Al_2O_3 interface of sample T.F.C.1 as measured after successive sputter periods.

The spectra of the boundary layer of this sample are given in fig. 3.7. At the stage that alumina is detected, a second nickel peak at about 6 eV higher appears. From the characteristic features, that is the energy difference between the Ni ($3p_{1/2}$) and ($3p_{3/2}$) photoelectron peak and the intensity ratio (X_c), it appears to be a metallic peak. The large shift must be caused by different sample charging. During subsequent sputtering the low energy nickel photoelectron peak decreases while the second one increases.

Table 3.5. Binding energies of the species in sample T.F.C.1, with the semi-quantitative composition in molar percents in the brackets.

Total sputter-time (min)	Ni(2p _{3/2})		Al ₂ O ₃	
			O(1s _{1/2})	Al(2s)
0	853.8			
	(100)			
30	853.8	852.0	531.8	120.0
	(69)	(17)	(14)	
33	853.8	852.2	531.8	120.0
	(58)	(22)	(20)	
39	853.8	852.2	531.8	119.6
	(41)	(28)	(28)	
44	853.8	852.4	531.8	119.6
	(33)	(33)	(34)	
59	853.8	852.6	531.8	119.8
	(15)	(25)	(60)	
90	853.6	853.0	531.8	119.6
	(9)	(9)	(82)	
170	853.8	852.6	531.8	119.4
	(2)	(6)	(92)	

Because of the rather complex nature of the spectra, no direct information could be gained about the formation of nickel aluminate. During the analysis no C-contamination was detected, so the energy of the original nickel photoelectron peak is not corrected for charging up. This is done consequently for the total duration of the analysis and the energy as measured is listed in table 3.5.

Reaching the boundary, it is assumed that the low energy peaks evolving have to originate from the alumina and therefore the correction of the binding energy of both the aluminum and the second nickel peak for charging up was performed with O(1s_{1/2})-Al₂O₃ as reference. The evaluated binding energies and the semi-quantitative

composition are given in table 3.5.

The sputter profile of T.F.C. 1 is shown in fig. 3.8. The second nickel species in this sample exhibits a maximum concentration at the boundary. After the point of intersection of the metal and support profile the relative concentration of this species is higher than the metal concentration.

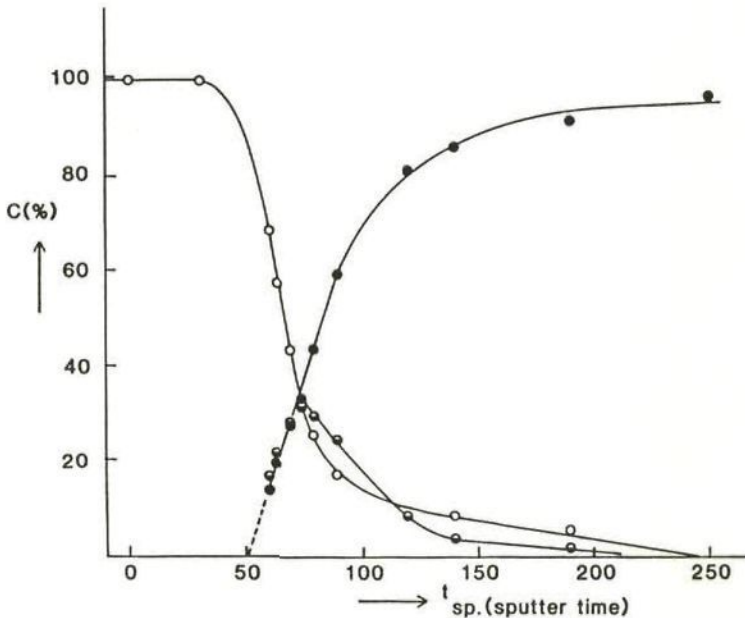


Fig. 3.8. Sputter profile of the Ni-Al₂O₃ thin film composite.

3.4.2.2. T.F.C.2, Ni/Cr/Al₂O₃

The spectra of the sintered sample T.C.F.2, representing the composition of the boundary layer after successive sputtering periods are given in fig. 3.9. A slight broadening of the Ni(2p_{3/2}) photoelectron peak can be seen, upon reaching the alumina layer. This indicates the presence of an intermediate species at the nickel-alumina interface.

The binding energies as determined by using the Ni (2p_{3/2}) peak to correct for sample charging, have been given in table 3.6. Table 3.7 and fig. 3.10 show the evaluated composition of the sample without correction for reduction during sputtering.

Table 3.6. The binding energies of sample T.F.C.2, corrected for sample charging with Ni ($2p_{3/2}$), in brackets binding energies corrected with $O(1s)-(Al_2O_3)$.

Total duration of sputtering (min)	Ni(p.e)	Ni satellites			$O(1s_{1/2})$	Al(2s)
0	853.0	855.8	---	859.2		
60	853.0	856.2	857.8	859.8	533.0	120.8
			(856.6)		(531.8)	(119.6)
65	853.0	856.0	857.4	859.6	532.8	120.6
			(856.4)		(531.8)	(119.6)
85	853.0	856.4	857.8	858.4	532.4	120.2
			(857.2)		(531.8)	(119.6)
125	853.2	855.4			(531.8)	(119.8)
205	853.2	854.8			(531.8)	(119.6)

Table 3.7. Semi-quantitative composition of the boundary layer of T.F.C.2 in molar percents.

Total duration of sputtering (min)	Ni	Intermediate species	Al_2O_3
0	100		
60	64	12	24
65	55	8	37
85	31	5	64
125	8		92
205			~100

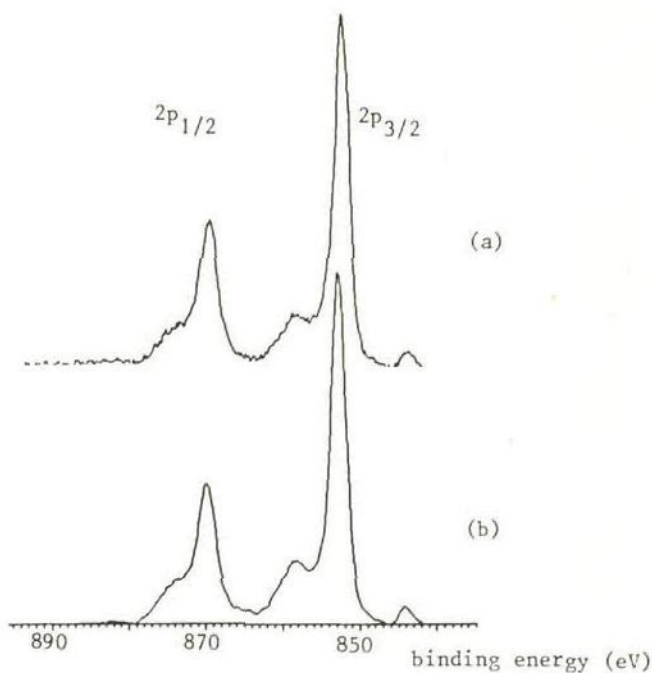


Fig. 3.9. XPS spectra of sample T.F.C.2 of the Ni overlayer (a) and the NiAl_2O_3 boundary (b).

As said before, the broadening of the Ni ($2p_{3/2}$) peak after sputtering for 60 minutes is ascribed to the appearance of an additional peak at 857.8 eV. Simultaneously with this peak, in the low energy region the oxygen and the aluminum peaks of alumina develop, having binding energies of 533.0 and 120.8 eV, respectively. From table 3.2 it can be seen that all evaluated energies for the nickel and the alumina components are too high. Now, as it is very likely that the support is approaching, these high values must be caused by a different charging up of the alumina. Therefore the energy shift of the oxygen, O (1s), peak of alumina is used to correct the measured energy of the evolving peaks, although the choice is rather arbitrary. From table 3.6 it can be seen that even after the second correction, the binding energy for the additional nickel compound of 856.6 eV is rather high as compared with that of the standards.

During further etching the nickel peak decreases while the Al(2s) peak increases with both materials still charging up differently. After 125 minutes sputtering analysis, the second nickel photoelectron peak cannot be distinguished reliably anymore from the nickel metal peak.

In fig. 3.10 the evaluated sputter profile for this sample is given. From the figure it can be seen that at the Ni-Al₂O₃ interface three different species are present, that is, the nickel metal, the alumina and an intermediate species. The concentration of the intermediate species attains a maximum before the concentration of nickel equals that of alumina.

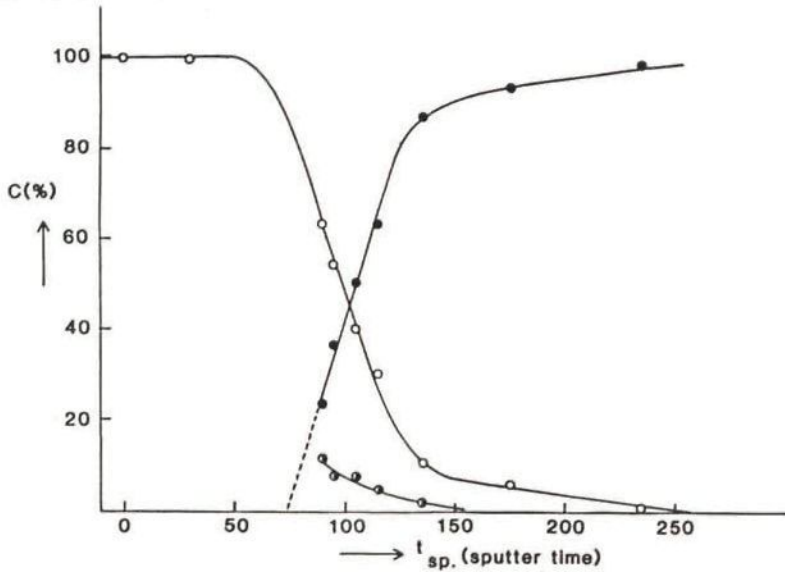


Fig. 3.10. Sputter profile of the Ni/Cr/Al₂O₃ composite (T.F.C.2).

3.4.2.3. T.F.C.3, Ni/Mn/Al₂O₃

- At the nickel alumina interface no intermediate species could be detected.

3.4.3. Discussion

3.4.3.1. NiAl₂O₄ standards

Both nickel aluminate samples used as standard material (coprecipitate and T.F.C.) showed a different behaviour in our analyses than reported in literature [8] viz:

- a low photon yield, less dramatic for the T.F.C. sample.
- a low binding energy and some broadening of the photo electron peak.
- a high reducibility during sputter etching

During analysis a high background was observed, indicating shielding of the species by another material leading to a reduced photon yield. As only aluminum, oxygen and nickel were detected, a toplayer -if present- has to consist of NiO or Al_2O_3 . The presence of some nickel oxide, having a lower binding energy than nickel aluminate, then could explain the rather low nickel binding energy measured and could also account for the broadening of the photo electron peak of the aluminate. However, also the model of a solid solution of nickel oxide in alumina used by P. de Korte [11] in his investigation of the structure of coprecipitated nickel aluminates, could account for the phenomena observed.

Although the two standard samples were prepared in different ways, they show the same enhanced reducibility. Even more, they reduce more easily than nickel oxide during Ar^+ ion sputtering. Because of the higher binding energy in nickel aluminate than in nickel oxide, nickel oxide is expected to reduce to a higher degree than the aluminate. This is also reported in literature [8] for commercial nickel aluminate. Hence, the concept of a NiO layer has to be ruled out, and it is therefore assumed that at the surface the standards are a solid solution of nickel oxide in alumina, which is apparently instable under Ar^+ ion bombardment.

Because of the problems encountered no correction was carried out for reduction in the semi-quantitative analysis of the thin film interface.

3.4.3.2. Thin Film Composites

XPS-analysis of the Ni- Al_2O_3 interfaces have shown that three different boundary layers are formed during heat treatment of the three thin film composites. In contrast to both the Ni/ Al_2O_3 and the Ni/Cr/ Al_2O_3 systems in which an intermediate layer is formed (table 3.5 and 3.6) no such intermediate layer could be detected in the Ni/Mn/ Al_2O_3 system. The intermediate layers in Ni/ Al_2O_3 and Ni/Cr/ Al_2O_3 differ in composition as well as in location with respect to the boundary. The systems investigated are schematically represented in fig. 3.11 and will be discussed in detail.

• After heat treatment:

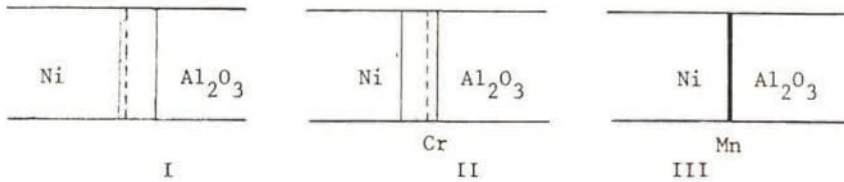


Fig. 3.11. Schematic representation of the Thin Film Composites:

I: Ni/Al₂O₃; II: Ni/Cr/Al₂O₃; III: Ni/Mn/Al₂O₃.

I. The Ni/Al₂O₃ composite

In this system, at the boundary, a nickel metal species is detected. The concentration depth profile (fig. 3.8) shows that the maximum concentration of this species is located at the intercept of the nickel metal and the alumina profile. As it is assumed, as discussed in section 3.4.2, that the intercept of the concentration profiles reflects the position of the interface, it is most likely that the boundary layer is adjacent to the nickel film while extending into the alumina layer. As diffusion of nickel metal atoms into the support is not likely to occur, the species detected must originate from a nickel compound which reduces easily reducing upon sputtering.

From our experience, nickel oxide reduces up to an amount of 40% only by sputter etching (table 3.4). As no residual oxide was found, the intermediate species is more likely to be similar to the "easy to reduce" nickel aluminate, also present in our standard samples. So, our observations indicate that during heat treatment of the nickel alumina composite a diffusion layer consisting of a solid solution of nickel oxide in alumina is formed, as illustrated in fig. 3.11.

II. The Ni/Cr/Al₂O₃ composite

The species detected in this system is characterized by a binding energy of 856.6 eV (table 3.6) which is in between the binding energy of the nickel aluminate standards (table 3.2) and that of commercially available "hard to reduce" nickel aluminate (857.2 eV, [8]). The location of this boundary is rather different from that in the

composite without chromium, as can be seen in fig. 3.10. Here, the maximum concentration of the intermediate species occurs before the interface of $\text{Ni-Al}_2\text{O}_3$ is reached, suggesting that in this composite the boundary layer is adjacent to the alumina layer while extending into the metal film.

Now, concerning the chemical composition of this layer, the problem is somewhat complicated, as the interface was supplied with chromium, which could not be studied by XPS. First, there is the possibility of alloying between nickel and chromium. However, this compound would have a binding energy only slightly higher than that of nickel metal, hence it can be ruled out. Secondly, as during preparation of the composites some oxidation can occur, formation of nickel chromate has to be considered. At this point XPS analysis fails and no unambiguous analyses can be made of the chemical composition of the boundary layer.

Anyhow, it is certain that the presence of chromium prevents the diffusion of nickel ions into the alumina and the consequent formation of an intermediate aluminate.

III. The $\text{Ni/Mn/Al}_2\text{O}_3$ composite

No intermediate species could be detected; there seems to be a sharp transition between the nickel metal and the alumina layer, formed by the manganese boundary layer.

3.5. Conclusions

- During heat treatment of a $\text{Ni}/\gamma\text{-Al}_2\text{O}_3$ thin film composite at 973 K in hydrogen, a boundary layer arises from the interface consisting of a solid solution of nickel oxide in alumina which extends into the alumina layer.
- The observed boundary layer is in good agreement with the XRD and XPS analysis of coprecipitated and impregnated $\text{Ni/Al}_2\text{O}_3$ catalysts, reported by R.B. Shalvoy [8] and M. Wu [9], respectively. After calcining at 873 K these authors report that both types of catalysts contain amorphous NiAl_2O_4 , persisting after reduction in hydrogen at 673 K.

- Introduction of a chromium or manganese intermediate film prevents the diffusion of nickel ions into alumina.
- The use of chromium, as an intermediate film probably leads to the formation of a stoichiometric nickel chromate boundary layer.

3.6. References

- [1] P. v.d. Engel: Graduation Report (1983).
- [2] H. Demiryont; N. Tezey: Thin Solid Films 101 (1983) 345.
- [3] J.W. Coburn: I. Vac. Sci. Technol. 13 (1976) 1037.
- [4] P. de Korte: Private communication.
- [5] C.D. Wagner: Anal. Chem. 49 (1977) 1282.
- [6] J.H. Scofield: J. Electron Spect. Rel. Phen. 8 (1976) 129.
- [7] Carley & Joyner: J. Electron Spect. Rel. Phenom. 16, (1979) 1.
- [8] R.B. Shalvoy; P.J. Reucroft: J. Cat. 56 (1979) 336.
R.B. Shalvoy; B.H. Davis; P.J. Reucroft: Surf. Interf. Anal. 2 (1980) 11.
- [9] M. Wu; D.M. Hercules: Amer. Chem. Soc. 83 (1979) 2003.
- [10] P. Lorentz: J. Finster & G. Wendt, J. Electron Spectr. Rel. Phenom. 61 (1979) 267.
- [11] P. de Korte: Thesis (1988) Delft.

4. KINETICS OF THE GROWTH OF INDIVIDUAL PARTICLES

4.1. Introduction

The sintering of a dispersion of nickel particles, under the driving force of difference in vapour pressure of small and large particles, is governed by a number of processes, running partially parallel and partially in series. The overall rate is mainly determined by the fastest of the parallel processes, which, in turn, is governed by its slowest step. Fig. 4.1 gives a schematic representation of the steps, that will turn out to be the most important ones to be discussed in this chapter.

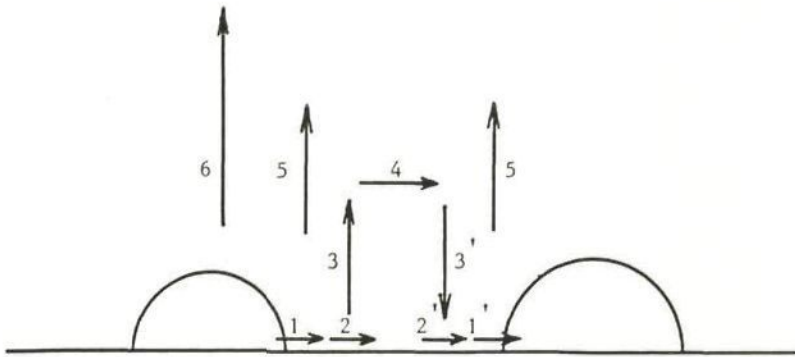


Fig. 4.1. Schematic representation of the growth process

Route I consists of:

Step 1: Spill-over at the edge of a nickel particle, of adsorbed Ni-atoms from the particle onto the alumina surface.

Step 2: Surface migration of Ni-atoms over the alumina surface from one nickel particle to another.

Step 1': Readsorption, at the edge of a nickel particle, of adsorbed Ni-atoms from the alumina surface onto a nickel particle.

Route II consists of:

Steps 1 and 2 as described above.

Step 3: Desorption of adsorbed Ni-atoms from the alumina surface into the gas phase in the vicinity of the alumina surface.

Step 4: Diffusion of Ni-atoms through the gas phase from the area surrounding one nickel particle to the area surrounding another nickel particle.

Step 3': Readsorption of Ni-atoms from the gas phase onto the alumina surface.

Steps 2' and 1', as described above.

Route III consists of:

Steps 6 and 6': Desorption of Ni-atoms from the surface of the nickel particles into the vapour phase and the reverse (readsorption) step. These reaction steps may well compete with the parallel routes I and II.

Finally, part of the Ni-atoms may withdraw from the sintering process by diffusion away from the sample into the container; that is step 5 as indicated in fig. 4.1.

In this chapter some other processes will turn out to be sufficiently fast so as not to influence the rate of the overall process, viz:

Steps 7 and 7': Transition of Ni-atoms from the bulk of the nickel particles to the adsorbed state at the particle surface and the reverse step. These reaction steps will be very fast as compared with the preceding and following steps 1 and 1', respectively.

Step 8 : Migration of Ni-atoms over the surface of the particles towards and from the edges of these particles. Again these steps are fast compared with the following and the preceding steps 1 and 1', respectively.

An exception to the conclusion about step 7' has to be made in the case that the surfaces of the small nickel particles are not rough and more or less spherical, as holds for very small particles, but show facets of low index crystal faces. In that case incorporation of adsorbed Ni-atoms into the crystal lattice occurs by the growth of the crystal faces. Formation of a new lattice layer now requires formation of a two-dimensional nucleus first. The larger the particles, the slower the nucleation step. Thus two-dimensional nucleation can grow into a serious rate limitation of crystal growth.

In the present chapter a thorough analysis will be given of the relative rates to be expected for all reaction steps discussed above. A number of approximations will be made in order to achieve a reasonable basis for the comparison of the competing rates. For the nearly temperature independent pre-exponential factors in the reaction rates, predictions will be based on the most simple version of Eyring's statistical mechanical theory of absolute reaction rates [1, 2]. For the heats of reaction and the activation energies, occurring in the strongly temperature dependent Arrhenius factors of the reaction rates, simple approximations will be made, relating all quantities to the heat of formation of crystalline nickel from its vapour.

In this way the anticipation about the most important steps in the sintering phenomenon, as suggested in fig. 4.1, will be justified and the way will be opened to the overall discussion of the kinetics of the sintering of a dispersion of nickel particles, to be given in the next chapter.

4.2. Approximations for the rates and the equilibria of elementary reaction steps

According to Eyring's theory the rate of a reaction step is equal to:

$$v = \frac{kT}{h} \cdot n^{\ddagger}$$

where n^{\ddagger} is the concentration of the species in the transition state of the reaction. The value of n^{\ddagger} is obtained by assuming the transition state to be in equilibrium with the reaction partners. In turn, equilibrium depends on the condition that the chemical potentials of all species involved are equal. In table 4.1 formulas are presented for the chemical potentials to be used in this stage of the discussion.

In the appendix, following the last chapter of this thesis better approximations for the chemical potentials will be presented and the consequences of their use will be discussed. Also the possibility of mobile adsorption will be considered and its consequences for the reaction rates will be discussed.

Table 4.1. Chemical potentials of nickel in the various states in which it may occur

State of nickel	μ/kT
vapour	$\ln \frac{p}{kT} + \frac{3}{2} \ln \frac{h^2}{2\pi mkT}$
solid	$\frac{h_{\text{bulk}}}{kT}$
adsorbed	$\frac{h_{\text{ads}}}{kT} + \ln n_{\text{ads}} - \ln n_0$
transition state solid adsorbed	$\frac{h_{\text{ads}}}{kT} + \ln n^+ - \ln n_0$
transition state for adsorption and desorption	$\ln n^+ - \ln n_0$
transition state at edge of nickel particles for transfer from nickel to alumina surface and v.v.	$\frac{h_{\text{ads}}(\text{Al}_2\text{O}_3)}{kT} + \ln n^+ - \ln n_e$

where: - h_{bulk} , h_{ads} and $h_{\text{ads}}(\text{Al}_2\text{O}_3)$ are the enthalpy contents per atom

- n_{ads} and n^+ are the atom concentrations per m^2
- n_0 is the number of adsorption sites per m^2
- n_e is the number of adsorption sites along the edge of the particle, per m.
- m is the mass of a nickel atom
- it is assumed, that n^+ and $n_{\text{ads}} \ll n_0$

These formulas are approximations, based on several assumptions, viz.:

- the contributions due to vibrational entropies are throughout negligible
- all adsorptions are strictly localized
- the steps involved do not require extra activation energies

Here the data of table 4.1 will be used. In doing so, it is explicitly considered, that the net rate of a reaction step is always the difference between a forward and a reverse rate; however, both will be presented separately. At equilibrium, forward and reverse rates are equal.

4.2.1. Transfer of nickel atoms between bulk (flat surface) and vapour

- Using the data of table 4.1, the rate of evaporation is found as:

$$v_e = n_0 \frac{kT}{h} \exp \left[-\frac{h_{\text{bulk}}}{kT} \right], \text{ in at. m}^{-2}\text{s}^{-1} \quad (1)$$

where the subscript e stands for evaporation. The frequency factor kT/h is of the order of infra-red vibration frequencies ($\sim 10^{13}\text{sec}^{-1}$).

It is assumed that evaporation does not require an extra activation energy.

- Analogously, the rate of condensation is found to be:

$$v_c = n_0 \frac{kT}{h} \frac{p}{kT} \left[\frac{h^2}{2\pi m kT} \right]^{3/2} \text{ at m}^{-2}\text{s}^{-1} \quad (2)$$

where the subscript c stands for condensation.

In this case the activation energy for incorporation in the crystal is neglected.

The equilibrium vapour pressure follows from $v_e = v_c$ as:

$$p_\infty = \left(\frac{2\pi m kT}{h^2} \right)^{3/2} kT \exp \left[-\frac{h_{\text{bulk}}}{kT} \right] \text{ Nm}^{-2} \quad (3)$$

4.2.2. Transfer of nickel atoms between bulk and adsorbed state

With the assumptions underlying table 4.1, the forward rate is:

$$v_1 = n_0 \frac{kT}{h} \exp \left[-\frac{h_{\text{bulk}} - h_{\text{ads}}(\text{Ni})}{kT} \right] \text{ at. m}^{-2}\text{s}^{-1} \quad (4)$$

and the reverse rate:

$$v_2 = n_{\text{ads}} \frac{kT}{h} \text{ at. m}^{-2}\text{s}^{-1} \quad (5)$$

The adsorption equilibrium follows from $v_1 = v_2$:

$$n_{\text{ads}} = n_0 \exp \left[\frac{-h_{\text{bulk}} + h_{\text{ads}}(\text{Ni})}{kT} \right] \text{ at. m}^{-2} \quad (6)$$

4.2.3. Adsorption and desorption of nickel vapour on and from a flat nickel surface

From the data of table 4.1, the rate of desorption is given by:

$$v_d = n_{\text{ads}} \frac{kT}{h} \exp \left[-\frac{h_{\text{ads}}(\text{Ni})}{kT} \right] \text{ at. m}^{-2}\text{s}^{-1} \quad (7)$$

and analogously the rate of adsorption is:

$$v_a = n_0 \frac{kT}{h} \frac{p}{kT} \left(\frac{h^2}{2\pi m kT} \right)^{3/2} \text{ at. m}^{-2}\text{s}^{-1} \quad (8)$$

where the subscripts a and d stand for adsorption and desorption, respectively.

The adsorption equilibrium then follows from $v_d = v_a$ as:

$$n_{\text{ads}} = n_0 \frac{p}{kT} \left(\frac{h^2}{2\pi m kT} \right)^{3/2} \exp \left[-\frac{h_{\text{ads}}(\text{Ni})}{kT} \right] \text{ at. m}^{-2} \quad (9)$$

4.2.4. Adsorption and desorption of nickel vapour on and from a flat alumina surface

The expressions are similar to those for adsorption of nickel on nickel, with the exception that $h_{\text{ads}}(\text{Ni})$ has to be replaced by $h_{\text{ads}}(\text{Al}_2\text{O}_3)$.

4.2.5. Diffusion to and from a small sphere (embedded in vapour), a small circular disk (in interaction with adsorbed layer) and a flat surface (embedded in vapour)

In a steady state, solution of Fick's equation:

$$J = -D \nabla c$$

for symmetrical situations and boundary conditions, given as:

concentration at $r = c$

at $r_a = c_a$,

leads to the following expressions for the diffusion flux:

- for a 3-dimensional case the total flux is:

$$\phi = 4\pi D r (c - c_a) \frac{r_a}{r - r_a}, \text{ in at. s}^{-1}$$

for $r_a \gg r$:

$$\phi \cong 4\pi D r (c - c_a) \text{ at. s}^{-1} \quad (10)$$

- for a 2-dimensional case the total flux is:

$$\phi = 2\pi D \frac{c - c_a}{\ln r_a / r} \text{ at. s}^{-1} \quad (11)$$

- and for a 1-dimensional case the flux per unit surface area is:

$$\phi = D \frac{c - c_a}{r - r_a} \text{ at m}^{-2}\text{s}^{-1}$$

for $r_a \gg r$:

$$\phi \cong D \frac{c-c_a}{r} \text{ at. m}^{-2}\text{s}^{-1} \quad (12)$$

In the formulas given, the rates of forward and reverse flows are easily distinguished as being proportional to c and c_a respectively.

4.2.6. Migration of nickel atoms over the surface towards the edge of a half sphere of nickel, supported by a flat alumina surface, and the spill-over from the nickel particle to the alumina surface

4.2.6.1.

Redistribution by diffusion of adsorbed nickel atoms contained within a circular circumference, cannot be derived in a general way by solution of Fick's equation. The following rough argument may suffice to find the diffusion flux when the average concentration is n_{ads} , while the concentration at the edge is negligible.

The time constant for diffusion can be defined as:

$$\tau = \frac{\ell^2}{D} = \frac{\pi^2}{4} \frac{r^2}{D}$$

where ℓ is the radius of the half sphere.

The quantity of material to be removed is: $2\pi r \cdot n_{\text{ads}}$. The total flow of material per unit of time then is:

$$\phi = \frac{8}{\pi} D n_{\text{ads}} \quad (13)$$

4.2.6.2.

Again, using the data from table 4.1, the rate of spill-over of nickel atoms from the nickel to the alumina surface is estimated to be:

$$v_1 = \frac{kT}{h} \frac{n_{\text{ads}}(\text{Ni})}{n_0(\text{Ni})} n_e \exp \left[\frac{h_{\text{ads}}(\text{Ni}) - h_{\text{ads}}(\text{Al}_2\text{O}_3)}{kT} \right] \text{ at m}^{-1}\text{s}^{-2} \quad (14)$$

and in the reverse direction, analogously

$$v_2 = \frac{kT}{h} \frac{n_{\text{ads}}(\text{Al}_2\text{O}_3)}{n_0(\text{Al}_2\text{O}_3)} n_e \text{ at. m}^{-1}\text{s}^{-1} \quad (15)$$

Here $h_{\text{ads}}(\text{Ni})$ is supposed to be stronger negative than $h_{\text{ads}}(\text{Al}_2\text{O}_3)$. In equilibrium both rates are equal.

4.2.7. The diffusion coefficients

The diffusion coefficient of nickel vapour in the carrier gas hydrogen can be approximated by the ideal gas formula:

$$D = \frac{2}{3} \frac{(kT)^{3/2}}{\pi a^2 (\pi m p_0)^{1/2}} \text{ m}^2\text{s}^{-1} \quad (16)$$

where a is the collision diameter, assumed to be equal for Ni and H_2 , m is the atomic mass of Ni, and p_0 is the pressure of the carrier gas.

The diffusion coefficient for adsorbed nickel atoms is given by:

$$D = 1/4 \omega a^2 \text{ m}^2\text{s}^{-1}$$

where ω is the average jump frequency and a is the jump distance.

The factor $1/4$ represents the chance, that a jump is in the direction of the concentration gradient.

The jump frequency will be approximated by the absolute rate formula, which leads to:

$$D = \frac{1}{4} \frac{kT}{h} a^2 \exp \left[- \frac{u_{\text{act}}}{kT} \right] \quad (17)$$

The activation energy for jumps, u_{act} , is different for nickel atoms on a nickel surface and on an alumina surface, $u_{\text{act}}(\text{Ni})$ and $u_{\text{act}}(\text{Al}_2\text{O}_3)$, respectively.

4.3. General formulae for growth rates

4.3.1. General remarks

At equilibrium, that is at equal size of the two particles depicted in fig. 4.1, every single step as described before is in equilibrium and hence the rates of the forward and reverse reactions of each elementary step are equal. No net transport will occur. When equilibrium is disturbed, for instance because of the left hand particle in fig. 4.1 being smaller than the right hand particle, a net transport from left to right will occur. The maximum rate such a net reaction can attain just equals the rates of the forward and reverse reactions at equilibrium.

The equilibria of all steps will be disturbed. The largest relative disturbance in a sequence will then be at that step, where the maximum attainable rate is smallest. This step will therefore be the rate determining step. Often it is a fair approximation to assume that the driving force of the reaction is concentrated at the rate determining step, while the deviations from equilibrium at the preceding and following steps are so small, that they can be neglected.

Thus, in trying to find out which of the reaction routes is the preferred one and which of the reaction steps is rate determining in that route, it is important to derive the rates of the forward and reverse reactions of every step in equilibrium. In doing so, it is still important to take into account the particle size at which the equilibrium is considered. Although the radii do not appear explicitly in the formulae derived in section 4.2, all vapour pressures and concentrations of adsorbed species depend on the radii as well as on the crystal faces of the particles considered. Some of the rates are directly proportional to the corresponding nickel vapour pressure p_r or one of the concentrations of adsorbed nickel atoms, $n_{ads}(Ni)$ or $n_{ads}(Al_2O_3)$. For the evaporation or desorption rates the proportionality is less obvious and hidden in the dependence of the heat of formation or heat of adsorption on particle radius. Anyhow, as compared with the rates for flat surfaces, all rates applicable to nickel particles with

radius r , supported by a flat alumina carrier, will be increased by the same factor given by the Kelvin equation:

$$\frac{p_r}{p_\infty} = \exp \left[\frac{2\sigma a^3}{kTr} \right]$$

where p_∞ is the vapour pressure above flat surface, σ the surface free energy (surface tension) of nickel and a^3 the atomic volume of nickel in the solid state.

In calculating the relative rates of the various processes we shall use p_∞ and the corresponding concentrations of adsorbed nickel atoms $n_\infty(\text{Ni})$ and $n_\infty(\text{Al}_2\text{O}_3)$. Then, the real rates at equilibrium at a certain radius r are obtained by multiplying all rates with the same factor:

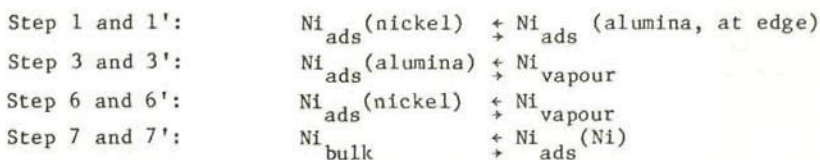
$$\exp \left[\frac{2\sigma a^3}{kTr} \right]$$

The reaction rates presented in section 4.2 still are not directly comparable. Some are expressed as flows per unit surface area, others as flows per unit of length along a circumference and some as total flow towards or from a particle. In order to arrive at a good comparison all rates have to be translated to a common rate constant for the growth of the nickel particles. In the following we have chosen the linear particle growth rate, dr/dt .

Conversion of the growth rates presented in section 4.2 then will require geometric factors, some of which with a different dependence of the particle radius considered.

4.3.2. Formulae for maximum growth rates

The reaction steps given in section 4.1 can be recapitulated as follows:



and the diffusion processes (2), (4), (5) and (8) of Ni-atoms over the alumina surface, in the vapour phase and over the nickel surface.

Using the reaction rates of section 4.2, the maximum growth rates of the various steps, normalized for a flat nickel surface, are obtained as outlined in this section. The results are assembled in table 4.2.

Step 1: $Ni_{ads}(Ni) \rightleftharpoons Ni_{ads}(Al_2O_3)$ (at edge)

The basic rate is taken from equation (14), n_{ads} is given by equation (9), p , in turn, is given by equation (3); n_0 (the concentration of adsorption sites) is approximated by a^{-2} , where a^3 is the atomic volume of bulk nickel; n_e is approximated by a^{-1} . Assuming the nickel particles to be half spheres, the geometric factor, converting a flow per unit length of the particle circumference, $2\pi r$, into a linear growth rate of the particle, turns out to be:

$$2\pi r \frac{a^2}{2\pi r^2} a = \frac{a^3}{r}$$

Step 3: $Ni_{ads}(Al_2O_3) \rightleftharpoons Ni_{vapour}$

The basic rate is taken from (8); again p is substituted as given by (3). In calculating the geometric factor, it is assumed that every nickel particle is connected to a circular area on the alumina surface with radius ℓr . The geometric factor then turns out to be:

$$\frac{\pi \ell^2 r^2}{2\pi r^2} a^3 = \frac{1}{2} \ell^2 a^3$$

where $\pi \ell^2 r^2$ is the area on alumina involved in the adsorption process.

Step 6: $Ni_{ads}(\text{nickel}) \rightleftharpoons Ni_{vapour}$

The basic equations to be used are (8) and (3); the geometric factor connecting a flow per unit surface area to a linear growth rate is a^3 . This step is directly coupled to the diffusion in the gas phase away from and towards the spherical particle. This sub-step will be indicated as 6a and treated below.

Table 4.2. Formulas for maximum rates (in m sec^{-1}) for a number of different steps of the overall sintering process. In order to allow for the curvature of the nickel surface all rates still have to be multiplied by a common factor $\exp [2\sigma a^3/kTr]$.

Step no.	Reaction	Growth rate (dr/dt , m sec^{-1})
1	$\text{Ni}_{\text{ads}}(\text{Ni}) \xrightleftharpoons{\text{at edge}} \text{Ni}_{\text{ads}}(\text{Al}_2\text{O}_3)$	$\frac{a^2}{r} \frac{kT}{h} \exp \left[\frac{h_{\text{bulk}} - h_{\text{ads}}(\text{Al}_2\text{O}_3)}{kT} \right]$
3	$\text{Ni}_{\text{ads}}(\text{Al}_2\text{O}_3) \xrightleftharpoons{\text{Ni vapour}}$	$\frac{1}{2} \ell^2 a \frac{kT}{h} \exp \left[\frac{h_{\text{bulk}}}{kT} \right]$
6	$\text{Ni}_{\text{ads}}(\text{Ni}) \xrightleftharpoons{\text{Ni vapour}}$	$a \frac{kT}{h} \exp \left[\frac{h_{\text{bulk}}}{kT} \right]$
6a	Diffusion through vapour away from and towards nickel particle	$\frac{4\sqrt{2}}{3} \frac{a}{r} \left(\frac{kT}{h} \right)^3 \frac{m}{p_0} \exp \left[\frac{h_{\text{bulk}}}{kT} \right]$
7	Transition of Ni atoms from the bulk to the adsorbed state	$a \frac{kT}{h} \exp \left[\frac{h_{\text{bulk}} - h_{\text{ads}}(\text{Ni})}{kT} \right]$
2	Diffusion over alumina from one particle to another	$\frac{1}{4} \frac{a^3}{r^2 \ln \ell} \frac{kT}{h}$ $\exp \left[\frac{h_{\text{bulk}} - h_{\text{ads}}(\text{Al}_2\text{O}_3) - u_{\text{act}}(\text{Al}_2\text{O}_3)}{kT} \right]$
4	Diffusion through vapour parallel to the alumina surface	$\frac{4\sqrt{2}}{3} \frac{\ell}{\ln \ell} \frac{a}{r} \left(\frac{kT}{h} \right)^3 \frac{m}{p_0} \exp \left[\frac{h_{\text{bulk}}}{kT} \right]$
5	Diffusion through vapour away from the sample	$\frac{2\sqrt{2}}{3} \frac{\ell^2}{L} \frac{a}{r} \left(\frac{kT}{h} \right)^3 \frac{m}{p_0} \exp \left[\frac{h_{\text{bulk}}}{kT} \right]$
8	Redistribution by diffusion over nickel surface	$\frac{a^3}{\pi^2 r^2} \frac{kT}{h} *$ $\exp \left[\frac{h_{\text{bulk}} - h_{\text{ads}}(\text{Ni}) - u_{\text{act}}(\text{Ni})}{kT} \right]$

Step 7: $\text{Ni}_{\text{bulk}} \rightleftharpoons \text{Ni}_{\text{ads}} \text{ (Ni)}$

The basic equation used is (4), n_0 is approximated by a^{-2} and the geometric factor is again a^3 .

Step 6a: Diffusion through vapour away from the spherical surface of the nickel particles.

The total one-sided diffusion flux from the half sphere is given by (10) as:

$$\begin{aligned} \phi &= 2\pi Drc \\ &= 2\pi Dr \frac{p}{kT} \end{aligned}$$

Substituting D from (16) and p/kT from (3), while taking into account the geometrical factor $a^3/2\pi r^2$, this leads to the desired result.

Step 2: Diffusion over the alumina substrate, from one particle to another.

According to equation (11) the maximum flux of adsorbed nickel atoms from the circular edge of a particle is:

$$\phi = 2\pi D \frac{c}{\ln(r_a/r)}$$

while the maximum flux towards a particle is analogously:

$$\phi = 2\pi D \frac{c_a}{\ln(r_a/r)}$$

A reasonable approximation for r_a may be half the average distance between the centres of neighbouring particles and from now on we substitute $r_a/r = \lambda$. The two-dimensional concentration c corresponds to n_{ads} , as used earlier. Introduction of n_{ads} from (9), applied to adsorption on alumina, p from (3) and D from (17) also for alumina, leads to the desired maximum flux. The geometric factor for conversion into a linear growth rate is now $a^3/2\pi r^2$.

Step 4: Diffusion through vapour parallel to the alumina surface.

The basic equation is (11). It is assumed that the diffusion originates in a cylindrical volume with radius r and height ℓr . The flow out of the layer over the substrate with thickness ℓr , is considered to disappear from the sample. The flux is then:

$$\frac{2\pi Dc}{\ln \ell} \ell r$$

The three dimensional concentration c is equal to p/kT as given by (3). The diffusion coefficient is given by (16) and the geometric factor for translation of the flux into a linear growth rate is $a^{3/2}\pi r^2$.

Step 5: Diffusion through vapour, away from the sample.

The basic formula is (12). A good measure for the flow per unit surface area can be obtained by assuming $c_a = 0$ at $r_a = L.r$, where $L.r$ is the radius of the alumina sample. The flow per nickel particle (effective alumina area $\pi \ell^2 r^2$) is then:

$$\phi = \frac{Dc}{Lr} \pi \ell^2 r^2 = \pi \frac{\ell^2}{L} r D c$$

With the same substitutions as in the preceding case and taking into account the geometric factor, the tabulated result is obtained.

Step 8: Redistribution by diffusion over the nickel surface.

The total diffusion flux is given by (13), n_{ads} follows from (9) in combination with (3), the diffusion coefficient is given by (17) and once again the geometric factor is $a^{3/2}\pi r^3$. Combination of these parameters gives the tabulated result.

From the results in tabel 4.2 it is seen, that the pre-exponential factors only contain well known quantities and can therefore be calculated easily. The exponential factors contain a limited number of energy parameters, h_{bulk} , $h_{ads}(Ni)$, $h_{ads}(Al_2O_3)$, $u_{act}(Ni)$ and $u_{act}(Al_2O_3)$. In the next section all these quantities will be expressed in

h_{bulk} , the pre-exponential factors will be calculated and by substitution of an experimental value for h_{bulk} finally quantitative estimates will be obtained for the maximum rates of all individual growth steps.

4.4. Quantitative evaluation of the maximum rates of the individual growth steps

4.4.1. Heats of adsorption, activation energies for diffusion and surface free energies

The nickel crystal has the cubic close packed atom arrangement (f.c.c.) the (111) and (100) faces being the two most stable faces, determining the *equilibrium shapes of large crystals*.

Approximations for all relevant energy parameters can be made, considering nearest neighbour interactions only. This is the line we will follow throughout. In sections 1 and 2 of the appendix, a justification of some of the approximations will be given.

The heat of formation of the crystal from infinitely separated atoms is found by considering the coordination number of the nickel atoms in the crystal, which is 12. As every nearest neighbour bond is shared by two atoms, the heat of formation per atom is $6w$, where w is the energy content of a single bond.

On adsorption on a (111)-face a nickel atom forms three bonds, hence the heat of adsorption per atom amounts to $3w$ (on a (100)-face this would be $4w$).

On diffusion of a nickel atom over a (111)-face it has to pass a transition state, where it is bound to two surface atoms. Hence the activation energy for diffusion is w (on a (100)-face this would be $2w$).

Creating of two (111)-faces by cleavage of a crystal, the number of bonds broken is three per atom in one of the faces. Hence the surface energy per atom is $3/2 w$ (for a (100)-face it would be $2w$). The surface energy per unit of surface area then is

$$\sigma_{(111)}^{\circ} = \frac{3w}{2a^2}$$

Table 4.4. Calculated pre-exponential factors in m s^{-1} , and energy-terms for the different reaction steps as a factor of h_{bulk}/kT .

Reaction step	Reaction	(r in nm)		Energy in exp.
		Pre-exponential factor		
		873 K	973 K	
1	$\text{Ni}_{\text{ads}}(\text{Ni}) \rightleftharpoons \text{Ni}_{\text{ads}}(\text{Al}_2\text{O}_3)$ at edge	$896*r^{-1}$	$998*r^{-1}$	0.793
3	$\text{Ni}_{\text{ads}}(\text{Al}_2\text{O}_3) \rightleftharpoons \text{Ni}_{\text{vapour}}$	$2.02*10^5$	$2.25*10^5$	1
6	$\text{Ni}_{\text{ads}}(\text{Ni}) \rightleftharpoons \text{Ni}_{\text{vapour}}$	4030	4500	1
6a	Diffusion through vapour away from and towards nickel particle	$2.50*10^9*r^{-1}$	$3.40*10^9*r^{-1}$	1
7	Transition of Ni atoms from the bulk to the adsorbed state	4030	4500	0.5
2	Diffusion over alumina from one particle to another	$21.6*r^{-2}$	$24.1*r^{-2}$	0.862
4	Diffusion through vapour parallel to the alumina surface	$1.06*10^{10}*r^{-1}$	$1.48*10^{10}*r^{-1}$	1
5	Diffusion through vapour away from the sample	$1.22*10^5*r^{-1}$	$1.70*10^5*r^{-1}$	1
8	Redistribution by diffusion over nickel surface	$20.1*r^{-2}$	$22.4*r^{-2}$	0.667

Table 4.5. Evaluated linear particle growth rates to be multiplied by r^n , for the various reaction steps (r in nm).

Reaction step	Reaction	$dr/dt(\text{nmh}^{-1}), (111)\text{-face}$		exp. of r
		T = 873 K	T = 973 K	
1	at edge $\text{Ni}_{\text{ads}}(\text{Ni}) \rightleftharpoons \text{Ni}_{\text{ads}}(\text{Al}_2\text{O}_3)$	$2.3 \cdot 109^{-2}$	1.5	-1
3	$\text{Ni}_{\text{ads}}(\text{Al}_2\text{O}_3) \rightleftharpoons \text{Ni}_{\text{vapour}}$	$1.7 \cdot 10^{-4}$	$3.2 \cdot 10^{-2}$	0
6	$\text{Ni}_{\text{ads}}(\text{Ni}) \rightleftharpoons \text{Ni}_{\text{vapour}}$	$3.4 \cdot 10^{-6}$	$6.4 \cdot 10^{-4}$	0
6a	Diffusion through vapour away from and towards nickel particle	2.1	$4.8 \cdot 10^2$	-1
7	Transition of Ni atoms from the bulk to the adsorbed state	$2.2 \cdot 10^5$	$3.2 \cdot 10^6$	0
2	Diffusion over alumina from one particle to another	$1.8 \cdot 10^{-5}$	$1.6 \cdot 10^{-3}$	-2
2, corrected (for $r=1\text{nm}$)		$2.9 \cdot 10^{-5}$	$3.2 \cdot 10^{-3}$	
4	Diffusion through vapour parallel to the alumina surface	9.0	$2.1 \cdot 10^3$	-1
5	Diffusion through vapour away from the sample	$1.0 \cdot 10^{-4}$	$2.4 \cdot 10^{-2}$	-1
8	Redistribution by diffusion over nickel surface	0.27	9.2	-2

For the [100]-face the same data apply, with the exception of those for step 7. The rate at 873 K is now 9.1×10^8 , at 973 K the rate is 5.6×10^9 .

Table 4.5 allows a comparison of the various possible rate determining growth steps. Returning to section 1 of this chapter and the discussion illustrated by fig. 4.1, we are now in the position to check to what extent the various anticipations have been justified. First we consider particles with a radius of 1 nm. Then several conclusions are straight forward.

- Diffusion of nickel vapour away from the nickel particles (step 6a) is very fast as compared with the evaporation of nickel atoms (step 6); hence 6a is irrelevant as a rate determining step.
- Redistribution of adsorbed nickel atoms over the surface of the particles (step 8) is a very fast process.
- Transition of nickel atoms from the nickel bulk to the adsorbed state and vice versa (step 7) is also a very fast process. However, here the proviso holds, that for a well faceted crystal incorporation of the adsorbed nickel atoms may be nucleation inhibited and thus a slow process. This aspect will be considered in the next section.
- The transition of adsorbed nickel atoms from the nickel to the alumina surface at the circumference of the particles (step 1) is also a fast process and no candidate for the rate determining step.
- Direct evaporation of adsorbed nickel atoms from the surface of the nickel particles (step 6) is a slow process as compared with step 2. Hence it is not rate determining. However, with slightly different parameters or particle radii it might take over from step 2.

Two parallel routes remain, indicated as I and II in section 1. The rate limiting steps in these routes appear to be:

- I Transport of nickel atoms by diffusion over the alumina surface (step 2)
- II A sequence of diffusion over the alumina surface (step 2) and desorption from the alumina surface (step 3), followed, after rapid diffusion through the gas phase (step 4), by the reverse steps.

As seen from table 4.5, the diffusion through the gas phase is very fast as compared with the diffusion over the alumina surface. So in principle route II is an effective short cut for route I. The limitation is the rate of desorption and readsorption of nickel from and to the alumina surface. The effect of the short cut will be that the concentration gradient, governed by the surface diffusion, will reach from r to $\ell'r$ closer by than ℓr , as originally. The evaporation, preceding the gas diffusion, then, will originate from the smaller surface $\pi (\ell'r)^2$ as compared to $\pi (\ell r)^2$ originally. ℓ' is found by balancing the resulting rates, i.e by putting:

$$\frac{\pi \ell'^2}{\ln \ell'^2} * 1.7 * 10^{-4} = \frac{\ln \ell}{\ln \ell'} * 1.8 * 10^{-5} \text{ at } 873 \text{ K}$$

and:

$$\frac{\ell'^2}{\ln \ell'} * 3.2 * 10^{-2} = \frac{\ln \ell}{\ln \ell'} * 1.6 * 10^{-3} \text{ at } 973 \text{ K}$$

For $\ell=10$ this leads to $\ell'=4.1$ at 873 K and $\ell'=3.2$ at 973 K with the corresponding rates $2.9 * 10^{-5} \text{ nm h}^{-1}$ and $3.2 * 10^{-3} \text{ nm h}^{-1}$. It can be seen, that the effective rate of diffusion has scarcely changed as compared to the rate of the diffusion of the adatoms over the alumina surface as derived originally.

Accordingly, the calculated values for the rates of the rate determining step 2 of route II can be considered as satisfactory approximations for the growth rates dr/dt .

A disturbing factor, however, is found in step 5, namely the diffusion of nickel through the gas phase away from the sample. The rates of step 5 are found to be slightly greater than the transport rates leading to sintering. This would mean that sintering is always accompanied by a depletion of nickel from the sample. Obviously, it falls to the experiment to decide whether this is a realistic conclusion. Generally no such effect is observed. We shall return to this point in the discussion of the reliability of the models and the parameters chosen in the first two sections of the appendix.

All conclusions derived so far are valid for a particle radius of 1 nm. The rates of the various processes, however, depend in a different way on this radius, which can be seen from the last column of table 4.5. This might influence some of the conclusions. Inspection shows that there are no problems at smaller particle sizes. At larger radii, however, several effects arise:

- The diffusion of nickel vapour away from the sample (step 5) *predominates to a greater extent over step 2.*
- The direct evaporation from the nickel particles (step 6) increases with respect to step 2 and would take over at a particle size of $r = 2.3$ nm at 873 K and $r = 1.6$ nm at 973 K.
- The competition between route I and route II (essentially step 2 and 3) changes more and more in favour of step 3 and hence route II. This effect is more predominant at 973 K than at 873 K.

Definite conclusions about these circumstances are only possible after the consideration of better approximations, to be found in sections 1 and 2 of the appendix. In section 7 of this chapter such conclusions will be recapitulated.

4.5. The role of supersaturation in determining growth rates

So far we have considered the maximum rates of reversible growth steps. All maximum rates depend on the radius of the nickel particles, for which they are considered, by a common factor:

$$\exp \left[\frac{2\sigma a^3}{kTr} \right]$$

In the actual circumstances of the sintering process, we assume that a rate determining step has been identified and that the total driving force is concentrated at that step. Such a driving force is seen as arising from a difference between an average vapour atmosphere (c.q. adsorption density) prevailing in the area or region between the differently sized particles and the vapour pressure or adsorption density corresponding to the particle considered. The net rate is a balance between a forward step, leading to growth, and a reverse step leading to dissolution. The balance is expressed by a factor:

$$\exp \left[\frac{2\sigma a^3}{kTr^*} \right] - \exp \left[\frac{2\sigma a^3}{kTr} \right]$$

where r^* is the radius of particles in equilibrium with the nickel concentration between the particles.

This factor can be converted as follows:

$$\exp \left[\frac{2\sigma a^3}{kTr^*} \right] - \exp \left[\frac{2\sigma a^3}{kTr} \right] = \exp \left[\frac{2\sigma a^3}{kTr^*} \right] \left\{ 1 - \exp \left[\frac{2\sigma a^3}{kT} \left(\frac{1}{r} - \frac{1}{r^*} \right) \right] \right\}$$

Assuming: $\frac{2\sigma a^3}{kT} \left(\frac{1}{r} - \frac{1}{r^*} \right) \ll 1$,

the equation becomes:

$$= \exp \left[\frac{2\sigma a^3}{kTr^*} \right] \left\{ \frac{2\sigma a^3}{kT} \left(\frac{1}{r^*} - \frac{1}{r} \right) \right\} = \frac{2\sigma a^3}{kTr^*} \left(1 - \frac{r^*}{r} \right) \exp \frac{2\sigma a^3}{kTr^*} \quad (22)$$

The factor $(1 - r^*/r)$ is found frequently in literature as governing the growth or dissolution of particles in a dispersion of sizes. Those particles with $r > r^*$ grow, while particles with $r < r^*$ disappear. Most authors [8,9], however, use a series expansion for the exponential such that the factor $\exp \left[\frac{2\sigma a^3}{kTr^*} \right]$ disappears. In the next chapter it will turn out, that interpretation of sintering results is seriously influenced by this omission.

4.6. Nucleation-inhibited growth as a possible rate determining step

Turning to nucleation as an inhibiting factor in growth of crystals with well developed low index faces, supersaturation, as expressed by a factor $(1 - r^*/r)$, is of dominating importance. The driving force for incorporation of adatoms into the crystal structure is the gain in lattice energy. For adatoms on a low index face such a gain materializes only for a two dimensional nucleus of a certain minimum size. Relatively speaking, the gain in energy per atom for a smaller nucleus is less, which is expressed by saying that such a subcritical nucleus has too large an edge energy. The well known nucleation theory, to be summarized below, shows, that both the size of the critical nucleus and the activation energy for its formation, sharply depend on supersaturation. The same sharp influence is shown by the growth rate as limited by nucleation.

Assuming, as stated before, that the nickel particle is a half sphere with radius r , supported by a flat alumina surface, the linear growth rate, as a consequence of nucleation, can be given by:

$$\frac{dr}{dt} = 2\pi r^2 a I_N$$

where I_N is the rate of formation of two-dimensional nuclei of sufficient size per unit area of nickel surface.

On its turn:

$$I_N = Z \phi n^*$$

where n^* is the concentration of critical nuclei per unit surface area, and ϕ the flux of nickel atoms towards the circumference of the nucleus and Z , the Zeldovich nonequilibrium correction factor, which is dimensionless and of the order of unity.

The following values may be substituted:

$$n^* = n_0 \exp \left[- \frac{\Delta G_{cr}}{kT} \right]$$

where n_0 is the concentration of surface sites ($= a^{-2}$);
 ΔG_{cr} the free energy of formation of a critical nucleus at the prevailing concentration of adatoms (i.e. at the prevailing supersaturation).

$$\phi = 2\pi D \frac{n_{ads}}{\ln \lambda} \quad (\text{see eq (11), section 4.2.5})$$

where $D = \frac{1}{4} \frac{kT}{h} a^2 \exp \left[- \frac{u_{act}^{(Ni)}}{kT} \right]$ (see eq (17), section 4.2.7)

$$n_{ads} = n_{eq} \exp \left[\frac{2\sigma a^3}{kTr^*} \right] \quad (\text{see section 4.3.1})$$

and:

$$n_{eq} = \frac{1}{a^2} \exp \left[\frac{h_{bulk} - h_{ads}^{(Ni)}}{kT} \right] \quad (\text{from eq. (9) and (3), section 4.2})$$

The free energy of formation of a nucleus with radius ρ_N from adatoms with a concentration corresponding to r^* , is given by:

$$\Delta G = \pi \rho_N^2 a 2\sigma \left(\frac{1}{r^*} - \frac{1}{r} \right) + 2\pi \rho_N \epsilon$$

where $2\sigma \left(\frac{1}{r^*} - \frac{1}{r} \right)$ is the free energy difference per unit of volume between particles with radius r^* and r and ϵ is the free energy per unit length of edge of a two-dimensional nucleus.

The radius of the critical nucleus and the activation energy for its formation are derived from:

$$\frac{d\Delta G}{d\rho} = 0$$

The result is:

$$\Delta G_{cr} = \frac{\pi \epsilon^2}{2a\sigma} \frac{r r^*}{r - r^*} \quad \text{for } \rho_{cr} = \frac{\epsilon}{2\sigma a} \cdot \frac{r r^*}{r - r^*}$$

Combining all quantities gives the desired result:

$$\begin{aligned} \frac{dr}{dt} &= \frac{\pi^2}{\ln \ell} Z \frac{r^2}{a} \frac{kT}{h} \exp \left[\frac{2\sigma a^3}{kTr^*} \right] * \\ &* \exp \left[\frac{h_{bulk} - h_{ads} (Ni) - u_{act} (Ni)}{kT} \right] \exp \left[- \frac{\pi \epsilon^2}{2a\sigma kT} \frac{r r^*}{r - r^*} \right] \quad (19) \end{aligned}$$

Using the data from table 4.3, with $h_{bulk} = -6.0 \cdot 10^{-19} \text{J}$, and the approximation $Z = 1$, the following rates are obtained:

at 873 K:

$$\begin{aligned} \frac{dr}{dt} &= 3.5 \cdot 10^5 r^2 \exp \left(\frac{4.75}{r^*} \right) \exp \left(\frac{0.667 h_{bulk}}{kT} \right) \exp \left(- 28.4 \frac{r r^*}{r - r^*} \right) \text{ms}^{-1} \\ &= 4.7 \cdot 10^3 r^2 \exp \left[\frac{4.75}{r^*} \right] \exp \left[- 28.4 \frac{r r^*}{r - r^*} \right] \text{nm h}^{-1} \quad (20) \end{aligned}$$

and at 973 K:

$$\frac{dr}{dt} = 1.6 \cdot 10^5 r^2 \exp \left[\frac{4.18}{r^*} \right] \exp \left[- 24.4 \frac{r r^*}{r - r^*} \right] \text{ nm h}^{-1} \quad (21)$$

where r and r^* are expressed in nm.

The effect of the second exponential factor in equations (20) and (21) is still difficult to judge, as $\frac{r r^*}{r - r^*}$ is a complicated quantity. Its possible values can be limited, however, by considering the conditions where nucleation limitation can operate in the sense as considered here.

No limitation at all will be expected when the two-dimensional nuclei are so small, that they only contain a few nickel atoms. This means, that for nucleation limitation to be effective:

$$\rho_{cr} > a \quad (22)$$

or:

$$\frac{\varepsilon}{2a\sigma} \frac{r r^*}{r - r^*} > a$$

This means that

$$\frac{r r^*}{r - r^*} > \frac{2\sigma a^2}{\varepsilon}$$

Using the values for σ , ε and a as given in table 4.3:

$$\frac{r r^*}{r - r^*} > 0.7 \text{ nm} \quad (23)$$

On the other hand, extreme limitation of growth due to the need for nucleation, i.e. no growth at all, is to be expected when the radius of the critical nucleus exceeds the radius of the crystal face on which it should be formed:

$$\rho_{cr} > \alpha \cdot r \quad (24)$$

where α is a geometric factor, which we assume to be 0.5.

Then:

$$\frac{\epsilon}{2\sigma a} \frac{r}{r-r^*} > 0.5 r \text{ and } \frac{r}{r-r^*} > \frac{\sigma a}{\epsilon} r = 1.63 r \quad (25)$$

In conclusion, equations (20) and (21) apply to the situations where:

$$0.7 < \frac{r}{r-r^*} < 1.63 r \quad (26)$$

Introduction of eq. (23) in the growth rate expression at 873 K, eq (20), results in:

$$\frac{dr}{dt} < 1.1 \cdot 10^{-5} r^2 \exp \left[\frac{4.75}{r^*} \right] \text{ nm h}^{-1} \quad (27)$$

We can now compare this with the rate obtained by considering step 2 as rate determining. For a good comparison the result from table 4.5 has to be combined with eq (18):

$$\begin{aligned} \frac{dr}{dt} &= 4.75 \exp \left[\frac{4.75}{r^*} \right] \left(\frac{1}{r^*} - \frac{1}{r} \right) \frac{1.8 \cdot 10^{-5}}{r^2} \\ &= \frac{1.2 \cdot 10^{-4}}{r^2} \exp \left[\frac{4.75}{r^*} \right] \end{aligned} \quad (28)$$

It is seen that at particle sizes around 1 nm, nucleation may be an effective rate determining step if such particles have surfaces consisting of low index crystal faces.

At increasing $\frac{r}{r-r^*}$ during sintering, the effect of the second exponential factor in eq (20) increases and sintering will come rapidly to a stand still. In order to come to a more precise comparison of the consequence of eq (20) and (28), sintering of a dispersion of particles will have to be considered in detail. This will be done in the next chapter.

For the sake of completeness, the equivalents of equations (20) and (21) will also be given for the parameters corresponding to (100)-faces:

$$\text{at 873K: } \frac{dr}{dt} = 4.7 \cdot 10^3 \exp \left[\frac{6.59}{r^*} \right] \exp \left[-2.76 \frac{r}{r-r^*} \right] \text{ nm h}^{-1} \quad (29)$$

$$\text{at } 973\text{K: } \frac{dr}{dt} = 1.6 \cdot 10^5 \exp \left[\frac{5.83}{r^*} \right] \exp \left[-2.10 \frac{rr^*}{r-r^*} \right] \text{ nm h}^{-1} \quad (30)$$

In analogy to eq (26) a range can be defined, where growth limitation due to nucleation may be operative:

$$2.7 < \frac{rr^*}{r-r^*} < 6.2 \text{ r.}$$

4.7. The overall reliability of the results obtained

In the appendix a discussion is given of a number of factors that might affect the accuracy of the results derived thus far. The main conclusions may be summarized as follows:

- Mobility of the adsorbed nickel atoms would influence the rate of the various adsorption and desorption steps considerably. These effects would be taken into account by assuming, that the transition states for adsorption and desorption, both for nickel and alumina, would be completely mobile. Anyhow, these are sensible assumptions, but they would lead to much higher rates of adsorption and desorption.
- Taking into account the vibrational entropy in the calculation of the thermodynamic potential of bulk nickel, would lead to a considerable reduction of the vapour pressure of nickel and of the equilibrium concentrations of adsorbed nickel. The rates of adsorption and desorption steps as well as of all diffusion steps would be influenced. For the former this would compensate the effects of the mobility of the transition states for adsorption and desorption. The effect on the latter would take away the serious problem, that diffusion of nickel vapour away from the sample did appear so rapid that depletion of the sample by this process would be expected to occur simultaneously with sintering of the nickel particles.
- Refinement of other entropy terms by vibrational contributions would not lead to great changes in the relative rates of the various reaction steps. After the corrections, discussed so far, all conclusions as to the rate determining step would remain valid.

In the appendix a discussion is also given of the choice made for the enthalpy of evaporation of nickel from the bulk: $-h_{\text{bulk}} = 6.0 \cdot 10^{-19} \text{J}$ at $^{-1}$. It turns out, that this value must be considered as a minimum value. Higher values would lead to correspondingly lower rates of all reaction steps.

The most important set of approximations, not dealt with in the appendix, are those formulated in table 4.3, where all heats of adsorption, activation energies for diffusion over surfaces and surface energies are expressed as fractions of h_{bulk} . The possible effect of these estimates on the relative rates of the various reactions are seen most clearly in the last column of table 4.4, presenting the factors of h_{bulk}/kT in the exponent of the Arrhenius factors of the various rates. As steps 1, 7 and 8 could be discarded with wide margins, it is seen that only the relative rate of step 2 as compared to step 3 and 6 would be influenced by the estimates of table 4.3. It is not to be expected that the general picture of the relative rates of the various steps would be seriously influenced by the different estimates.

A very real sensitivity to the estimates of table 4.3, however, turns up in the rate formulas for nucleation inhibited incorporation of nickel atoms in growing particles. As is seen from eq (19), in the last exponential a factor $\epsilon^2/a\sigma$ occurs. The values of this factor strongly depend on the estimates used for ϵ and σ . A comparison of eq (20) and (21) on the one hand and of eq (29) and (30) on the other hand shows the very large difference in the exponents, resulting from the estimates for a (111)-face and a (100)-face, respectively.

To avoid misunderstanding a final comment should be made. The Eyring method for determining absolute rates of reaction should never be seen as a method for calculating very accurate values of reaction rates. But in a field, where no other method is available, a calculation of frequency factors within one or two orders of magnitude is an important achievement. This holds the more so, because the effects of inaccuracies in the estimates of activation energies also easily will be one or two orders of magnitude. Our general contention is, that relative errors will be much less than absolute errors, in the same way

that differences in the estimate for h_{bulk} lead to greater absolute than relative errors.

It is in this context that choices have to be made as to the rate equations to be used for the discussion in the next chapter of the development in time of the sintering in ensembles of small particles. In view of the uncertainties involved, our main aim is to use some representative data for the various processes. As such we may consider the following:

1. The data of step 2 for the (111)-face in table 4.5 as representative for both route I and route II, that is, transport of nickel atoms by surface and gas phase diffusion over the alumina surface.
2. The data of step 6 for the (111)-face in table 4.5 as representative for the evaporation of nickel atoms from the surface of the nickel particles followed by diffusion through the gas phase from one particle to another.
3. The data of eq (20) and (21) as representative for the growth of nickel particles by nucleation on a (111)-face.
4. The data of eq (29) and (30) for the same on a (100)-face.

4.8. References

- [1] K.J. Laidler; J.H. Meiser, Physical Chemistry, Benjamin/Cummings, 1982, Ch. 9.
- [2] S. Glasstone; K.J. Laidler; H. Eyring, Theory of Rate Processes, McGraw-Hill Inc., 1941.
- [3] A.K. Vyh: Oxides and Oxidic Films, Vol. 6, 1982.
- [4] B. Lewis; J.C. Anderson, Nucleation and growth of thin films, Academic Press, 1978.
- [5] H. Jones; R.G.N. Leak: Met. Sci. J. 1 (1967) 211.
H. Jones; R.G.N. Leak: Met. Sci. J. 5 (1971) 15.
- [6] A.R. Miedema: Nederlands Tijdschrift voor Natuurkunde A46 (1980) 47.
- [7] A.N. Nesmeyanov: Vapor pressure of the chemical elements, 1963.
- [8] B.K. Chakraverty: J. Phys. Chem. Solids 28 (1967) 2401.
- [9] P. Wynblatt; N.A. Gjostein: Acta Metall. 24 (1976) 1165.

5. KINETICS OF THE COARSENING OF A PARTICLE ENSEMBLE BY SINGLE ATOM EMISSION AND CAPTURE

5.1. Introduction

The phenomenon of Ostwald ripening, the gradual increase in average particle size in a dispersion of small particles under the influence of differences in surface energy, is well known as a mechanism for sintering during a long time. The mathematical formulation for this phenomenon, as used presently, has been due to I.M. Lifshitz and V.V. Slyozov [1] and C. Wagner [2] and is generally referred to as the L.S.W. theory. This L.S.W. theory has been developed originally for a dispersion of colloidal particles in a solution. The application to the two-dimensional problem of a dispersion of metal particles at the surface of a solid carrier is due to B.K. Chakraverty [3] and among others T.M. Ahn and J.K. Tien [4]. Our discussion will be based on the papers of Chakraverty, Ahn and Tien, although in some details modified points of view will be introduced.

The general way to classify a growing dispersion of particles is by its distribution function $f(r,t)$, such that $f(r,t)dr$ given at time t_1 represents the number of particles in the system, or per unit of volume, with radii between r and $r + dr$. The development of the distribution function is governed by the so-called continuity equation:

$$\frac{\partial f(r,t)}{\partial t} + \frac{\partial}{\partial r} \left\{ f(r,t) \frac{dr}{dt} \right\} = 0$$

expressing the fact that the change, $\partial f(r,t)/\partial t$, of the number of particles with sizes between r and $r + dr$ is equal to the difference of number of particles entering by growth at r and disappearing by growth at $r + dr$.

The continuity equation can be transformed into a partial differential equation when an expression for dr/dt is available, either in r and t , or as has been encountered in the previous chapter, in r .

Generally the experimental situation is such that the total mass of the material in the particle ensemble is conserved. Solutions of the continuity equation have to be sought such that:

$$\int_0^{\infty} \frac{2}{3} \pi r^3 f(r,t) dr = V = \text{constant} \quad (1)$$

where V is the total volume of the particles. The numerical factor $2\pi/3$ represents our contention, that the supported particles can be considered as half spheres.

Here the contribution to the total mass of the material atomically dispersed in the solution, the vapour phase or the adsorbed state is neglected.

As sintering of the supported particles occurs by transport through the vapour phase or the adsorbed state, these states in itself are important for the processes. In fact it has already been suggested in the previous chapter, that the sintering is governed by an average vapour pressure and a corresponding concentration of adatoms in the space between the particles. These average concentrations can be specified by a virtual diameter r^* of the particles, that would be in equilibrium with these average concentrations. Particles with $r > r^*$ grow, particles with $r < r^*$ shrink, while particles with $r \ll r^*$ disappear very fast. Ultimately the growth rates, dr/dt , derived in the previous chapter, can be expressed as functions of r and r^* , see section 4.5.

During the sintering process r^* increases gradually with the growth of the average particle size. Formally, r^* is a function of t , and thus introduces a time dependence of dr/dt , to be introduced in the continuity equation. In order to circumvent part of the mathematical difficulties the indirect time dependence of dr/dt might cause, earlier investigators have used a change to more appropriate variables, namely *dimensionless radius and time variables defined as:*

$$\rho = \frac{r(t)}{r^*(t)} \quad (2)$$

and

$$\tau = \ln \left[\frac{r^*(t)}{r^*(0)} \right] \quad (3)$$

where $r^*(0)$ is the value of r^* at $t=0$.

Accordingly a new distribution function is defined, that is $\phi(\rho, \tau)$, such that $\phi(\rho, \tau)$ gives the number of particles with a radius between ρ and $\rho + d\rho$ at time τ . The corresponding continuity equation in the ρ, τ space then reads:

$$\frac{\partial \phi(\rho, \tau)}{\partial \tau} + \frac{\partial}{\partial \rho} \left[\phi(\rho, \tau) \frac{d\rho}{d\tau} \right] = 0 \quad (4)$$

The only transformation yet to make, is from dr/dt to $d\rho/d\tau$. This is performed as follows:

$$\frac{d\rho}{d\tau} = \frac{d}{d \ln(r^*/r_0)} \frac{r}{r^*} = r^* \frac{d(r/r^*)}{dr^*} = - \frac{r}{r^*} + \frac{dr}{dr^*} = - \rho + \frac{1}{dr^*/dt} \frac{dr}{dt} \quad (5)$$

As growth formulas are available expressing dr/dt in r and r^* , dr/dt may also be easily expressed in ρ and r^* . In this way the only time dependence remaining is that of the slowly developing functions r^* and dr^*/dt . Presently it will be shown in a way slightly different from that of earlier authors, how the problem of this time dependence is circumvented. For convenience, we follow other authors by writing:

$$\frac{d\rho}{d\tau} (\rho, \tau, r^*, \frac{dr^*}{dt}) = -g (\rho, \tau, r^*, \frac{dr^*}{dt}) \quad (6)$$

The continuity equation can then be given as:

$$\frac{\partial \phi(\rho, \tau)}{\partial \tau} = \frac{\partial}{\partial \rho} \left\{ \phi(\rho, \tau) g(\rho, \tau, r^*, \frac{dr^*}{dt}) \right\} \quad (7)$$

Now, the feasibility is investigated of solutions of the type:

$$\phi(\rho, \tau) = T(\tau) \psi(\rho) \quad (8)$$

Reading equation (7) as:

$$\frac{\partial \phi}{\partial \tau} = g \frac{\partial \phi}{\partial \rho} + \psi \frac{\partial g}{\partial \rho}$$

and substituting equation (8) leads to:

$$\psi \frac{dT}{d\tau} = g T \frac{d\psi}{d\rho} + \psi T \frac{\partial g}{\partial \rho}$$

Attempting a separation of variables by dividing this equation by ψT :

$$\frac{1}{T} \frac{dT}{d\tau} = g \frac{d \ln \psi}{d\rho} + \frac{\partial g}{\partial \rho} \quad (9)$$

A successful separation of variables requires, that $\partial g / \partial \rho$ and hence g is independent of τ and only dependent on ρ . As now the left hand side only depends on τ and the right hand side only on ρ , the equality requires that both sides must be equal to a constant K , independent of ρ and τ . Now further solution is a straightforward affair.

First the time dependent part:

$$\frac{1}{T} \frac{dT}{d\tau} = K \quad (10)$$

with solution: $T(\tau) = K_0 \exp [K\tau]$ (11)

The constant K follows from the conservation of volume, eq. (1):

$$\frac{2\pi}{3} \int_0^\infty r^3 \phi(\rho, \tau) d\rho = V$$

$$\frac{2\pi}{3} \int_0^\infty \rho^3 r^{*3} T(\tau) \psi(\rho) d\rho = V$$

Substituting r^* according to eq (3) and $T(\tau)$ according to eq (11) results in:

$$\frac{2\pi}{3} r^{*3}(0) K_0 \exp [3\tau] \exp [K\tau] \int_0^\infty \rho^3 \psi(\rho) d\rho = V$$

As V , the total volume of the particles, is independent of τ :

$$K = -3$$

Then the ρ -dependent part:

$$g \frac{d \ln \psi}{d\rho} + \frac{dg}{d\rho} = -3$$

$$\frac{d \ln \psi}{d\rho} + \frac{1}{g} \frac{dg}{d\rho} = -\frac{3}{g}$$

$$\text{and: } \ln \psi g = -3 \int_0^\rho \frac{1}{g} d\rho \quad (12)$$

Integration leads to $\psi(\rho)$. As indicated by earlier authors [1-3], expression of this particle size distribution in ρ instead of r allows of obtaining a time independent particle size distribution. The growth of the particles is reflected by a growth of the average particle size as represented by the time dependence of ρ via the time dependence of r^* .

Finally, the circumstance that g , and hence $d\rho/d\tau$, only depend on ρ , involves that g must be independent of r^* and dr^*/dt . It will turn out that this requirement leads to a relation between dr^*/dt and r^* which is just the required relation expressing growth of an average particle size r^* with time.

The examples to be studied will be the most relevant growth processes coming from the discussion in the previous chapter:

- particle growth limited by the diffusion of nickel atoms over the alumina surface (step 2);
- particle growth limited by desorption of nickel atoms directly from the surface of the particles (step 6);
- particle growth limited by two-dimensional nucleation on the growing particle faces.

However, before turning to these examples, two remarks may be made:

- The average radius r^* can be thought as to have been obtained by averaging over the vapour pressures. Therefore it will be different from the average according to the definition:

$$\bar{r}(t) = \int_0^{\infty} r(t) f(r,t) dr \quad (13)$$

For all reasonable purposes, however, $r^*(t)$ will be just as informative as $\bar{r}(t)$. If required, for instance, for comparison with the experiments, $r^*(t)$ could be transformed into $\bar{r}(t)$ when $f(r,t)$ is known. In view of the accuracy of the experiments such a transformation will be rarely justified.

- The solutions obtained, explicitly refer to the circumstance, that separation of variables is possible, and the particle size distribution, expressed in ρ , is invariant in time. The initial particle size distribution is not necessarily equal to the steady state distribution. Therefore there must be initial stages of sintering where the separation of variables is not justified. There is even no guarantee that the system will tend towards a steady state solution or that a steady state solution is possible for all situations. In the wake of earlier investigators, however, we assume that, if a steady state solution is mathematically feasible, it will be the experimentally relevant solution attained after a relatively short initial stage of sintering.

5.2. Sintering limited by diffusion of nickel atoms over the alumina surface

The relevant expression for the growth of a particle with radius r is obtained by combining the formula for step 2 in table 4.2 with equation (4.18).

$$\frac{dr}{dt} = \frac{1}{4} \frac{a^3}{r^2 \ln \xi} \frac{2\sigma a^3}{kTr^*} \frac{kT}{h} \exp \left[\frac{2\sigma a^3}{kTr^*} \right] \left(1 - \frac{r^*}{r} \right) *$$

$$* \exp \left[\frac{h_{\text{bulk}} - h_{\text{ads}}(\text{Al}_2\text{O}_3) - u_{\text{act}}(\text{Al}_2\text{O}_3)}{kT} \right]$$

$$= \frac{A_1}{r^3} \exp \left[\frac{2\sigma a^3}{kTr^*} \right] \left(\frac{r}{r^*} - 1 \right) \quad (14)$$

$$\text{where } A_1 = \frac{1}{2 \ln \ell} \frac{\sigma a^6}{h} \exp \left[\frac{h_{\text{bulk}} - h_{\text{ads}} (Al_2O_3) - u_{\text{act}} (Al_2O_3)}{kT} \right] \quad (15)$$

According to (5), transformation to the ρ - τ space gives:

$$\frac{d\rho}{d\tau} = -\rho - \frac{1}{dr^*/dt} \frac{A_1}{r^{*3}} \exp \left[\frac{2\sigma a^3}{kTr^*} \right] \frac{1-\rho}{\rho^3} = -\rho - \lambda \frac{(1-\rho)}{\rho^3} \quad (16)$$

$$\text{with } \lambda = \frac{A_1}{r^{*3} dr^*/dt} \exp \left[\frac{2\sigma a^3}{kTr^*} \right] \quad (17)$$

The requirement, derived earlier, that $g(\rho, \tau, r^*, dr^*/dt)$, and hence $d\rho/d\tau$, must be a function of ρ only, leads to the conclusion that λ has to be a constant independent of time. This immediately leads to a rate equation for the sintering process:

$$\frac{dr^*}{dt} = \frac{A_1}{\lambda} \cdot (r^*)^{-3} \exp \left[\frac{2\sigma a^3}{kTr^*} \right] \quad (18)$$

where only the constant λ has to be chosen. This choice is limited by the requirements $d\rho/d\tau$ has to meet. In the first place only negative values of $d\rho/d\tau$ are meaningful. That is so because $\rho = r/r^*$, and at constant r only increasing r^* is to be expected. In the second place, at the upper limit of r (thus of ρ at constant r^*) there is no mechanism by which particles could be created or removed, hence $d\rho/d\tau$ should be zero.

Considering expression (16):

$$\frac{d\rho}{d\tau} = -\frac{\rho^4 - \lambda\rho + \lambda}{\rho^3},$$

several types of behaviour are possible, dependent on the value of λ , as can be seen in fig. 5.1.

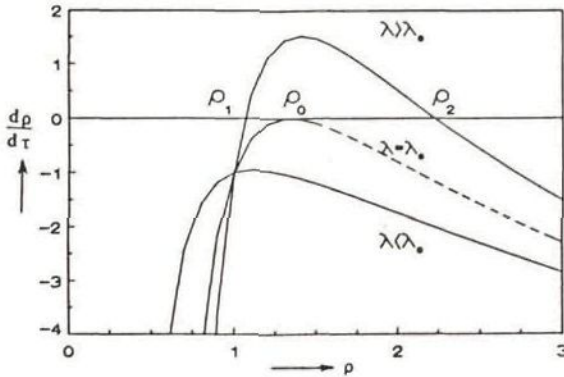


Fig. 5.1. Dimensionless growth rate for different values of λ

At $\rho \rightarrow 0$, $d\rho/d\tau \rightarrow -\infty$, expressing the fact that very small particles disappear extremely rapidly. For $\lambda = \lambda_0$, the curve for $d\rho/d\tau$ touches the ρ -axis. The conditions for this to occur are:

$$\frac{d\rho}{d\tau} = 0$$

and $\frac{d}{d\rho} \left(\frac{d\rho}{d\tau} \right) = 0$

It is easy to see that $\lambda_0 = 256/27$, while $\rho_0 = 4/3$. For $\lambda < \lambda_0$, the curve does not intercept the ρ -axis. Such values for λ are unacceptable. For $\lambda > \lambda_0$ there is an intercept at lower ρ -values according to higher λ -values.

For $\lambda > \lambda_0$ the part of the curve for $\rho > \rho_1$ (the intercept) is unacceptable as $d\rho/d\tau$ becomes positive. Also for $\lambda = \lambda_0$, the dotted part of the curve is rejected as $d\rho/d\tau$ increases indefinitely and cannot attain zero anymore.

In conclusion only $\lambda > 256/27$ is feasible, coupled to the segment of the $d\rho/d\tau$ -curve for ρ between zero and the first intercept. Following Chakraverty we make the most attractive choice of $\lambda = 256/27$.

Introduction in eq (18) results in the rate of sintering:

$$\frac{dr^*}{dt} = \frac{27A_1}{256} (r^*)^{-3} \exp \left[\frac{2\sigma a^3}{kTr^*} \right] \quad (20)$$

The foregoing argument closely followed Chakraverty. Yet the resulting equation (20) differs from his result in that the exponential factor is added here. This is a consequence of the development used in section 4.5, which is superior to the approximations made by Chakraverty. As soon as $2\sigma a^3/kTr^*$ becomes of the magnitude of unity the exponential term makes itself felt, and the sintering process does not anymore follow a simple power law as frequently assumed in the past. Equation (20) will be used later in this chapter, in combination with the results of two alternative processes, for the analysis of our experimental data.

For the sake of completeness, here, first the results of section 5.1 will be used to derive the steady state particle size distribution. The appropriate formula to be used is eq (12), which in combination with eq (16) leads to:

$$\begin{aligned} \ln \psi g &= -3 \int_0^\rho \frac{\rho^3 d\rho}{\rho^4 - \frac{256}{27} \rho + \frac{256}{27}} \\ &= -3 \int_0^\rho \frac{\rho^3 d\rho}{(4/3 - \rho)^2 (16/3 + 8\rho/3 + \rho^2)} \end{aligned} \quad (21)$$

Integration then results in:

$$\begin{aligned} \ln \psi g &= \frac{2}{4-3\rho} - \frac{7}{6} \ln \left(\frac{4}{3} - \rho \right) - \frac{1}{6\sqrt{2}} \operatorname{arctg} \left\{ \frac{1+3\rho/4}{\sqrt{2}} \right\} + \\ &\quad - \frac{11}{2} \ln \left\{ \frac{16}{3} + \frac{8}{3} \rho + \rho^2 \right\} + \text{constant} \end{aligned}$$

$$\text{where: constant} = \frac{7}{6} \ln \frac{4}{3} + \frac{11}{12} \ln \frac{16}{3} + \frac{1}{2} + \frac{\operatorname{arctg} 1/\sqrt{2}}{6\sqrt{2}}$$

$$= \ln 11.5$$

Substitution of $g = d\rho/d\tau$ leads to the result also obtained by Chakraverty:

$$\psi(\rho) = 11.5 \rho^3 \frac{\exp \left[-\frac{2}{4-3\rho} \right] \exp \left[-\frac{1}{6\sqrt{2}} \operatorname{arctg} \frac{1+(3\rho/4)}{\sqrt{2}} \right]}{\left(\frac{4}{3} - \rho \right)^{19/6} \left(\frac{16}{3} + \frac{8}{3} \rho + \rho^2 \right)^{23/12}} \quad (22)$$

This distribution function is given in fig. 5.2.

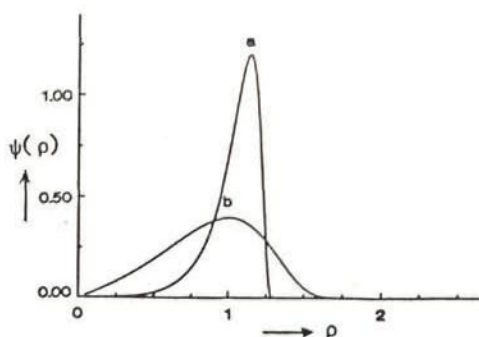


Fig. 5.2. The dimensionless particle size distribution for mechanisms 2 (curve a) and 6 (curve b).

5.3. Sintering limited by desorption from the nickel particles

The relevant expression for the growth of a particle of radius r is obtained by combining the formula of step 6 of table 4.2, with equation (4.18).

$$\begin{aligned} \frac{dr}{dt} &= a \frac{2\sigma a^3}{kTr^*} \frac{kT}{h} \exp\left[\frac{2\sigma a^3}{kTr^*}\right] \left(1 - \frac{r^*}{r}\right) \exp\left[-\frac{h_{\text{bulk}}}{kT}\right] \\ &= \frac{A_2}{r} \exp\left[\frac{2\sigma a^3}{kTr^*}\right] \left(\frac{r}{r^*} - 1\right) \end{aligned} \quad (23)$$

with $A_2 = \frac{2\sigma a^4}{h} \exp\left[-\frac{h_{\text{bulk}}}{kT}\right]$

According to eq (5), transformation to the dimensionless ρ, τ -space gives:

$$\frac{d\rho}{d\tau} = -\rho - \lambda_2 \frac{1-\rho}{\rho} \quad (24)$$

$$\text{with } \lambda_2 = \frac{A_2}{r^* dr^*/dt} \exp\left[\frac{2\sigma a^3}{kTr^*}\right] \quad (25)$$

Similar arguments as used in the preceding section 5.2 lead to the following results:

$$\frac{dr^*}{dt} = \frac{A_2}{\lambda_2} r^{*-1} \exp \left[\frac{2\sigma a^3}{kTr^*} \right] \quad (26)$$

Judging from the curve of $dp/d\tau$ vs. ρ , equation (24), only satisfactory solutions are obtained for $\lambda_2 > 4$. Again we make the choice of $\lambda_2 = 4$, which is the case where the curve touches the ρ -axis (analogous to fig. 5.1). The corresponding range of ρ is from 0 to 2.

As before, the distribution function is derived from:

$$\ln \psi_\rho = -3 \int_0^\rho \frac{\rho d\rho}{\rho^2 - 4\rho + 4} \quad (27)$$

which results after integration in:

$$\ln \psi_\rho = -3 \left\{ \ln(2-\rho) + \frac{2}{2-\rho} - \ln 2 - 1 \right\}$$

and subsequently in:

$$\psi(\rho) = 8 e^{3\rho} (2-\rho)^{-5} \exp \left[-\frac{6}{2-\rho} \right] \quad (28)$$

This curve is also represented in fig. 5.2.

Again these results will be further used in a comparison with other mechanisms in section 5.5.

5.4. Sintering limited by two-dimensional nucleation on the growing particle faces

Now the essential rate equation for the growth of a single particle is given by eq (4.19):

$$\begin{aligned} \frac{dr}{dt} &= \frac{\pi^2}{\ln 2} Z \frac{r^2}{a} \frac{kT}{h} \exp \left[\frac{2\sigma a^3}{kTr^*} \right] \exp \left[\frac{-\pi \epsilon^2}{2\sigma a kT} \frac{r}{r-r^*} \right] * \\ &* \exp \left[\frac{h_{\text{bulk}} - h_{\text{ads}}(\text{Ni}) - u_{\text{act}}(\text{Ni})}{kT} \right] \\ &= A_3 r^2 \exp \left[\frac{2\sigma a^3}{kTr^*} \right] \exp \left[-\frac{\pi \epsilon^2}{2\sigma a kT} \frac{r}{r-r^*} \right] \end{aligned} \quad (29)$$

$$\text{with } A_3 = \frac{\pi^2 Z}{a \ln \lambda} \frac{kT}{h} \exp \left[\frac{h_{\text{bulk}} - h_{\text{ads}}(\text{Ni}) - u_{\text{act}}(\text{Ni})}{kT} \right]$$

Transformation, according to eq. (5), to the ρ, τ -space results in the dimensionless growth rate:

$$\frac{d\rho}{d\tau} = -\rho + \frac{\rho^2}{dr^*/dt} A_3 (r^*)^2 \exp \left[\frac{2\sigma a^3}{kTr^*} \right] \exp \left[\frac{-\pi \epsilon^2 r^*}{2\sigma a kT} \frac{\rho}{\rho-1} \right] \quad (30)$$

The requirement that $d\rho/d\tau$ should be a function of ρ only, can be satisfied with the following construction:

$$\frac{d\rho}{d\tau} = -\rho + \lambda_3 \rho^2 \quad (31)$$

$$\text{and } \frac{dr^*}{dt} = \frac{A_3}{\lambda_3} (r^*)^2 \exp \left[\frac{2\sigma a^3}{kTr^*} \right] \exp \left[\frac{-\pi \epsilon^2 \rho}{2\sigma a kT (\rho-1)} r^* \right] \quad (32)$$

where λ_3 is a constant.

Now complications arise that did not occur in the preceding sections. There the equations derived for $d\rho/d\tau$ were valid over the whole range of ρ considered. The factor $\rho-1$ took account of the fact that particles grow for $\rho > 1$ and shrink as $\rho < 1$. In contrast, equation (29) and hence eq (31), only applies to growing particles, that is for $\rho > 1$. As we have shown earlier, section 4.6, there is even a range of supersaturations, $\rho-1$, where nucleation is impossible and therefore growth does not occur. The minimum supersaturation required for growth to occur is given by eq (4.25) as:

$$\rho_B^{-1} = \left(\frac{r - r^*}{r^*} \right)_B = \frac{\epsilon}{\sigma a} \quad (33)$$

Altogether one should distinguish three ranges:

- $\rho > \rho_B$ growth covered by eq (32)
- $1 < \rho < \rho_B$ no change of particle size, $dr/dt = 0$
- $0 < \rho < 1$ particles shrink according to one of the mechanisms mentioned before.

However, the growth processes in the three ranges considered have one feature in common: the development of r^* and dr^*/dt is governed by

nucleation limitation. This means that dr^*/dt , as derived from eq (32), also applies to the shrinking process for $\rho < 1$.

The most important result thus far is the rate of growth of the average particle size, dr^*/dt , as given by eq. (32). However, λ_3 is still a constant to be determined. In addition, now dr^*/dt depends on ρ , because of the factor $\rho/(\rho-1)$ in the second exponential. As seen before, the maximum admissible value for ρ depends on λ and is obtained by the condition:

$$\left(\frac{d\rho}{d\tau}\right)_{\rho=\rho_0} = 0$$

Substituting eq (31), this results in:

$$\rho_0 = \frac{1}{\lambda_3} \quad (34)$$

The second criterion used earlier to make a choice for λ_3 , viz:

$$\left\{\frac{d}{d\rho} \left(\frac{d\rho}{d\tau}\right)\right\}_{\rho=\rho_0} = 0$$

does not apply anymore. This situation has been recognized by T.M. Ahn and coworkers [4]. Instead they advocate the use of a criterion, applied by C. Wagner [2]:

$$\frac{\partial}{\partial \tau} \int_0^{\rho_0} \phi(\rho, \tau) d\rho = \lim_{\rho \rightarrow 0} \left\{ \phi(\rho, \tau) \frac{d\rho}{d\tau} \right\} \quad (35)$$

Here two expressions are used, describing the rate of decrease in the number of particles: the change in the total number and the rate of disappearance at $\rho = 0$. The essential assumption is, that no particles appear or disappear at $\rho = \rho_0$.

A very elegant formulation for eq (35) can be found by substituting eq (6), (8) and (11), and assuming the value $K = -3$ derived earlier. The result is:

$$\int_0^{\rho} \psi(\rho) d\rho = \frac{1}{3} \lim_{\rho \rightarrow 0} [\psi(\rho)g(\rho)]$$

Provided $[g(\rho=0)]^{-1}$ is finite, eq (12) shows that:

$$\lim_{\rho \rightarrow 0} \ln[\psi(\rho)g(\rho)] = 0$$

$$\text{and hence } \int_0^{\rho} \psi(\rho) d\rho = \frac{1}{3} \quad (36)$$

A problem with the application of eq (35) or (36), however, is that these equations are direct consequences of the continuity equation (4). They will therefore be valid for all solutions of the continuity equation derived using eq (31), independent of the value of λ_3 .

There is no choice but to take an arbitrary value for λ_3 , where in view of eq (34) the maximum must be:

$$\lambda_3 = \frac{1}{\rho_B}$$

as ρ_0 must be larger than ρ_B .

A reasonable assumption might be:

$$\rho_0 - 1 = 2(\rho_B - 1) ; \lambda_3 = \frac{1}{2\rho_B - 1}$$

Then it is also possible to make an estimate of the factor $\rho/(\rho-1)$ in the second exponential of eq (32). Its value varies between:

$$\frac{\rho_B}{\rho_B - 1} \text{ and } \frac{\rho_B - 1/2}{\rho_B - 1}$$

Introduction of eq (33) and of the average value of $\rho/(\rho-1)$ into eq (32) leads to a final expression for the rate of growth under nucleation limitation:

$$\frac{dr^*}{dt} = A_3 \left(1 + \frac{2\varepsilon}{\sigma a}\right) (r^*)^2 \exp\left[\frac{2\sigma a^3}{kTr^*}\right] \exp\left[-\frac{\pi\varepsilon}{2kT} \left(\frac{\varepsilon}{\sigma a} + \frac{3}{4}\right)r^*\right] \quad (37)$$

Again for the sake of completeness the distribution function for the situation of nucleation limitation will be derived. Assuming that the

rate of shrinkage of the particles for $\rho < 1$ is determined by diffusion of nickel atoms over the alumina surface, the considerations of section 2 apply, and in principle eq (16) and (18) can be used. There is a problem, however, as dr^*/dt is limited by nucleation inhibition and given in eq (37). This upsets the whole argument of section 1 and 2, for now it is impossible to make λ of eq (17) independent of r^* and hence of τ . Separation of variables, as proposed in eq (8) is no longer feasible.

It will also be clear, however, that for the range where nucleation inhibition is really important, dr^*/dt is so small, that it can be easily followed by the shrinking and disappearance of the particles with $\rho < 1$. In the extreme case $d\rho/d\tau$ will have high (negative) values for all ρ values from 0 up to 1 and correspondingly $\psi(\rho)$ will have very low values up to close to $\rho = 1$. Under these circumstances the dependence of $d\rho/d\tau$ on τ will not have a great effect anymore.

Moving to the range $1 < \rho < \rho_B$, we have seen already that $dr/dt = 0$. From eq (5), the transformation to the ρ, τ -space leads to:

$$\frac{d\rho}{d\tau} = -\rho \quad \text{and} \quad g(\rho) = \rho$$

Introduction into eq (12), leads to:

$$\begin{aligned} \ln \psi g &= -3 \int_0^1 \frac{d\rho}{\rho} - 3 \int_1^{\rho} \frac{d\rho}{\rho} \\ &= -C_1 - 3 \ln \rho \end{aligned}$$

or:

$$\psi = \rho^{-4} \exp [-C_1] \quad (38)$$

Analogously for the region $\rho_B < \rho < \rho_0$, we find by substitution of $d\rho/d\tau$ of eq (31) into equation (12):

$$\ln \psi (\rho - \lambda_3 \rho^2) = -3 \int_0^{\rho_B} \frac{d\rho}{\rho} - 3 \int_{\rho_B}^{\rho_0} \frac{d\rho}{\rho(1-\lambda_3\rho)}$$

and:

$$\psi = \frac{(1-\lambda_3\rho)^2 \exp [-C_1]}{\rho^4 (1-\lambda_3\rho_B)^3} \quad (39)$$

If desired, the factor $\exp [-C_1]$ can be determined from the Wagner criterion (36), where the contribution for $\rho < 1$ to the integral is neglected. In agreement with the assumption $\left| \frac{d\rho}{d\tau} \right| \gg 1$ for $0 < \rho < 1$, it is found that $C_1 = 0$ and $\exp [-C_1] = 1$. The results are depicted in fig. 3 for the choice of ρ_B and ρ_0 as indicated.

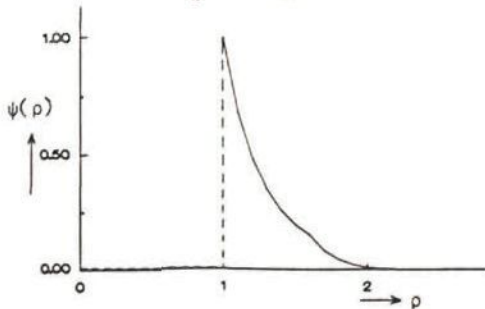


Fig. 5.3. The dimensionless particle size distribution

5.5. Synthesis and evaluation of results

Three rate determining steps have been discussed in detail, that is, two parallel steps, diffusion of nickel atoms on the alumina surface (step 2, eq (18)) and the evaporation-condensation of nickel from and to the particle surface (step 6, eq (26)), and one series step, the nucleation inhibited incorporation of nickel atoms into growing crystal faces of the particles (step 7, eq (37)). The overall rate is determined by the fastest of the first two steps and the slowest of this fastest step and the third step.

Using equations (15), (23), and (29), the data from table 4.3 and the value for h_{bulk} of $-6.0 \cdot 10^{-19} \text{ Jat}^{-1}$, the values for the various parameters are obtained as presented in table 5.1.

The equations for the growth rates of the possible rate determining steps are evaluated by introducing the calculated values of these parameters into the equations (18), (26) and (37). The results obtained

have been presented in table 5.2, using the data corresponding to (111)-nickel crystal faces and in table 5.3 using the data for (100)-faces.

Table 5.1. Parameters, to be used in growth equations for step 2 (A_1 and λ_1), step 6 (A_2 and λ_2) and 7a (A_3 and λ_3)

Parameter	(111)-face		(100)-face	
	873K	973K	873K	973K
$A_1(\text{nm}^4\text{h}^{-1})$	$8.6 \cdot 10^{-5}$	$6.7 \cdot 10^{-3}$	$1.2 \cdot 10^{-4}$	$9.4 \cdot 10^{-3}$
$A_2(\text{nm}^2\text{h}^{-1})$	$1.6 \cdot 10^{-5}$	$2.7 \cdot 10^{-3}$	$2.2 \cdot 10^{-5}$	$3.7 \cdot 10^{-3}$
$A_3(\text{nm}^{-1}\text{h}^{-1})$	$4.7 \cdot 10^3$	$1.6 \cdot 10^5$	$4.7 \cdot 10^3$	$1.6 \cdot 10^5$
λ_1	9.48	9.48	9.48	9.48
λ_2	4	4	4	4
λ_3	0.45	0.45	0.76	0.76
$\frac{2\sigma a^3}{kT}$ (nm)	4.75	4.18	6.59	5.83
$\frac{\pi\epsilon}{2kT} \left(\frac{\epsilon}{\sigma a} + \frac{3}{4} \right) (\text{nm}^{-1})$	63.2	54.7	15.5	12.6

Table 5.2. Growth rates for possible rate determining steps in nm h^{-1} ; parameters for (111)-face

Rate determining mechanism	873K	973K
Diffusion over $\text{Al}_2\text{O}_3(2)$	$\frac{9.1 \cdot 10^{-6}}{r^3} \exp \left[\frac{4.75}{r} \right]$	$\frac{7.1 \cdot 10^{-4}}{r^3} \exp \left[\frac{4.18}{r} \right]$
Evaporation from Ni-particles (6)	$\frac{4.0 \cdot 10^{-6}}{r} \exp \left[\frac{4.75}{r} \right]$	$\frac{6.8 \cdot 10^{-4}}{r} \exp \left[\frac{4.18}{r} \right]$
Nucleation on Ni-facets (7a)	$1.0 \cdot 10^4 r^2 \exp \left[\frac{4.75}{r} - 63.2r \right]$	$3.6 \cdot 10^5 r^2 \exp \left[\frac{4.18}{r} - 54.7r \right]$

Table 5.3. Growth rates for possible rate determining steps in nm h^{-1} ; parameters for (100)-face

Rate determining mechanism	873K	973K
Diffusion over $\text{Al}_2\text{O}_3(2)$	$\frac{1.3 \cdot 10^{-5}}{r^3} \exp \left[\frac{6.59}{r} \right]$	$\frac{9.9 \cdot 10^{-4}}{r^3} \exp \left[\frac{5.83}{r} \right]$
Evaporation from Ni-particles (6)	$\frac{5.5 \cdot 10^{-6}}{r} \exp \left[\frac{6.59}{r} \right]$	$\frac{9.3 \cdot 10^{-4}}{r} \exp \left[\frac{5.83}{r} \right]$
Nucleation on Ni-facets (7a)	$6.1 \cdot 10^3 r^2 \exp \left[\frac{6.59}{15.5r} \right]$	$2.1 \cdot 10^5 r^2 \exp \left[\frac{5.83}{12.6r} \right]$

The corresponding growth curves, obtained by numerical evaluation of the rate equations are presented in fig. 5.4 to 5.8.

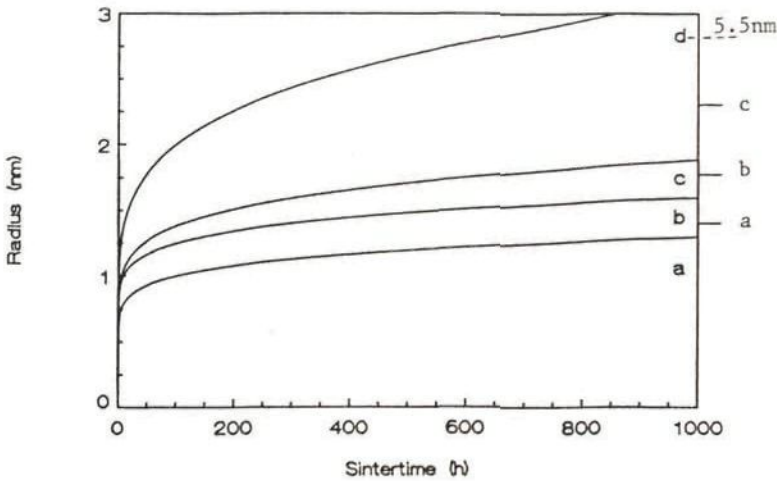


Fig. 5.4. Development of the mean particle radius with time for a dispersion of nickel particles at 873K, assuming diffusion of nickel atoms over the alumina surface to be the rate limiting step: a. data from table 5.2, (111)-face; b. data from table 5.3, (100)-face; c. based on A_1' , table 5.4; d. based on A_1'' , table 5.4.

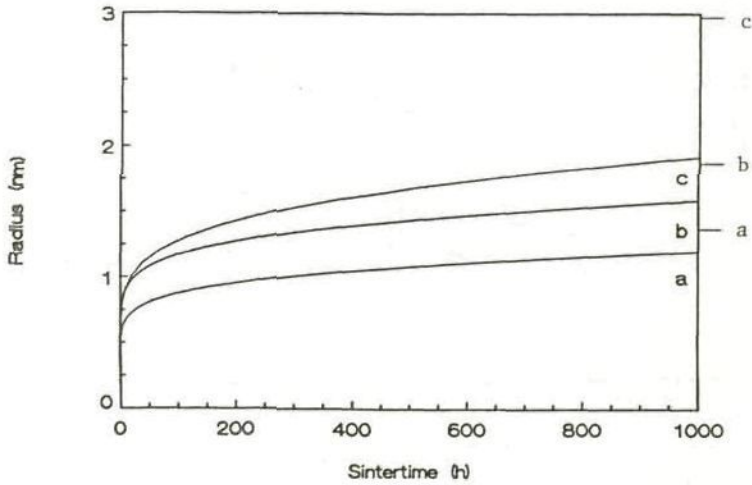


Fig. 5.5. Development of the mean particle radius with time for a dispersion of nickel particles at 873K, assuming the evaporation of nickel from the particles to be the rate limiting step:
 a. data from table 5.2, (111)-face; b. data from table 5.3, (100)-face;
 c. based on A_2' , table 5.4

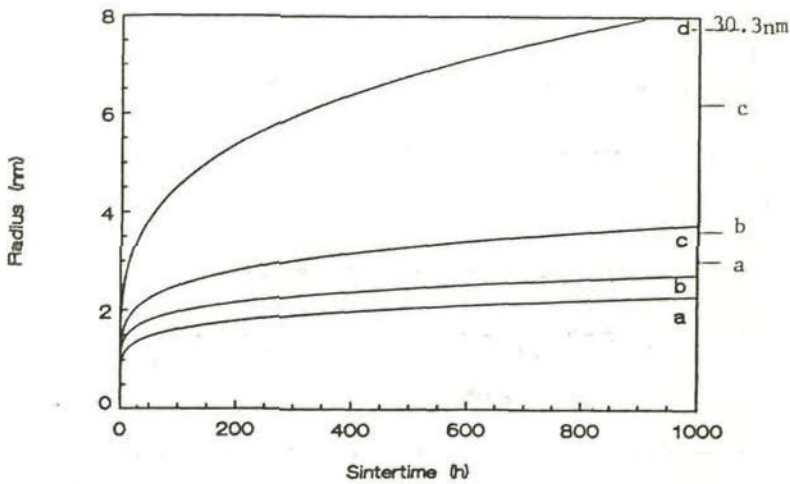


Fig. 5.6. Development of the mean particle radius with time for a dispersion of nickel particles at 973K, assuming diffusion of nickel atoms over the alumina surface to be the rate limiting step:
 a. data from table 5.2, (111)-face; b. data from table 5.3, (100)-face;
 c. based on A_1' , table 5.4; d. based on A_2'' , table 5.4.

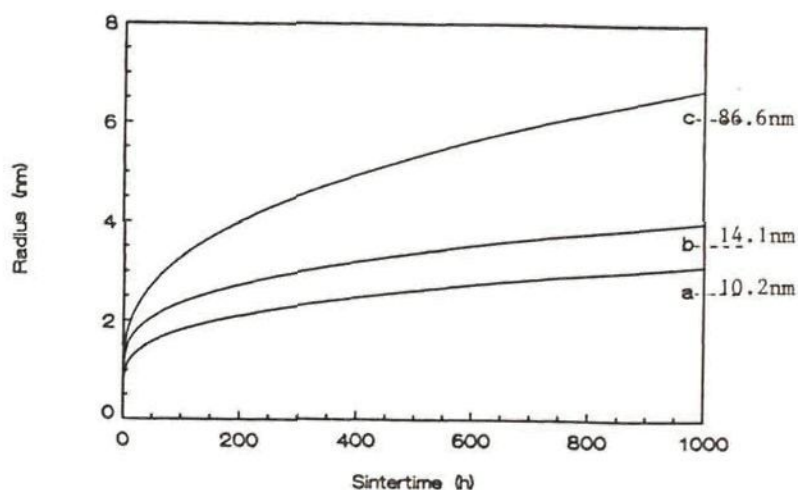


Fig. 5.7. Development of the mean particle radius with time for a dispersion of nickel particles at 973K, assuming the evaporation of nickel from the particles to be the rate limiting step:
a. data from table 5.2, (111)-face; b. data from table 5.3, (100)-face;
c. based on A_2' , table 5.4

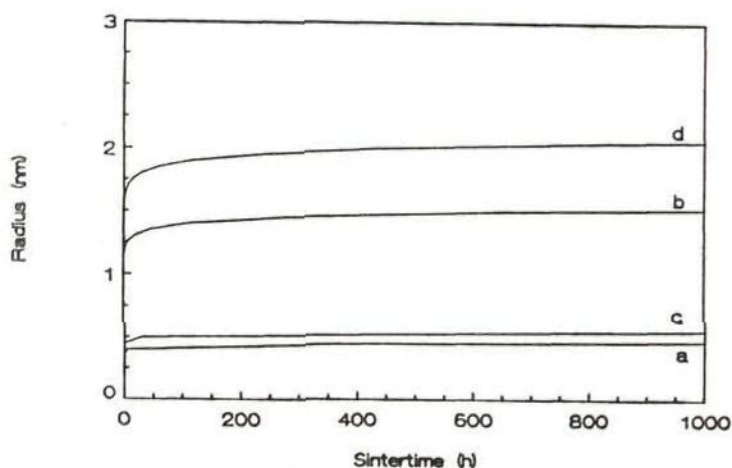


Fig. 5.8. Development of the mean particle radius with time for a dispersion of nickel particles, assuming two-dimensional nucleation at the crystal faces to be the rate limiting step; data from table 5.2 and 5.3:
a. 873K, (111)-face; b. 873K, (100)-face; c. 973K, (111)-face;
d. 973K, (100)-face

The main results, shown by these graphs, can be characterized as follows:

- At 873K, without nucleation inhibition, diffusion of nickel atoms over the alumina carrier (step 2) is the predominating growth mechanism. For particle dispersions with an average radius larger than 2 nm, the smallest size considered in the experiments, the growth rate is very small and no perceptible growth is to be expected.
- At 973K, again without nucleation inhibition, evaporation of nickel from the smaller particles and recondensation on the larger ones (step 6) is the dominating growth mechanism. For particle dispersions with an average radius larger than 4 nm the growth rate is so small, that no perceptible growth is to be expected.
- As soon as nucleation inhibition dominates the growth process the growth rates are reduced very much for particle dispersions with average radius greater than 0.5 nm at 873K and 2 nm at 973K.

Nucleation inhibition only occurs for particles with well developed low index crystal faces. Generally small particles will not have such facets. Only after a certain size is passed crystal faces will develop. At this stage nucleation inhibition will become effective. The results show, that at this moment the immediate consequence must be, that further crystal growth stops.

The results, as discussed so far, are underlined in fig. 5.4 to 5.7, by indicating in the right hand margin of these figures the sizes at which the very low growth rate of 10^{-4} nm h⁻¹ will be obtained for the different rate determining steps. It will be seen, that at 973K, if very long times are available and no nucleation inhibition occurs, growth could continue to large average radii. This is not the case at 873K.

As the present conclusions are very important for the interpretation of the experimental results, it is worth while to see to what extent the various numerical results depend on the assumptions used in their

derivation.

Looking at the relevant equations, (18) for step 2, (26) for step 6 and (37) for nucleation inhibition, three factors will be considered successively: $\exp \left[\frac{2\sigma a^3}{kT} \right]$, $\exp \left[- \frac{\pi \epsilon}{2kT} \left(\frac{\epsilon}{\sigma a} + \frac{3}{4} \right) r \right]$ and A_i / λ_i .

1. The common factor $\exp \left[\frac{2\sigma a^3}{kT} \right]$ of all three processes.

This factor arises out of an improved approximation of the driving force for particle growth, so far not used by other authors (see section 4.5.). Its effect is largest for small average particle radii, leading to a very fast initial growth, and peters out for average particle radii approaching $r=2\sigma a^3/kT$. The results, therefore, depend essentially on the choice that has been made for the surface free energy, σ . This is the reason for the differences of the growth curves evaluated for mechanisms 2 and 6, using the parameters for (111)- and (100)- faces (see fig. 5.4 to 5.7).

It is seen, that the particle radii, attained after for instance 1000 h, are not greatly influenced by the difference in the values of σ for the (111)- and the (100)-face.

The values chosen for σ depend on the assumptions for its relation to h_{bulk} as given in table 4.3. In section A-3 the predictions have been compared with experimental data. It is seen that the value of σ chosen for the (111)-face should be considered as a maximum value. In that respect the results for the (111)-face should be considered as more reliable than those for the (100)-face.

2. The factor $\exp \left[- \frac{\pi \epsilon}{2kT} \left(\frac{\epsilon}{\sigma a} + \frac{3}{4} \right) r \right]$, which dominates the rate of nucleation inhibited growth.

The effect of this factor is important for $r > \left[\frac{\pi \epsilon}{2kT} \left(\frac{\epsilon}{\sigma a} + \frac{3}{4} \right) \right]^{-1}$.

From table 5.1 it is seen, that widely different values are obtained for the coefficient of r in the exponent by using the values of ϵ and σ applying to (111)- and (100)- faces, respectively. The corresponding values for $\left[\frac{\pi \epsilon}{2kT} \left(\frac{\epsilon}{\sigma a} + \frac{3}{4} \right) \right]^{-1}$ are 0.016 and 0.065 nm at 873K and 0.018 and 0.080 nm at 973K.

Fig. 5.8 shows, that the estimates of ϵ and σ for the (111)- face lead to very low rates of nucleation inhibited growth, while those for the

(100)-face lead to a reduced, but still substantial inhibition of growth, as soon as nucleation is required.

It is reasonable to assume, that the estimates of ϵ and σ for the (100)-face represent a situation allowing of the largest nucleation inhibited growth rates possible. Even these rates bring crystal growth to a standstill for average particle radii greater than 2 nm.

In section A-4 further refinements have been discussed for the estimates of ϵ and σ , connected with the proper values of the lattice parameter to be introduced in the parameters σ^*a^2 and ϵ^*a as given in table 4.3. Taking into account of these refinements leads to slightly different values for the factors under discussion. The corresponding line of table 5.1 should now be read as:

Parameter	(111)-face		(100)-face	
	873K	973K	873K	973K
$\frac{\pi\epsilon}{2kT} \left(\frac{\epsilon}{\sigma a} + \frac{3}{4} \right) \text{ nm}^{-1}$	57.9	50.0	14.9	12.0

The difference in the parameter values are substantial, but the effects on the growth curves very minor.

3. The factors $\frac{A_1}{\lambda_1}$, $\frac{A_2}{\lambda_2}$ and $\frac{A_3}{\lambda_3}$.

Uncertainties in the parameters λ are of minor importance within the purposes of this chapter. The values taken for λ_1 and λ_2 are minimum values, leading to maximum values of the predicted growth rates.

Uncertainties in the factors A_1 are much more important. The factors A_1 and A_2 , used so far, are essentially those derived from table 4.5 and discussed in section 4.7. As mentioned there, all adsorbed species and transition states have been assumed to be localized, while vibrational contributions to the entropies of bulk nickel and the adsorbed species have been neglected. In section A.1 and A.2 better approximations have been discussed. The results have been assembled in table A.7. In order to check the sensitivity of the overall results to

the values of A_1 and A_2 , in fig. 5.4 to 5.7, growth curves have been added, calculated with values of A_1 and A_2 , derived from the data in table A.7. The values A_1' and A_2' , so used, have been presented in table 5.4 and should be compared to those of table 5.1. In order to evaluate a possible effect of mobility of adatoms at the alumina surface, in fig. 5.4 and 5.6 also growth curves have been presented for this version of rate limitation by diffusion of adatoms over the alumina surface. The corresponding values of A_1'' , calculated using data from table A.2 and A.3, also have been presented in table 5.4. It should be kept in mind here, that the growth rate now is proportional to r^{-2} . This influences the value of λ_1 , which now turns out as 6.75.

Table 5.4. Revised parameters, to be used in growth equations for step 2 (A_1' , A_1'' and λ_1'') and step 6 (A_2')

Parameter, (111)-face	873 K	973 K
A_1' (nm^4h^{-1})	$1.4 \cdot 10^{-3}$	$1.1 \cdot 10^{-1}$
A_1'' (nm^3h^{-1})	$9.0 \cdot 10^{-3}$	$5.4 \cdot 10^{-1}$
λ_1''	6.75	6.75
A_2' (nm^2h^{-1})	$2.4 \cdot 10^{-4}$	$3.3 \cdot 10^{-2}$

In connection with the factor A_3 , it has been shown in section A.2, that the rate of nucleation inhibited growth is only slightly influenced by the introduction of corrections, due to vibrational entropies of bulk nickel and absorbed nickel atoms. Moreover the structure of the growth equation (5.37) in combination with the parameter values of table 5.1 is such, that very wide variations in the value of A_3 have very little influence on the value of the particle radius, where growth effectively comes to a standstill.

Reviewing the earlier conclusions as to the maximum radii, attainable by growth under circumstances where nucleation inhibition is not effective, it should be kept in mind that the modified growth rates, as obtained now, should be considered as maximum values. Three reasons can

be mentioned, viz:

- The value of h_{bulk} , used for the calculations, must be considered as a lower limit, see section A.3.
- The value of σ (111) used must be considered as a higher limit, see also section A.3.
- All possible extra activation energies in the transition states have been neglected.

Fig. 5.4 and 5.5 show, that at 873 K the maximum particle radius to be expected after 1000 h of growth is 3 nm. From fig. 5.6 and 5.7 it is seen, that at 973 K growth in 1000 h to particle radii of 8 nm is possible.

5.6. References

- [1] I.M. Lifshitz; V.V. Slyosov: J. Phys. Chem. Solids 19 (1961) 35.
- [2] C. Wagner: Z. Electrochem. 65 (1961) 581.
- [3] B.K. Chakraverty: J. Phys. Chem. Solids 28 (1967) 2401.
- [4] T.M. Ahn; J.K. Tien: J. Phys. Chem. Solids 37 (1976) 771.

6. GENERAL ANALYSIS OF RESULTS

6.1. Introduction

An extended thermodynamic and kinetic analysis of the growth of individual supported particles, in chapter 4, shows that during sintering mass transport from one particle to another is governed by evaporation of nickel from the particles, and diffusion of the nickel atoms along the support. For these rate determining process steps the rate of the Ostwald ripening process of a supported particle dispersion was evaluated in chapter 5 and will now be used for further analysis of the experimental results as presented in chapter 2 and 3.

This will be done by first confronting the results of the sinter experiments with the theoretical predictions. After that the information on the chemical composition of the metal support interface will be analyzed, in order to come to a better understanding of some of the factors that might govern the sintering process.

The new developed approach will then be tested using the experimental data of P. Wynblatt et al. [1], sintering a Pt/Al₂O₃ model catalyst in an oxygen atmosphere.

6.2. Confrontation of experimental kinetic data with theoretical predictions

6.2.1. Kinetics of the Ostwald ripening process

Sintering of the model catalyst at 873 K will not be discussed any further because, as already concluded in section 2.6, the supports used do not meet the requirements made for this sinter study. Also, according to the theoretical predictions of section 5.5, at 873 K very low growth rates are to be expected in dispersions with average particle radii in excess of 3 nm.

In fig. 6.1 the growth curves for mass transport through the vapour phase (a) and by diffusion along the support (b), as evaluated in section 5.5, are given for 400 hours processing at 973 K.

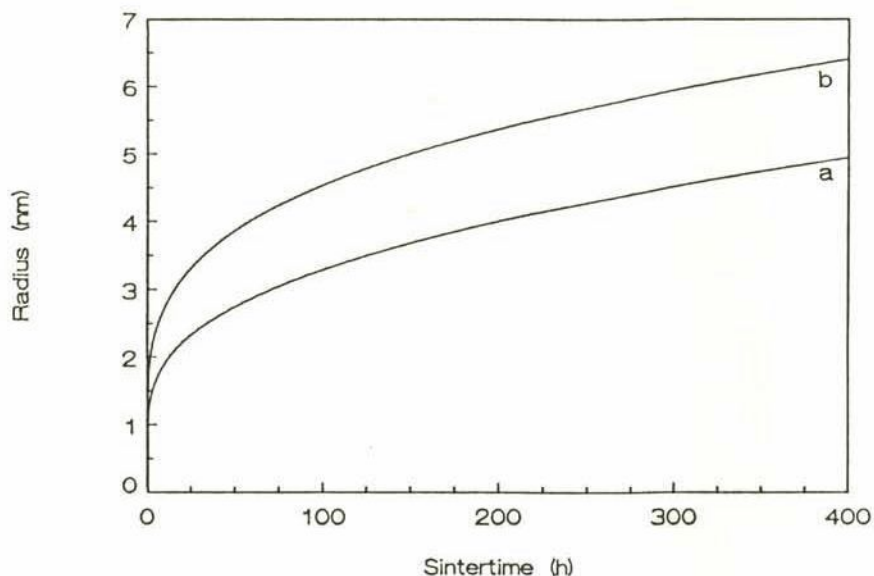


Fig. 6.1. Development of the mean particle radius with time for a dispersion of nickel particles at 973 K;
a: evaporation of nickel rate determining, based on A_2' from table 5.4
b: diffusion over alumina rate determining, based on A_1'' from table 5.4

From these theoretical growth curves it can be seen that the highest growth rate possible is predicted assuming substrate diffusion including mobile adsorption. Sintering of the metal dispersion by evaporation-condensation can therefore be neglected and from now on the discussion will be focussed on fig. 6.2, where the theoretical growth curves for substrate diffusion are combined with the experimental data.

For the initial stage of sintering the experimental data, except those of catalyst F(o), agree well with the theoretical growth curve for mobile adsorption with an activation energy in between those evaluated for (111) and (100) faces of nickel (see chapter 4). There may be a small influence of the additives on the activation energy for sintering in this range, but the data are too restricted for further analysis. Greater differences between the various samples occur, when the

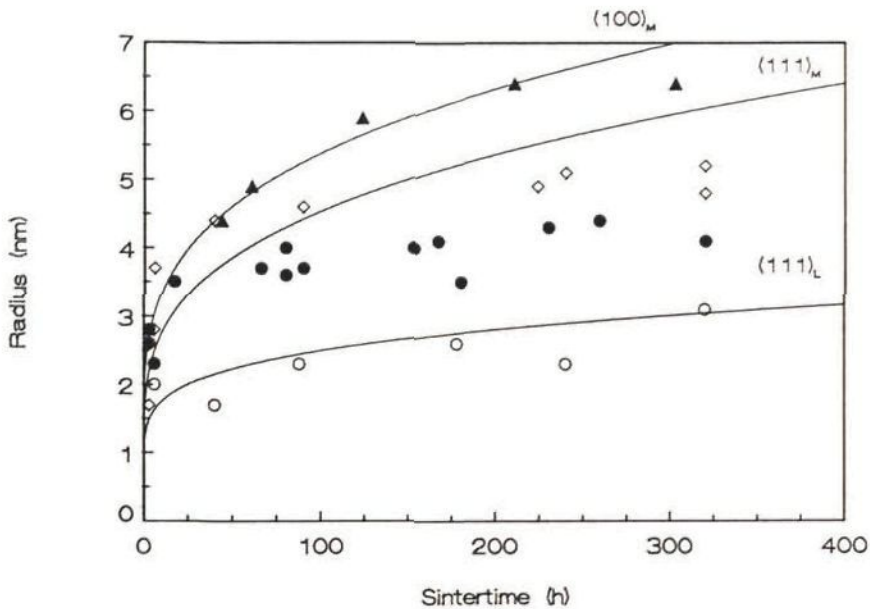


Fig. 6.2. Development of the mean particle radius with time, as predicted by the growth model assuming diffusion along the support (solid lines) for:

- $(111)_L$: localized adsorption on alumina, activation energies evaluated for nickel (111) face
- $(111)_m$, $(100)_m$: mobile adsorption on alumina, activation energies evaluated for nickel (111) and (100) faces, respectively.

Data as determined for the different model catalysts: Cat. F, Ni/Cr/Al₂O₃(○); Cat. E, Ni/Al₂O₃(●); Cat. H, Ni/Mn/Cr/Al₂O₃(◇) and Cat. G, Ni/Mn/Al₂O₃(▲).

sintering is further continued. Assuming, that the diffusion of nickel adatoms along the support is the governing step, still various factors might be influenced by the additives.

In chapter 5, it has been predicted already that as soon as the metal particles develop well formed crystal faces, nucleation inhibition does stop further growth. Additives might influence facet formation. Also, as can be seen from fig. 6.2, for a particle dispersion of mean particle radius larger than 3 nm, growth rate is very sensitive to the transition from the localized to the mobile adsorption mode. Slight

changes in the adsorption mode could be introduced by variations of activation energy for diffusion over the alumina surface, caused by the various additives. A third factor influenced by additives might be in the surface free energy of the nickel particles and hence in the driving force for sintering.

Addition of chromium, catalyst F, almost directly introduces stabilization of the mean particle size. Growth kinetics resembles the model for rate determining substrate diffusion in the localized mode. This indeed would suggest an influence through the activation energy for diffusion over the alumina surface. As such, this effect on the properties of the alumina surface would appear to be more probable than the other effects, which would require influences of the additives on the nickel surface.

Catalyst G represents a different effect, namely a coarse dispersion already after desintegration of the nickel film. As can be seen from fig. 6.2 the higher stabilization level reached by introducing manganese is not only caused by the coarser initial dispersion, but also by a longer initial stage of sintering. Here mobility of adatoms on alumina might have been enhanced.

Model catalyst H, containing chromium as well as manganese, exhibits a fine nickel dispersion just as catalyst F, containing chromium. The high stabilization level seems to be accompanied with an increased duration of the initial stage of sintering as compared with the nickel-alumina catalyst E, a phenomenon also observed in the manganese containing model catalyst G.

6.2.2. The particle size distributions

From the PSD's as given in chapter 2, it can be seen that during the second stage of sintering, characterized by a constant mean particle size, the dispersion is not at all stable. There is still a changing of the size distribution going on, although the electron micrographs do expose faceted crystallites. So, despite faceting of the crystallites, there is some mass transport leading to broadening of the particle size distribution, however, without significantly affecting the mean

particle size. Additional information, not available, would therefore be required for further analysis of the second stage of sintering.

6.3. The chemical composition of the metal support interface

During heat treatment at 973 K in hydrogen, the metal deposits on the alumina support react with the alumina creating a diffusion layer, which consists of (see chapter 3 and section 2.3):

Ni/Al ₂ O ₃	→ solid solution of nickel oxide in alumina
Ni/Cr/Al ₂ O ₃	→ nickel chromate
Ni/Mn/Al ₂ O ₃	→ manganese aluminate and a solid solution of nickel oxide in alumina

There is a clear tendency of nickel to diffuse, in the form of Ni²⁺-ions, into the alumina carrier. This diffusion is precluded, however, by the presence of chromium. But also in this case a boundary layer is definitely present.

In section 6.2.1. it has been concluded, that the sinter behaviour of the model catalysts is strongly influenced by the additives Cr and Mn and that these effects are probably due to their influence on the diffusion of nickel adatoms over the alumina surface.

The question remains, to what extent variations in sinter stability might be influenced by the diffusion layers, discussed here. In principle such an effect might be possible. In thin film technology [2] *it is known that crystals grown on a substrate with a different structure are rather irregularly shaped, because of the mismatch of the crystal lattices. Matching of the crystal lattices can be realized by the formation of an intermediate diffusion layer, thereby restoring the regular shape of the crystallites grown.*

In other words, the formation of low index crystal faces on the nickel particles might be influenced by the presence of diffusion boundary layers and through nucleation inhibition this would influence sintering very strongly.

Indeed a certain amount of facet formation on the nickel crystallites is observed during sintering. But these observations are scanty and do

not allow for any discrimination between model catalysts without additives or with special types of additives. Much more systematic research would be required to come to conclusions here.

6.4. Analysis of the sintering of Pt/Al₂O₃ model catalysts in oxygen

The sinter studies of Pt/Al₂O₃ systems, reported by P. Wynblatt [1], involved sintering of a model catalyst in an oxygen atmosphere ($p_{O_2} = 2$ kPa) at 873 K and 973 K. In the presence of oxygen a volatile oxidic species is formed. Such a species with a high affinity for the oxidic substrate will show limited mass transport by adatom diffusion along the substrate. Sintering will therefore be determined by mass transport through the vapour phase.

Following the thermodynamic and kinetic models as presented in chapter 4 and 5, the growth curves have been evaluated and presented in fig. 6.3. and 6.4 together with the experimental data of P. Wynblatt. For the initial stage of sintering a quite satisfactory agreement is found between the data and the growth model. At a certain stage of the process, average radius of 8 nm at 873 K and 10 nm at 973 K, the mean particle size levels out very abruptly. This must be caused by nucleation inhibition due to facet formation of the crystallites. Indeed such a facet formation is shown by the electron micrographs.

The present interpretation to a certain extent is in contrast with that of T.M. Ahn et al. [3]. They appoint nucleation inhibition as the *sinter mechanism right from the start. There are two main differences* between our kinetic model and the analysis of T.M. Ahn leading to the discrepancy viz:

- the exponential term: $\exp \left[\frac{2\sigma a}{kTr} \right]$.

As illustrated in section 5.5 this factor does have a remarkable influence on the sinter rate. By neglecting this term growth is underestimated, especially during the initial stage.

- the edge energy.

T.M. Ahn et al. have evaluated this energy parameter by curve

fitting, whereas we have used a broken bond model. As no direct experimental information is available, the feasibility of the estimates cannot be judged. We feel Ahn's estimates to be extremely low.

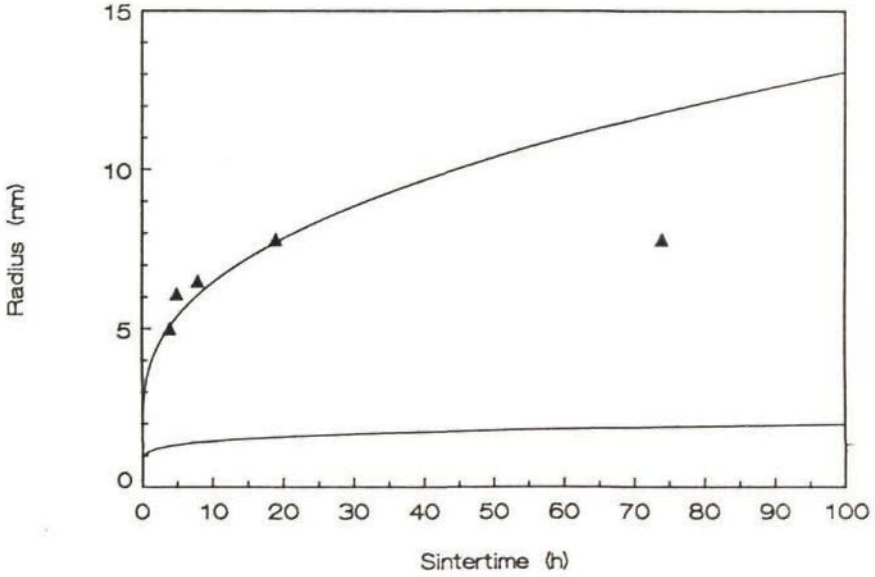


Fig. 6.3. Development of the mean particle radius with time for a dispersion of platinum particles at 873 K and oxygen pressure of 2 kPa, assuming the evaporation of platinum oxide from the particle to be the rate limiting step;

a. for localized transition state; $\frac{dr}{dt} = \frac{9.25 \cdot 10^{-5}}{r} \exp\left[\frac{8.18}{r}\right] \text{ nm h}^{-1}$

b. for mobile transition state ; $\frac{dr}{dt} = \frac{0.31}{r} \exp\left[\frac{8.18}{r}\right] \text{ nm h}^{-1}$

Pt: $h_{\text{bulk}} = -8.83 \cdot 10^{-19} \text{ J}$
 $a = 2.47 \cdot 10^{-10} \text{ m}$

$$\ln \frac{p(\text{PtO}_2)}{p(\text{O}_2)} = 0.860 - \frac{20140}{T}$$

[3]

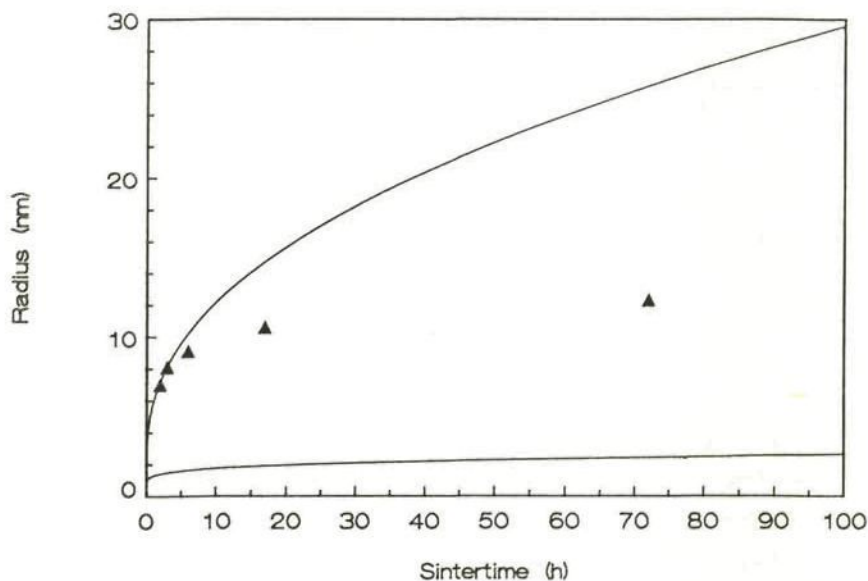


Fig. 6.4. Development of the mean particle radius with time for a dispersion of platinum particles at 973 K and oxygen pressure of 2 kPa, assuming the evaporation of platinum oxide from the particle to be the rate limiting step;

a. for localized transition state; $\frac{dr}{dt} = \frac{7.55 \cdot 10^{-4}}{r} \exp\left[\frac{7.25}{r}\right] \text{ nm h}^{-1}$

b. for mobile transition state ; $\frac{dr}{dt} = \frac{2.90}{r} \exp\left[\frac{7.25}{r}\right] \text{ nm h}^{-1}$

6.5. General conclusions

In the preceding sections it has been shown, that the theoretical treatment, presented in chapter 4 and 5, gives a better qualitative description of the growth of dispersions of supported metal particles than earlier proposals in literature. That is mainly due to the introduction of an improved series development of the factor representing the supersaturation. More important, however, is the question whether the quantitative treatment of chapter 4 and 5 also is justified. In answering this question let us first notice, that the number of essential parameters involved appears to be less than one might expect. Two of these parameters turn out to be of essential

importance:

- the combination, $\sigma a^2/kTr$, governs the very rapid initial growth, that occurs when the particles are so small that the value of this parameter is substantially greater than unity;
- the heat of evaporation of the bulk metal, as indicative for the other energy parameters involved, determines the particle size where the rate of sintering diminishes very rapidly.

The results of the quantitative estimates, however, appear to be very sensitive to some kinetic factors, that are difficult to establish beforehand: the mobility of the metal adatoms on the carrier surface and the mobility of the transition state for adsorption and desorption. The comparison with experiments on Ni/Al₂O₃ and Pt/Al₂O₃ has shown that only the assumption of high mobility in both cases yields the high growth rates observed experimentally. In other words, this finding might be interpreted as showing, that there is a tendency for our quantitative predictions to underestimate the growth rates as observed. This is an interesting contrast with the field of catalysis, where the application of Eyring's theory of absolute reaction rates usually leads to overestimates in comparison with observations.

The experiments described in this thesis apply to model systems with rather large metal particles: radii in the range from 2 to 10 nm. This might be adequate for the catalysts studied in our laboratory, nickel/alumina methanation catalysts, but many industrial nickel and platinum catalysts contain smaller particles, down to radii of 0.2 or 0.3 nm. On the other hand, inevitably for the study of the model systems, higher sinter temperatures had to be applied than allowed for the stability of supported fine grain metal catalysts.

In order to apply the predictions of this thesis to such systems a certain amount of extrapolation would be required. In comparing small particles and low temperatures on one hand and large particles and high temperatures on the other hand, still three aspects might be mentioned here:

- During the growth of large particles well formed low index crystal faces may develop, leading to nucleation inhibition of particle

growth and hence a considerable stabilization of particle size; unfortunately, for structure sensitive reactions this also could mean the end of catalytic activity; for small particles facet formation is much less probable.

- At high temperatures the vapour pressure and the rate of evaporation may be so high, that the active metal is carried away from the sample; in industrial catalysis the active metal might be transported through the catalyst bed and out of the reactor; the considerations of chapter 5 have shown, that the preference for growth vs. transport depends on a rather delicate balance between the various parameters involved. The geometry of the carrier pore system might also be very important here.

- All considerations so far apply to the role of Ostwald ripening in the sintering of the metal particles in a catalyst; in the introduction it has been mentioned, that sintering of the carrier must be an important factor too; even in the experiments with our model system it has turned out that the stability of the alumina carrier film cannot be taken for granted; on first sight it is to be expected that in actual catalysis Ostwald ripening is more important for small metal particles at relatively low temperatures, while sintering of the support will predominate for larger metal particles at higher temperatures.

Finally a word about the effect of additives. As mentioned earlier additives may be used to enhance the sinter stability of a catalyst carrier. From the experiments described in this thesis it is clear, that additives also may influence the Ostwald ripening of supported metal particles, both favourably and unfavourably. The most probable effect responsible has turned out to be the influence of additives on the diffusion of metal adatoms over the carrier surface. The experience assembled at present is far too scanty, however, for direct explanations and predictions.

6.6. References

- [1] P. Wynblatt; N.A. Gjostein: Acta Metall. 24 (1976), 1165, 1175.
- [2] H.G. Schneider; V. Ruth; Advances in Epitaxy and Endotaxy,
VEB Deutscher Verlag für Grundstoffindustrie, Leipzig 1971.
- [3] T.M. Ahn; J.K. Tien: J. Phys. Chem. Solids 37 (1976), 771, 777.

APPENDIX: ANALYSIS OF APPROXIMATIONS IN THE KINETIC AND THERMODYNAMIC BASIS OF CHAPTER 4 AND 5

A.1. Mobility of adsorbed nickel atoms

All considerations of chapter 4 have been based on the assumption, that the adsorption of nickel atoms on nickel and on alumina is strictly localized. The temperatures involved, however, are rather high and two-dimensional mobility of adsorbed nickel atoms cannot be excluded. Such mobility could influence the rates of adsorption and desorption (particularly step 3 and 6 of chapter 4) and the rates of diffusion of nickel atoms over the surfaces (step 2 and 8 of chapter 4). In order to study the effects of possible mobility we start by repeating the relevant part of table 4.1, but now with the formulas appropriate to mobile adsorption.

Table A.1. Chemical potential of Ni in the various states in which it may occur, assuming two-dimensional mobility for the adsorbed state and the transition state for adsorption and desorption.

state of nickel	μ/kT
vapour	$\ln \frac{p}{kT} + \frac{3}{2} \ln \frac{h^2}{2\pi mkT}$
adsorbed state	$\frac{h'_{ads}}{kT} + \ln n_{ads} + \ln \frac{h^2}{2\pi mkT}$
transition state	$\ln n^{\ddagger} + \ln \frac{h^2}{2\pi mkT}$

Here we may assume that:

$$h'_{ads} = h_{ads} + u_{act}$$

where h'_{ads} is the enthalpy of the mobile adsorbed state, while h_{ads} is the enthalpy of the localized adsorbed state and u_{act} is the activation

energy for the jumps of nickel atoms from one localized site to another.

Analogously to equations (4.7), (4.8) and (4.9) now the following equations can be derived:

- for the rate of desorption:

$$v_d = \frac{kT}{h} n_{ads} \exp \left[\frac{h_{ads} + u_{act}}{kT} \right] \quad (1)$$

- for the rate of adsorption:

$$v_a = \frac{kT}{h} \frac{p}{kT} \left(\frac{h^2}{2\pi mkT} \right)^{1/2} \quad (2)$$

- for the adsorption equilibrium, $v_a = v_d$:

$$n_{ads} = \frac{p}{kT} \left(\frac{h^2}{2\pi mkT} \right)^{1/2} \exp \left[\frac{-(h_{ads} + u_{act})}{kT} \right] \quad (3)$$

Comparison of equations (1), (2) and (3) with (4.7), (4.8) and (4.9) shows that:

$$\frac{v_a \text{ (mobile)}}{v_a \text{ (localized)}} = \frac{v_d \text{ (mobile)}}{v_d \text{ (localized)}} = a^2 \left(\frac{h^2}{2\pi mkT} \right)^{-1} \quad (4)$$

where the substitution $n_0 = a^{-2}$ is used, and:

$$\frac{n_{ads} \text{ (mobile)}}{n_{ads} \text{ (localized)}} = a^2 \left(\frac{h^2}{2\pi mkT} \right)^{-1} \exp \left[\frac{-u_{act}}{kT} \right] \quad (5)$$

These equations hold both for adsorption on nickel and adsorption on alumina.

Using the same numerical values as in chapter 4, the results as tabulated in table A.2 have been obtained. It is seen, that mobile adsorption is strongly favoured on alumina and is in the balance for nickel. The rates for adsorption and desorption are found to be much greater for mobile, than for localized adsorption.

Table A.2. Comparison of adsorption-desorption rates and adsorption equilibria for mobile and localized adsorption

	nickel		alumina	
	873K	973K	873K	973K
$\frac{v \text{ (mobile)}}{v \text{ (localized)}}$	830	920	830	920
$\frac{n_{\text{ads}} \text{ (mobile)}}{n_{\text{ads}} \text{ (localized)}}$	0.21	0.54	27	42

A first conclusion to be drawn is, that it is wise at least to assume two dimensional mobility for the transition states for adsorption and desorption. Then the difference between the rates of adsorption (and desorption) for mobile and localized adsorption disappear and for both modes the high rates of table A.2 apply. In the next section of this appendix, starting with table A.4, this choice will be followed through. This choice, however, does not influence the adsorption equilibria, neither the balance between mobile and localized adsorption. In the next section it will be shown, that the inclusion of vibrational entropy contributions to the chemical potentials do shift the balance between mobile and localized adsorption in the sense, that for nickel localized adsorption is far predominant, while for alumina localized adsorption is favoured, but there is still a certain competition from mobile adsorbed atoms.

In view of a possible contribution of mobile adsorbed atoms on alumina, it is still necessary to see to what extent the transport of nickel atoms over the alumina surface (step 2 of chapter 4) is influenced by mobility. For localized adsorbed atoms the transport is a diffusion process as a consequence of the activated random jumping of nickel atoms from one site to a neighbour site. According to section 4.3.2 the maximum flux towards or from nickel particles by this diffusion is:

$$\phi = \frac{2\pi D}{\ln 2} n_{\text{ads}} \quad \text{at } s^{-1} \quad (6)$$

The diffusion coefficient is given by eq (4.17). Numerical evaluation along the lines used throughout leads to values of $7.2 \cdot 10^{-9} \text{ m}^2 \text{ s}^{-1}$ at 873K and $1.15 \cdot 10^{-8} \text{ m}^2 \text{ s}^{-1}$ at 973K.

For mobile adsorption, the coverage is so low (of the order of magnitude of 10^4 at m^{-2}) that the nickel atoms may be considered as a two dimensional Knudsen gas. The flux towards a nickel particle then may be given as:

$$\phi = \frac{1}{2} \left(\frac{\pi kT}{2m} \right)^{1/2} 2\pi r n_{\text{ads}} \quad \text{at.s}^{-1} \quad (7)$$

In table A.3 the numerical estimates following from eq (6) and (7) have been compared.

Table A.3. Comparison of flux due to diffusion of localized adatoms and to collision of mobile adatoms (r in nm).

	873K	973K
$\frac{\phi \text{ (mobile)}}{\phi \text{ (localized)}}$	$69 r \frac{n_{\text{ads}} \text{ (mobile)}}{n_{\text{ads}} \text{ (localized)}}$	$47 r \frac{n_{\text{ads}} \text{ (mobile)}}{n_{\text{ads}} \text{ (localized)}}$

It is seen, that a small fraction of mobile adatoms still can have a significant contribution to the transport.

A.2. Equilibria and growth rates

Equilibria and reaction rates are determined by chemical potentials, defined for the species i as:

$$\mu_i = \left(\frac{\partial G}{\partial N_i} \right)_{p,T}$$

where G is the Gibbs free energy and N is the number of molecules of the species concerned. Thus far all contributions to the chemical potential due to vibrations have been neglected, while possible translations of adsorbed atoms have only been considered in section 1

of this appendix. Rotational contributions have no effect anyway, as nickel vapour is a monoatomic gas.

Full expressions for the chemical potentials are presented in table A.4. As is seen, the vibrational pattern of adsorbed atoms is simplified by assuming one vibration mode perpendicular to the surface and two modes parallel to the surface. As suggested in section 1, the transition states for desorption have been assumed to have complete two dimensional mobility, while the transition state for the transfer of atoms from the nickel to the alumina surface is assumed to have one dimensional mobility along the particle circumference. Extra activation energies for the processes involved still have been neglected.

The quantities h_{bulk} and h_{ads} , encountered earlier, now have to be interpreted as:

$$h_{bulk} = h_0 - 9/8 k\theta_D \text{ for nickel}$$

$$h_{ads} = h_a + 1/2 hv_1 + hv_2 \text{ for localized adsorption} \quad (8)$$

$$\text{and } h_{ads} = h_a + 1/2 hv_1 + u_{act} \text{ for mobile adsorption}$$

The terms in the chemical potentials, not accounted for earlier, are presented in table A.5 as $\Delta\mu/kT$. Numerical values at 873 K and 973 K are given in the last two columns of this table. To obtain these values, estimates have to be made of the frequencies ν_1 and ν_2 for the adsorbed states on nickel and alumina. Fortunately here the available margins are relatively small.

A reasonable estimate for ν_1 for nickel can be made by assuming:

$$\frac{hv_1}{k} = \theta_D = 370 \text{ K}$$

The corresponding contribution to μ/kT is:

$$\ln \left(1 - \exp \left[- \frac{hv_1}{kT} \right] \right) = 1.06 \text{ at } 873 \text{ K}$$

Table A.4. Chemical potentials of Ni, corrected for vibrational contributions

state of nickel	μ
vapour	$kT \ln \frac{p}{kT} - \frac{3}{2} kT \ln \frac{2\pi m kT}{h^2}$
solid	$h_0 + 9/8 k\theta_D - kT\phi\left(\frac{\theta_D}{T}\right) + 3 kT \ln \left(1 - \exp\left[\frac{-\theta_D}{T}\right]\right)$
adsorbed state (localized)	$h_a + 1/2 h\nu_1 + h\nu_2 + kT \ln n_{ads} + kT \ln a^2 + kT \ln \left(1 - \exp\left[\frac{-h\nu_1}{kT}\right]\right) + 2 kT \ln \left(1 - \exp\left[\frac{-h\nu_2}{kT}\right]\right)$
adsorbed state (mobile)	$h_a + 1/2 h\nu_1 + u_{act} + kT \ln n_{ads} - kT \ln\left(\frac{2\pi m kT}{h^2}\right) + kT \ln \left(1 - \exp\left[\frac{-h\nu_1}{kT}\right]\right)$
transition state for desorption	$kT \ln n^+ - kT \ln \frac{2\pi m kT}{h^2}$
transition state at the edge between nickel particle and alumina surface	$h_a(Al_2O_3) + kT \ln n^+ + kT \ln \left(1 - \exp\left[\frac{h\nu_2}{kT}\right]\right) + - \frac{1}{2} kT \ln \frac{2\pi m kT}{h^2}$

- h_0 and h_a are the enthalpies at absolute zero of the solid and the adsorbed states with respect to the vapour;
- θ_D is the Debye temperature of nickel ($\theta_D = 370$ K);
- $\phi(u) = \frac{3}{u} \int_0^u \frac{x^3}{e^x - 1} dx$;
- ν_1 and ν_2 are the vibrational frequencies of the adsorbed atoms in the direction perpendicular and parallel to the surface.

Table A.5. $\Delta\mu/kT$ for the different states of nickel

state of nickel	$\Delta\mu/kT$	873 K	973 K
vapour	not influenced	-	-
solid	$-\phi\left(\frac{\theta_D}{T}\right) + 3 \ln\left(1 - \exp\left[-\frac{\theta_D}{T}\right]\right)$	-4.0	-4.3
adsorbed state, nickel particle	$\ln\left(1 - \exp\left[-\frac{h\nu_1}{kT}\right]\right) +$	-5.8	-6.1
ibid, alumina carrier	$2 \ln\left(1 - \exp\left[-\frac{h\nu_2}{kT}\right]\right)$	-6.8	-7.1
transition state for desorption	$-\ln\frac{2\pi m kT}{h^2} - \ln a^2$	-6.7	-6.8
transition state at the edge between nickel particle and alumina surface	$\frac{1}{2} \ln\frac{2\pi m kT}{h^2} - \ln a +$ $+ \ln\left(1 - \exp\left[-\frac{h\nu_2}{kT}\right]\right)$	-5.7	-5.9
difference for mobile vs loca- lized adsorption	$\frac{u_{act} - h\nu_2}{kT} - \ln\frac{2\pi m kT}{h^2} +$	6.2	5.6
ibid, alumina carrier	$-\ln a^2 - 2 \ln\left(1 - \exp\left[-\frac{h\nu_2}{kT}\right]\right)$	2.4	2.3

An estimate for ν_2 can be made by assuming that the entropy contribution to the free energy of nickel atoms, adsorbed on nickel, is comparable to that of nickel atoms in the surface layer. The latter entropy contribution can be found by adding the entropy contribution to the surface free energy, tabulated as $-1.75 kT$ in table 4.3, to the entropy contribution in the chemical potential of solid nickel, tabulated here as $-4.0 kT$. The result is $-5.75 kT$ at 873 K. Taking into account the contribution due to ν_1 as derived above, this leaves for the contribution of ν_2 of μ/kT :

$$2 \ln (1 - \exp [-\frac{h\nu_2}{kT}]) = -4.69 \text{ at } 873 \text{ K}$$

and accordingly: $\frac{h\nu_2}{k} = 87.5 \text{ K}$

To estimate the margin available, it should be considered, that the maximum contribution of the term involving ν_2 is obtained, when there is complete two dimensional mobility of the adatoms. The corresponding entropy contribution to the chemical potential then is seen from table A.5 to amount to -6.7 kT . The corresponding value of ν_2 follows from:

$$\ln (1 - \exp [-\frac{h\nu_2}{kT}]) = -3.35$$

and is given by: $\frac{h\nu_2}{k} = 31 \text{ K}$

In order to come to the quantitative data in table A.5 we have made the rather arbitrary choices, given in table A.6.

Table A.6. Estimates for vibration frequencies

	Ni		Al ₂ O ₃	
	ν_1	ν_2	ν_1	ν_2
$\frac{h\nu}{k} \text{ (K)}$	370 K	87.5 K	370 K	50 K
$h\nu(10^{-19}\text{J})$	0.051	0.0121	0.051	0.007

As the solid state has to be considered as a given reference in all cases and concentrations and rates are effected by $\exp [\Delta\mu/kT]$, the following conclusions may be drawn in comparing the more accurate predictions with those derived earlier and assembled in table 4.5.

- The equilibrium vapour pressure at 873 K is a factor $\exp [4.0] = 55$ and at 973 K a factor 74 smaller than before; the same factor applies to the rates of diffusion through the gas phase.
- The concentration of adsorbed nickel atoms at 873 K has increased with a factor $\exp [1.8] = 6$ for the particle surface and with a factor $\exp [2.8] = 16$ for the alumina surface. At 973 K the same factors apply. The rates of transport by diffusion over these surfaces have increased accordingly.
- The rates of desorption of nickel atoms from (and adsorption on) nickel and alumina have increased with a factor of $\exp [2.7] = 15$ at 873 K and of 12 at 973 K.
- The rate of the transfer of adsorbed nickel atoms from the nickel to the alumina surface (and vice versa) has increased by a factor of $\exp [1.7] = 5.5$ at 873 K and of 5.0 at 973 K.
- A possible preference of mobile vs localized adsorption is governed by the quantities in the last two lines of table A.5. At 873K the exponentials of $\frac{\Delta U}{kT}$ amount to 490 for nickel and 11 for alumina in favour of localized adsorption. At 973K the corresponding factors in favour of localized adsorption are 270 and 10.

It is seen, that many of the entropy effects of vibration and two-dimensional mobility of transition states compensate. The most significant result is the marked decrease in diffusion transport through the gas phase. The effect of the mobility of adatoms on alumina appears to be very much reduced now as compared with the predictions of section A.1. Yet the high transport efficiency of such mobile adatoms might influence growth rates by step 2 considerably.

In order to see to what extent the relative rates of the various growth processes are influenced, the data for the relevant processes, as tabulated in table 4.5, are corrected and presented again in table A.7.

It is seen, that the rates of nucleation inhibited growth are only slightly influenced by the better approximations. Conclusions as to the rate determining step of the particle growth as derived from table A.7 are nearly the same as those derived from table 4.5, viz:

Table A.7. Linear particle growth rates (to be multiplied by r^n) for the various reaction steps; growth rates in nm h^{-1} , r in nm.

	Reaction step	873 K	973 K	exp. of r
1	$\text{Ni}_{\text{ads}}(\text{Ni}_{\text{edge}}) \leftrightarrow \text{Ni}_{\text{ads}}(\text{Al}_2\text{O}_3)$	0.13	7.4	-1
3	$\text{Ni}_{\text{ads}}(\text{Al}_2\text{O}_3) \leftrightarrow \text{Ni}_{\text{vapour}}$	$2.5 \cdot 10^{-3}$	0.39	0
6	$\text{Ni}_{\text{ads}}(\text{Ni}) \leftrightarrow \text{Ni}_{\text{vapour}}$	$5.1 \cdot 10^{-5}$	$7.8 \cdot 10^{-3}$	0
2	Diffusion over Al_2O_3	$3.0 \cdot 10^{-4}$	$2.7 \cdot 10^{-2}$	-2
	corrected for effect of 3	$4.7 \cdot 10^{-4}$	$4.8 \cdot 10^{-2}$	
	corrected for mobility	$1.9 \cdot 10^{-3}$	$1.3 \cdot 10^{-1}$	-1
4	Diffusion through vapour from one particle to another	0.16	28	-1
5	Diffusion through vapour away from the sample	$1.8 \cdot 10^{-6}$	$3.3 \cdot 10^{-4}$	-1

Analogously, the rate constants for nucleation inhibited growth, as given in eq. (20) and (21) of chapter 4, now should be read as:

$2.8 \cdot 10^4$ instead of $4.7 \cdot 10^3$

$9.7 \cdot 10^5$ instead of $1.6 \cdot 10^5$

- Step 1 and 4 are so fast, that they do not interfere with other slower steps.
- Step 2 has a fast partially parallel, partially serial step in the combination of 3 and 4. As a consequence the concentration gradient, operating 2, is compressed to a distance $\ell'r < \ell r$. Calculating ℓ' such that the two processes match, leads to $\ell' = 4.3$ at 873 K and $\ell' = 3.5$ at 973K. The adapted rates of 2 turn out as $4.7 \cdot 10^{-4} \text{nm h}^{-1}$ at 873K and $4.8 \cdot 10^{-2} \text{nm h}^{-1}$ at 973K.

- There is a certain competition between the parallel steps 2 and 6, where 2 is the faster route. The ratio between 2 and 6, however, depends on the particle size. At a particle radius $r > 3.0$ nm at 873K and of $r > 2.5$ nm at 973K step 6 takes over from 2.
- Mobile adatoms on alumina would lead to a moderate increase of the rate of step 2. The conclusions as to the competition with the other reaction steps remain essentially unmodified.
- Step 5, the diffusion through the vapour phase away from the sample, is much slower than in earlier calculations. This is a fortunate difference as otherwise the sintering experiment would have been accompanied by a gradual depletion of nickel from the sample.

A.3. Derivation of h_{bulk} from equilibrium data about nickel vapour pressures

Theoretically, the equilibrium vapour pressure of solid nickel at temperature T is given by:

$$p(T) = \exp \frac{\Delta S(T)}{k} \cdot \exp - \frac{\Delta h(T)}{kT}$$

where $-\Delta h(T)/kT$ is the slope at T of the Arrhenius plot of $\ln p$ vs T^{-1} , while $\exp \Delta S(T)/k$ is the corresponding pre-exponential factor.

According to Clapeyron, $\Delta h = h_{\text{gas}} - h_{\text{bulk}}$, taken at the temperature where the slope is determined. Accordingly $\Delta S = S_{\text{gas}}^{\circ} - S_{\text{bulk}}^{\circ}$, taken at the same temperature and at unit pressure.

Using the approximations, outlined earlier in this appendix, it is found that:

$$h_{\text{gas}}(T) - h_{\text{bulk}}(T) = -h_0 + 5/2 kT - 3 kT \phi(\theta_D/T) \quad (9)$$

$$\text{and } S_{\text{gas}}^{\circ}(T) - S_{\text{bulk}}^{\circ}(T) = k \left(5/2 + 3/2 \ln \frac{2\pi m kT}{h^2} + \ln kT + \right.$$

$$\left. - 4\phi(\theta_D/T) + 3 \ln (1 - \exp [-\theta_D/T]) \right)$$

Table A.8 presents values of these quantities for several temperatures.

Table A.8. Numerical data for the energy and entropy of evaporation.

T(K)	$h_{\text{gas}} - h_{\text{bulk}}$ (10^{-19}J)	$1/k (S_{\text{gas}}^{\circ} - S_{\text{bulk}}^{\circ})$ ($p_0 = 1\text{Nm}^{-2}$)
873	$- h_{\text{bulk}}(0) - 0.006$	26.8
973	$- h_{\text{bulk}}(0) - 0.013$	26.7
1200	$- h_{\text{bulk}}(0) - 0.028$	26.6
1500	$- h_{\text{bulk}}(0) - 0.048$	26.6
1726 *)	$- h_{\text{bulk}}(0) - 0.063$	26.5

*) melting point of nickel

Experimental data gathered by A.N. Nesmeyanov [4] consist of two strongly different groups of results, see table A.9. From these data we select as characteristic quantities:

- the vapour pressure at 1400 K (being the mean temperature of many series of experiments). The vapour pressure is the directly measured quantity!
- the entropy $\Delta S/k$, as deduced from the temperature dependency of the vapour pressure. This entropy can directly be compared with the thermodynamical predictions of table A.8.

Table A.9. Characteristic data for the evaporation of Ni, taken from Nesmeyanov [4]

	$p(\text{Nm}^{-2})$	$\Delta S/k$	$\theta_D(\text{K})$	$\Delta h(1400\text{K})$ (10^{-19}J)
Group 1	$1.33 \cdot 10^{-3}$	28.0	588	6.60
Group 2	0.84	31.1	1750	5.44

The predicted value of $\Delta S/k$ on basis of the Debye temperature for nickel, $\theta_D = 370$ K, is 26.6. The Debye temperatures corresponding with the experimental data of $\Delta S/k$ have been listed in the third column of the table. As the value of $\theta_D = 370$ K is determined by measuring the specific heat of nickel at relatively low temperatures, while here we are dealing with measurements of the vapour pressure at high temperatures, a difference in the Debye temperature is possible.

The results of group 2 cannot be totally correct because extrapolation of the data to 973 K and 873 K would result in such high vapour pressures and accordingly such high diffusion rates of nickel away from the sample, that the experiments described in this thesis would have been impossible to do.

The values of Δh at 1400 K, corresponding to the theoretical entropy value and the observed vapour pressure at 1400 K, have been calculated and are given in the last column of the table. The argument concerning the maximum value of the vapour pressure, which is reasonably acceptable at 873K, leads to the conclusion that Δh can hardly be lower than $6.0 \cdot 10^{-19}$ J. Therefore we shall adopt this value for calculations, but take into account that values up to $6.7 \cdot 10^{-19}$ J may be possible. In order to come from $\Delta h(1400)$ to h_{bulk} , as defined in eq (8), according to eq (9) the following correction has to be made:

$$h_{\text{bulk}} = -\Delta h(1400) + 5/2 k * 1400 - 3k * 1400 \phi(\theta_D/1400) + 9/8k\theta_D.$$

It is seen that the correction is of minor importance compared with the other uncertainties. Therefore the value to be used will be:

$$h_{\text{bulk}} = - 6.0 \cdot 10^{-19} \text{ J}$$

An independent check on the feasibility of this value can be obtained through the surface free energy. According to table 4.3 the values derived for $\sigma \cdot a^2$ from the present value of h_{bulk} would be $1.5 \cdot 10^{-19}$ J for the (111)-face and $2.0 \cdot 10^{-19}$ J for the (100)-face. Experimental values are available for temperatures close to the melting point: 1726K. Making the corrections for the temperature dependance of $\sigma \cdot a^2$ indicated

in table 4.3 and using the values for a^2 of $5.37 \cdot 10^{-20} \text{ m}^2$ for the (111)-face and of $6.20 \cdot 10^{-20} \text{ m}^2$ for the (100)-face, the following values are predicted for the surface free energies:

$$(111)\text{-face: } \sigma = 2.02 \text{ J m}^{-2}$$

$$(100)\text{-face: } \sigma = 2.55 \text{ J m}^{-2}$$

A representative experimental value is 1.81 J m^{-2} [5, 6]. Also here we find a justification of the adopted value for h_{bulk} , while there is an indication that we may have overestimated our values of σ and of the quantity $2\sigma a^3/kT$.

A.4. Geometric factors

The factor a , occurring in the various geometric factors of section 4.3, has different origins. It may arise from the volume per atom added to the growing crystal, but also from the surface per adsorption site either for nickel or for alumina. Finally, in one case it applies to the linear distance separating adsorption sites along the edge between nickel particle and the alumina support.

Obviously it is an approximation to define these quantities as a^3 , a^2 and a , respectively, and to use the same numerical value of a in the three cases. In view of the other approximations made, however, this modest approximation is easily justified. The numerical value taken in order to calculate tables 4.4 and 4.5 is $2.22 \cdot 10^{-10} \text{ m}$, which is $v_m^{1/3}$, where v_m is the volume per atom of bulk nickel. The corresponding distance between nearest neighbour atoms in the nickel crystal is:

$$a' = a \cdot 2^{1/6} = 2.49 \cdot 10^{-10} \text{ m}$$

There is one instance, where more care is required in defining a , namely equation (4.19) for the growth rate as limited by two dimensional nucleation on particle facets, as is seen in section 4.6. Here the growth rate is strongly influenced by the exponential

$$\exp \left[- \frac{\pi \epsilon}{2kT} \left(\frac{\epsilon}{\sigma a} + \frac{3}{4} \right) r^* \right]$$

In this formula, a represents the thickness of an extra adsorbed layer, while ϵ and σ must be derived from the estimated values for the atomic quantities $\epsilon a = \epsilon'$ and $\sigma a^2 = \sigma'$ of table 4.3. In the latter two equations, a represents the distance between nickel atoms along the edge of the two dimensional nucleus and a^2 the surface per nickel atom at the lattice plane considered. Different results are obtained for the (111) and (100) faces of the fcc nickel crystal, as can be seen in table A.10.

Table A.10. Characteristic parameters for different crystal planes

	Thickness of the ads. layer	Distance along edge	Surface per atom	$\frac{\epsilon}{a\sigma}$
(111)	$1/3 a' \sqrt{6}$	a'	$1/2 (a')^2 \sqrt{3}$	$\epsilon' / \sigma' \cdot 3 \sqrt{2} / 4$
(100)	$1/2 a' \sqrt{2}$	a'	$(a')^2$	$\epsilon' / \sigma' \cdot \sqrt{2}$

Similarly, in the factor $\pi\epsilon/2kT$, ϵ should be taken as:

$$\frac{\epsilon'}{a'} = \frac{\epsilon'}{a'^2}^{1/6}$$

In connection with this point it should be stressed that all through chapter 4 essential formulas about surface free energies of curved surfaces of small particles and curved edges of two-dimensional nuclei have been used as derived for continuous media and perfect spherical or circular shapes. The particles studied in the present research, however, have radii of the order of nm, while the two dimensional nuclei are even smaller. The number of atoms in such particles might deviate considerably from the idealized shapes. This problem has been studied extensively by J.C. Anderson [5]. Fortunately his conclusions are, that although some quantitative differences may occur, the qualitative description taking into account the correct structures on an atomic scale, does not deviate essentially from the description based on continuous models.

A.5. Zeldovich factor

The Zeldovich factor in the equation for the rate of formation (I_N) of two-dimensional nuclei on a flat surface, see section 4.6, expresses the consequences of deviations from equilibrium in the concentrations of nuclei of sizes close to the critical size. It is a dimensionless factor and provisionally it has been taken as equal to 1. In fact the correct value is:

$$Z = \left(\frac{2\sigma^3 a^7}{\pi^2 \epsilon^2 kT} \right)^{1/2} \left(\frac{1}{r^*} - \frac{1}{r} \right)^{3/2}$$

With the values of the various parameters, used earlier, and with r and r^* expressed in nm:

$$Z = 0.25 \left(\frac{1}{r^*} - \frac{1}{r} \right)^{3/2} = 0.25 \left(\frac{1}{r^*} \right)^{3/2} \left(\frac{\rho - 1}{\rho} \right)^{3/2} \quad \text{for the (111)-face}$$

and:

$$Z = 1.12 \left(\frac{1}{r^*} \right)^{3/2} \left(\frac{\rho - 1}{\rho} \right)^{3/2} \quad \text{for the (100)-face}$$

where ρ is a dimensionless radius defined as $\rho = r/r^*$.

It is seen, that Z depends on r^* and ρ . In view of the dominating effect of the second exponential factor in eq. (4.19) and the limited ranges of r^* and ρ , where two-dimensional nucleation operates, it is quite reasonable to take Z as a constant. It is also seen, however, that the value of this constant is better approximated by for instance 0.05 than by 1.

A.6. References

- [1] K.J. Laidler; J.H. Meiser: Physical Chemistry, Benjamin/Cummings 1982, Ch. 9.
- [2] J.H. Knox: Molecular Thermodynamics, John Wiley & Sons, 1978.
- [3] E. Hala; T. Boublik: Einführung in die Statistische Thermodynamik, Vieweg, 1970.

- [4] A.N. Nesmeyanov: Vapor pressure of the chemical elements, Elseviers Publ. Comp., 1963.
- [5] B. Lewis and J.C. Anderson: Nucleation and growth of thin films, Academic Press, 1978.
- [6] E.A. Clark: R. Yeske: H.B. Birnbaum; Metall. Trans. 11A (1980) 1903.

SUMMARY

The physical principle by which the catalytic activity of a metal/oxide catalyst decreases is coarsening of the metal dispersion. This process may be caused by sintering of the support, Ostwald ripening of the metal particles, or by particle growth through collisions of migrating metal particles along the support. Because of the intense contact between metal and carrier, mutual interaction may change the sinter behaviour of the individual compounds. Much work is devoted in literature to the influence of dopes on the thermostability of highly porous alumina supports, while less is known about the influence of the support and dopes on the sintering of the supported metal particles.

The study described in this thesis, is performed in order to give more insight into the sinter mechanism of supported metal dispersions and the influence of additives on this part of the process.

In **chapter 1** this study is placed within the framework of the research in our laboratory. A short summary is given of literature concerning the following subjects: sintering of $\text{Ni}/\text{Al}_2\text{O}_3$ catalysts, the behaviour of Pt and Pd supported model catalysts and fundamental studies emphasizing the theoretical aspects of sintering.

The study in question follows two main lines, viz: sinter kinetic measurements of a model $\text{Ni}/\text{Al}_2\text{O}_3$ catalyst with or without additives and chemical analysis of the metal support interface on the one hand, and development of a theoretical sinter kinetic model suitable for analysis of the experimental data, on the other hand.

In **chapter 2** preparation and sinter experiments of four different model systems, viz. $\text{Ni}/\text{Al}_2\text{O}_3$, $\text{Ni}/\text{Cr}/\text{Al}_2\text{O}_3$, $\text{Ni}/\text{Mn}/\text{Al}_2\text{O}_3$ and $\text{Ni}/\text{Mn}/\text{Cr}/\text{Al}_2\text{O}_3$, have been described. Sintering at 873 and 973 K is followed ex-situ in the Transmission Electron Microscope and samples, after sintering for about 300 hours, have been analyzed by Transmission Electron Diffraction.

Independent of the sinter temperature or composition, all model catalysts show a fast initial stage of sintering of 10 hours, followed by stabilization of the mean particle size. Dispersions with a mean particle radius of 11 nm are thermostable even at 973 K.

During ageing of the $\text{Ni}/\text{Al}_2\text{O}_3$ model catalyst at 973 K nickel aluminate

is formed. Addition of manganese leads to enhanced sintering rates, while again nickel aluminate is formed. Addition of chromium delays sintering and apparently prevents formation of nickel aluminate. Addition of chromium and manganese together, only slightly influences the stabilization level. In this catalyst nickel and manganese aluminate is detected. The results of the chemical analysis of the Ni/Al₂O₃ interface are presented in **chapter 3**. Analysis is carried out with X-ray Photoelectron Spectroscopy, combined with ion etching, in order to obtain depth profiles, using thin layer composites aged for 100 hours in hydrogen at 973 K.

The interfacial layer in the Ni/Al₂O₃ system consists of a solid solution of nickel oxide in alumina. In the Ni/Cr/Al₂O₃ composite nickel chromate is supposed to form the interfacial layer, while no diffusion layer could be detected in the Ni/Mn/Al₂O₃ composite.

In **chapter 4** a theoretical analysis of the kinetics of the growth of individual particles is given and by means of a thermodynamic and kinetic model an estimate is made of the rate determining process steps.

Using Eyring's theory of reaction rates for all elementary steps occurring, the rate is found to be proportional to the concentration of atomic species in the transition state and hence dependent on the chemical potentials of the reaction partners. By neglecting the vibrational and rotational entropy contributions in the chemical potentials, relatively simple equations are obtained for the reaction rates. From the equilibrium calculations calculations result in the concentrations of the migrating atoms in the gas phase and adsorbed states. Diffusion from and towards a particle is subsequently defined and by means of a geometric factor converted into a growth rate.

Using a broken bond model, all important, but unknown, energy parameters are related to the experimentally known value of the heat of evaporation of nickel. So the rates of individual growth steps can be estimated and rate determining steps established.

For nickel particles on an alumina support, the growth appears to be determined either by diffusion of atomic species to the vapour phase or by diffusion along the alumina support. However, as soon as growth is determined by nucleation -in the case of faceted crystallites- effectively growth is terminated.

A critical analysis, in the appendix, of the approximations used in the kinetic and thermodynamic model shows, that, taking into account the mobility of the transition states for adsorption and desorption our calculations lead to substantially increased growth rates. However, this effect is partially compensated by considering the contribution of the vibrational entropy in the chemical potential of bulk nickel as well. Moreover, by this effect the vapour pressure of nickel and the equilibrium amounts of adsorbed nickel are reduced significantly. In this way it also becomes clear, why there is no more depletion of nickel from the sample by diffusion away into the reactor.

In **chapter 5**, the kinetics of the sintering of a supported particle dispersion, Ostwald ripening, by atomic emission and capture is discussed, using the model of eg. T.M. Ahn, based on the L.S.W. theory with some modifications. An essential improvement is obtained by using a better series expansion for the factor representing the supersaturation. Now the kinetics is no longer of the power law type predicted in previous theories, but an additional exponential dependency on the particle radius appears.

Numerical calculations predict a maximum particle radius of 3 nm for sintering at 873 K during 1000 hours, while the process is determined by diffusion of mobile adatoms along the support. Sintering at 973 K during 1000 hours, with the same mechanism determining sintering, leads to a maximum particle radius of 8 nm. For particles with a radius larger than 0.5 nm (at 873 K) and 2 nm (at 973 K) growth stops as soon as faceting of the nickel particles occurs and nucleation inhibition becomes rate determining.

In **chapter 6** the results of the experimental studies are compared with the theoretical predictions.

At 973 K, sintering of all model catalysts, independent of the chemical composition, appears to be governed by diffusion of the mobile adatoms along the alumina support as rate determining step. The rate of this diffusion appears to be sensitively influenced by the type of additive used. Probably, this is so, because there is a rather delicate balance between localized and mobile adsorbed species, the latter contributing much more to mass transport than the former. Additives apparently will influence this delicate balance. Further in some cases the development of a diffusion boundary layer, as shown by the XPS analyses, appears to be accompanied by improvement of the nickel crystallite habits,

resulting in stabilization of the mean particle size of the nickel dispersion. Overall, the reaction rate and hence the degree of stabilization decreases in the order $\text{NiCr}_2\text{O}_4 > \text{NiAl}_2\text{O}_4 > \text{MnAl}_2\text{O}_4$. At 873 K, very low rates of sintering are predicted by the theoretical treatment for particles with radii larger than 3 nm. Experimentally substantial sintering is observed for such particles. Indications have been obtained, however, that, contrary to the original intent of this investigation, the alumina carrier films were not sufficiently thermostable and did show a certain amount of recrystallization during the sinter experiments.

SAMENVATTING

Het fysisch proces, verantwoordelijk voor de afname van de katalytische activiteit van metaal-op-drager katalysatoren, is het grover worden van de metaaldeeltjes. Dit proces wordt veroorzaakt door zowel het sinteren van de drager, vergezeld van migratie van metaaldeeltjes over de drager, als door groei van de metaaldeeltjes. Vanwege het intensief contact tussen beide componenten kan onderlinge beïnvloeding leiden tot een specifiek sintergedrag van elk van beide componenten. Uitgebreid onderzoek is en wordt verricht naar de invloed van dotering op het sintergedrag van hoog poreuze alumina dragers, terwijl weinig bekend is over de invloed van alumina dragers en doteringen op het sintergedrag van de metaaldispersie. Het onderzoek, zoals beschreven in dit proefschrift, is uitgevoerd om meer inzicht te verkrijgen in het sintermechanisme van nikkel metaaldispersies en de invloed van alumina dragers en doteringen op het sintergedrag van de metaaldispersie.

Het onderzoek, zoals beschreven in dit proefschrift, is uitgevoerd om meer inzicht te verkrijgen in het sintermechanisme van nikkel metaal dispersies en de invloed van een aluminadrager met en zonder toevoegingen.

In **hoofdstuk 1** is dit werk geplaatst in het kader van het onderzoek binnen onze groep. Met een korte samenvatting wordt een literatuuroverzicht gegeven van achtereenvolgens het sinteronderzoek aan $\text{Ni/Al}_2\text{O}_3$ katalysatoren, het onderzoek naar het gedrag van Pt en Pd dispersies op een stabiele aluminadrager en fundamenteel theoretisch onderzoek van de sinterkinetiek van kleine metaaldeeltjes op een drager.

Het onderhavige onderzoek verloopt langs twee lijnen, namelijk het experimenteel bestuderen van het sintergedrag van een $\text{Ni/Al}_2\text{O}_3$ modelkatalysator met en zonder toevoegingen en chemische analyse van het nikkel-drager grensvlak enerzijds, en het ontwikkelen van een theoretisch sintermodel voor de analyse van de experimentele resultaten anderzijds.

In **hoofdstuk 2** wordt de bereiding en het sinteren van vier verschillende modelsystemen, te weten $\text{Ni/Al}_2\text{O}_3$, $\text{Ni/Cr/Al}_2\text{O}_3$, $\text{Ni/Mn/Al}_2\text{O}_3$ en $\text{Ni/Mn/Cr/Al}_2\text{O}_3$ beschreven. Sinteren is ex-situ gevolgd in de Transmissie Electronen Microscoop bij 873 K en 973 K en na 300 uur sinteren geanalyseerd met Transmissie Electronen Diffractie.

Ongeacht de sintertemperatuur vertonen alle modelkatalysatoren een snelle stijging van de gemiddelde deeltjesgrootte gedurende de eerste 10 uur, waarna sinteren afneemt en de deeltjesgrootte een stabilisatieniveau bereikt na ca 50 uur. Dispersies met een gemiddelde deeltjesstraal van 11 nm zijn zelfs bij 973 K thermostabiel.

Tijdens het sinteren van de $\text{Ni}/\text{Al}_2\text{O}_3$ katalysator bij 973 K ontstaat nikkeraluminaat. Toevoeging van chroom vertraagt sinteren en gaat de vorming van aluminaat tegen. Daarentegen versnelt mangaan het sinteren van de nikkeldispersie terwijl ook in deze katalysator nikkeraluminaat ontstaat naast mangaanaluminaat. Bij het gebruik van een gecombineerde tussenlaag wordt slechts een lichte verhoging van het stabilisatieniveau verkregen. In deze modelkatalysator wordt eveneens nikkel- en mangaanaluminaat aangetoond.

De resultaten van de chemische analyse van het $\text{Ni}/\text{Al}_2\text{O}_3$ grensvlak zijn weergegeven in **hoofdstuk 3**. Analyse is uitgevoerd met Röntgen Foto *electronen Spectroscopie (XPS)*, waarbij door combinatie met ionen etsen diepteprofielen gemeten konden worden rondom de grensvlakken van dunne-laagcomposieten. Na de reactie in waterstof bij 973 K gedurende 100 uur ontstaat in het $\text{Ni}/\text{Al}_2\text{O}_3$ composiet een grenslaag, bestaande uit een vaste oplossing van nikkeloxide in alumina. In het $\text{Ni}/\text{Cr}/\text{Al}_2\text{O}_3$ composiet ontstaat nikkelchromaat aan het grensvlak, terwijl geen reactieproducten worden gevonden in het $\text{Ni}/\text{Mn}/\text{Al}_2\text{O}_3$ systeem.

In **hoofdstuk 4** wordt de kinetiek van de groei van individuele deeltjes op een drager geanalyseerd en met een thermodynamisch en kinetisch model wordt een afschatting gemaakt van de snelheidsbepalende processtappen. Dit geschiedt door de snelheden van de verscheidene processtappen te beschrijven met de meest eenvoudige versie van Eyring's theorie voor reactiesnelheden. Hierbij wordt aangenomen dat de overgangstoestand in evenwicht is met de reactanten en aldus de concentratie daarvan bepaald wordt door de chemische potentiaal van de desbetreffende reactanten. Door alle vibratie- en rotatiebijdragen in de chemische potentiaal te verwaarlozen worden relatief eenvoudige relaties verkregen voor de reactiesnelheden. Uit het evenwichtskriterium wordt de concentratie van de migrerende metaalatomen op diverse plekken in het systeem verkregen, waarmee de massastromen van en naar een deeltje kunnen worden gedefinieerd. Met een geometrische factor worden deze massastromen omgezet in groeisnelheden bestaande uit een nagenoeg temperatuurafhankelijke pre-exponentiële factor en een activeringsenergie.

Gebruikmakend van een "broken bond model" worden alle essentiële en onbekende energieparameters gerelateerd aan de verdampingswarmte van kristallijn nikkel.

Uit een afschatting van alle groeisnelheden blijkt dat de groeisnelheid hoofdzakelijk wordt bepaald door verdamping naar de gasfase of door diffusie over de drager, en nagenoeg direkt stopt zodra het groeiproces bepaald wordt door nucleatie.

Een kritische analyse, in de **appendix**, van de benaderingen gemaakt in de kinetische en thermodynamische beschouwing, laat zien dat verwaarlozing van de mobiliteit van de overgangstoestand voor adsorptie en desorptie leidt tot een onderschatting van de groeisnelheid. Daarentegen leidt de correctie van de thermodynamische potentiaal van "hulk"-nikkel met de vibratie-entropie tot een sterke vermindering van dampspanning en de verdampingssnelheden, hetgeen niet alleen het voorgaande effect voor een deel compenseert, maar bovendien duidelijk maakt waarom er geen nikkelverlies optreedt door diffusie van het preparaat af.

In **hoofdstuk 5** wordt de kinetiek van het sinteren van een deeltjesverzameling op een drager -het "Ostwald ripening" proces- beschreven aan de hand van het model van o.a. T.M. Ahn, gebaseerd op de L.S.W. theorie, en hier en daar aangepast. Een essentiële verbetering wordt verkregen door het toepassen van een betere reeksontwikkeling voor de factor, die de oververzadiging weergeeft. De groeisnelheden voor het geval van massatransport door diffusie via de gasfase en over het drageroppervlak zijn dan niet meer alleen evenredig met r^n , maar eveneens exponentieel afhankelijk van r . Numerieke berekeningen voorspellen voor het sinteren bij 873 K gedurende 1000 uur een maximale gemiddelde deeltjesstraal van 3 nm met diffusie van mobiele adatomen over het drageroppervlak als snelheidsbepalende stap. Sinteren bij 973 K verloopt via hetzelfde sintermechanisme, waarbij na 1000 uur een maximale gemiddelde deeltjesstraal van 8 nm mogelijk is. Zodra nucleatie tijdens groei de snelheidsbepalende stap wordt, treedt een aanzienlijke vertraging in groei op van deeltjes groter dan 0,5 nm bij 873 K en 2 nm bij 973 K.

Uit de analyse van de experimentele resultaten van het kinetisch en chemisch onderzoek bij 973 K, zoals weergegeven in **hoofdstuk 6**, blijkt dat sinteren, ongeacht de chemische samenstelling van de modelkatalysator, beschreven kan worden door atomaire emissie en invangst met diffusie van mobiele adatomen over de alumina drager als snelheidsbepalende stap.

Het blijkt, dat de diffusiesnelheid sterk beïnvloed wordt door de toevoeging van Cr en/of Mn. Dit lijkt vooral een gevolg te zijn van de delicate balans tussen gelocaliseerde en mobiele adsorptie, waarbij mobiele adatomen belangrijk meer bijdragen tot het massatransport, dan hun gelocaliseerde partners. Verder kan het ontstaan van een diffusiegrenslaag tussen metaaldeeltjes en drager gepaard gaan met het ontstaan van laag energetische kristalvlakken aan het nikkeloppervlak en stabilisatie van de gemiddelde deeltjesgrootte. Samenvattend blijkt dat de mate van stabilisatie afneemt in de volgorde $\text{NiCr}_2\text{O}_4 > \text{NiAl}_2\text{O}_4 > \text{MnAl}_2\text{O}_4$. De theorie voorspelt zeer lage sintersnelheden bij 873 K voor deeltjes met een straal groter dan 3 nm. Dat experimenteel toch ook voor grotere deeltjes substantiële sintering is waargenomen, moet dan ook toegeschreven worden aan de omstandigheid dat, tegen de bedoeling in, de alumina vliesjes toch niet voldoende thermostabiel waren en zelf rekristalliseerden.

LIST OF SYMBOLS

a	lattice parameter; adatom jump distance
D	diffusion coefficient
E_b	binding energy per atom/ion
E_k	kinetic energy per atom/ion
G	Gibbs free energy
ΔG_{cr}	free energy of formation of a critical nucleus
h	enthalpy content per atom
I	peak intensity
I_N	rate of formation of two-dimensional nuclei
J	mass flux
l	ratio of average distance between particles and particle diameter
L	ratio of sample diameter and particle diameter
m	atomic mass
ρ	number of atoms/ions per unit volume
n_0	number of adsorption sites per unit area
n_e	number of adsorption sites along the edge of a particle per unit length
n^+	number of species in the transition state per unit area
n_{ads}	number of adsorbed species per unit area
n_{eq}	equilibrium concentration of adsorbed species
n^*	number of critical nuclei per unit area
p	vapour pressure
p_0	normal atmospheric pressure; $1 \cdot 10^5 \text{ Nm}^{-2}$
p_∞	vapour pressure over a flat surface
p_r	vapour pressure over a particle with radius r
p.e.	photoelectron
r	radius of a particle
r^*	radius of a particle in equilibrium with the environment
S	entropy; sensitivity factor
TFC	thin film composite
u_{act}	activation energy for jumps along the surface
v	reaction rate
v_a	adsorption rate
v_c	condensation rate

v_d	rate of desorption
v_e	evaporation rate
w	energy content of a single bond
X_c	intensity ratio of the most prominent XPS peak and the total photoelectron peak
Z	Zeldovich non-equilibrium correction factor
θ_D	Debye temperature
ε	edge energy
γ	Young's contact angle
λ	adjustable parameter in ensemble growth rate
μ	chemical potential
ν	vibrational frequency of adsorbed atoms
ω	average jump frequency
ρ	dimensionless radius: $r(t)/r^*(t)$
ρ_{cr}	radius of a critical nucleus
σ	surface free energy
τ	time constant for diffusion
τ	dimensionless time: $\ln [r^*(t)/r^*(o)]$
h	constant of Planck; $6.63 * 10^{-34}$ J s
k	constant of Boltzmann; $1.38 * 10^{-23}$ JK ⁻¹
N_{av}	Avogadro number; $6.02 * 10^{23}$ mol ⁻¹
$m(Ni)$	$9.75 * 10^{-26}$ kg
$a(Ni)$	$2.22 * 10^{-10}$ m
$a(Pt)$	$2.47 * 10^{-10}$ m

CURRICULUM VITAE

De schrijfster van dit proefschrift werd geboren op 29 september 1949 te Paramaribo in Suriname.

Na in 1965 vanuit Paramaribo te zijn geëmigreerd naar Hoensbroek (Nederland, Limburg) behaalde zij in 1969 haar H.B.S.-B diploma aan het St. Claracollege in Heerlen.

In hetzelfde jaar begon zij met de Scheikunde studie aan de Technische Universiteit te Delft. In maart 1980 legde zij met goed gevolg het doctoraal examen af, met als afstudeeronderzoek het bestuderen van de heterogene uitwisseling van ionen tussen kristallen en hun verzadigde oplossing, onder leiding van Prof.Ir. J.P.W. Houtman van het IRI. Hierbij verwierf zij de eerstegraads onderwijsbevoegdheid in de scheikunde, natuurkunde en mechanica.

Van augustus 1980 tot augustus 1984 was zij in dienst van het SON/ZWO bij de vakgroep anorganische- en fysische chemie van de afdeling Scheikundige Technologie in Delft. Gedurende deze periode is het onderzoek dat beschreven is in dit proefschrift uitgevoerd onder leiding van Prof.Dr.Ir. L.L. van Reijen.

Sinds 1 juni 1985 is zij werkzaam bij het Energieonderzoek Centrum Nederland, afdeling Chemie en Materiaalkunde.

STELLINGEN

1. De benadering van de Kelvin-Thomson vergelijking met een beperkte reeksontwikkeling is onjuist in het geval van deeltjes ter grootte van enkele nanometers.

Dit proefschrift, hoofdstuk 5.

2. Het door Suwa voorgestelde verdichtingsmechanisme van met $\alpha\text{-Al}_2\text{O}_3$ gezaaid boehmiet is in tegenspraak met de gepresenteerde röntgendiffractie gegevens.

Y. Suwa, R. Roy, S. Komarneni; Mat.Sci. & Eng. 83 (1986) 151.

3. De door Bettinelli voorgestelde procedure om zeer zuivere alumina poeders versneld te verdichten met sinterhulpmiddelen die in minder zuivere alumina poeders reeds als verontreinigingen aanwezig zijn, getuigt niet van kostenbewustzijn.

A. Bettinelli, J. Guille, J.C. Bernier; Cer.Int. 14 (1988) 31.

4. In de door Aksay gegeven modelbeschrijving van het slibgietsproces is het verloop van de drukgradiënt in de mal en de koek niet correct afgeleid.

I.A. Aksay, C.H. Schilling, in Advances in Ceramics, J.A. Mangels en G.L. Messing, Eds., American Ceramic Society, Columbus, OH, 1984, Vol. 9, pg. 85.

5. Voor de weergave van het mechanisch gedrag van polymeercomposieten, is de rek een betere maat dan de spanning.
6. In het extrusieonderzoek van keramische pasta's op basis van thermoplasten zou de huidige kennis op het gebied van vormgeving van gevulde polymeren vruchtbaar gebruikt kunnen worden.

7. Aangezien het Trommsdorff-effect en het gel-effect gelijktijdig optreden bij radicaal polymerisatie, worden zij dikwijls vereenzelvigd. Het ware beter duidelijk onderscheid te maken tussen deze effecten.
8. Spuitgieten van keramische pasta's op waterbasis heeft duidelijk economische voordelen ten opzichte van het gebruik van pasta's op basis van thermoplasten.
9. Hg-porosimetrie, gebaseerd op een cilindrisch poriemodel, geeft geen betrouwbare weergave van de poriestructuur van een willekeurig poreus materiaal.
10. Het nadrukkelijk werven van vrouwen voor beroepen die hun aantrekkingskracht op de arbeidsmarkt hebben verloren, kan worden gezien als een ehec van de emancipatiegedachte.

Luci Correia

Delft, 23 mei 1989